CERN / LHCC 99–5
ALICE TDR 3
5 March 1999

A L I C E

Technical Design Report

of the

Zero Degree Calorimeter (ZDC)

Spokesperson
J. Schukraft

ZDC Project Leader
M. Gallio

Technical Coordinator
W. Klempt

Engineering/Integration Coordinator
L. Leistam

Resources Coordinator
J. de Groot

This edition contains a few minor modifications, essentially corrections of typographical errors, relative to the first, limited, edition.

Cover design by Fabienne Marcastel

Printed at CERN
March 1999

ISBN 92-9083-139-1

ALICE Collaboration

Alessandria, Italy, Facoltà di Scienze dell'Università:
G. Dellacasa, L. Ramello, E. Scalas, M. Sitta and C. Soave.

Aligarh, India, Physics Department, Aligarh Muslim University:
N. Ahmad, S. Ahmad, T. Ahmad, W. Baritak, M. Irfan and M. Zafar.

Athens, Greece, Nuclear and Particle Physics Division, University of Athens:
A.L.S. Angelis, A. Kapogiannis, G. Mavromanolakis and A.D. Panagiotou.

Athens, Greece, Institute of Nuclear Physics, NRC Demokritos:
K. Kalfas.

Bari, Italy, Dipartimento di Fisica dell'Università and Sezione INFN:
N. Colonna, D. Cozza, D. Dell'Olio, D. Di Bari, D. Elia, R.A. Fini, B. Ghidini, V. Lenti, L. Liberti, R. Loconsole, V. Manzari, E. Nappi[1)], F. Navach, F. Posa, S. Stucchi and G. Tomasicchio.

Bari, Italy, Politecnico and Sezione INFN:
F. Corsi, D. De Venuto, M. Di Ciano, R. Dinapoli, G. Gramegna, A. Grimaldi, P. Lamanna, C. Marzocca, G. Matarrese and E. Monno.

Beijing, China, China Institute of Atomic Energy:
Shuhua Zhou.

Bergen, Norway, Department of Physics, University of Bergen:
E. Andersen, K. Fanebust, H. Helstrup, A. Klovning, O.H. Odland, D. Röhrich and T.F. Thorsteinsen.

Bhubaneswar, India, Institute of Physics:
A.K. Dubey, D.P. Mahapatra and S.C. Phatak.

Birmingham, United Kingdom, School of Physics and Space Research, University of Birmingham:
I.J. Bloodworth, D. Evans, G.T. Jones, P. Jovanović, J.B. Kinson, A. Kirk, O. Villalobos Baillie and M.F. Votruba.

Bratislava, Slovakia, Faculty of Mathematics and Physics, Comenius University:
J. Braciník, V. Černý, J. Ftáčnik, V. Hlinka, M. Ivanov, R. Janik, R. Lietava, M. Pikna, J. Pišút, N. Pišútová, B. Sitar, P. Strmeň and I. Szarka.

Budapest, Hungary, KFKI Research Institute for Particle and Nuclear Physics, Hungarian Academy of Sciences:
E. Denes, B. Eged, Z. Fodor, G. Harangozo, T. Kiss, G. Palla, G. Rubin, J. Sulyan, L. Szendrey, J. Sziklai, D.L. Tarjan, Z. Varga, B.N. Vissy and J. Zimanyi.

Cagliari, Italy, Dipartimento di Fisica dell'Università and Sezione INFN:
C. Cicalo, A. De Falco, M.P. Macciotta-Serpi, A. Masoni, S. Mauro, G. Puddu, P. Randaccio, S. Serci, E. Siddi and G. Usai.

Calcutta, India, Saha Institute of Nuclear Physics:
P. Bhattacharya, S. Bose, Sukalyan Chattopadhyay, N. Majumdar, A. Sanyal, S. Sarkar, P. Sen, S.K. Sen and B.C. Sinha.

Calcutta, India, Variable Energy Cyclotron Centre:
Subhasis Chattopadhyay, M.R. Dutta Majumdar, M.S. Ganti, T.K. Nayak, R.N. Singaraju, M.D. Trivedi and Y.P. Viyogi.

Catania, Italy, Dipartimento di Fisica dell'Università and Sezione INFN:
A. Badalà, R. Barbera, U. Becciani, C. Caligiore, M. Gulino, S. Ingrassia, A. Insolia, F. Librizzi, D. Lo Presti, D. Nicotra, A. Palmeri, S. Panebianco, G.S. Pappalardo, L. Pappalardo, C. Petta, N. Randazzo, S. Reito, F. Riggi, A.C. Russo, G.V. Russo, M. Russo, G. Saccà and A. Sciuto.

CERN, Switzerland, European Laboratory for Particle Physics:
J. Bächler, A. Bajeli[2)], J.A. Belikov[3)], V. Berejnoi[4)], J.-C. Berset, R. Brun, M. Burns, J. Buytaert, M. Campbell, E. Cantatore, W. Carena, F. Carminati, J. Christiansen, D. Collados, C. D'Ambrosio, M. Davenport, J. de Groot, A. Di Mauro, R. Divià, C. Eisenberg, C. Engster, J. Espirito Santo, M. Fageda, H.G. Fischer, M. Flammier, F. Formenti, D. Fraissard, E. Futo[5)], E. Gaumann, M. Goossens, B. Goret, T. Grassi, C. Gregory, M. Hoch, P.G. Innocenti, A. Jachołkowski, W. Klempt, A. Kluge, K. Knudson, G. Lecoeur, J.C. Legrand, L. Leistam, P. Lenoir, Y. Lesenechal, C. Lourenço, A. Malinine, P. Martinengo, M. Mast, T. Meyer, H. Milcent, R. Monnin, M. Morel, A. Morsch, M. Mota, L. Musa, B. Perrin, L. Pigni, F. Piuz, E. Quercigh, J. Raynaud, H. Renshall, A. Rivetti, K. Šafařík, J.-C. Santiard, J. Schukraft, E. Schyns, W. Snoeys, P. Sonderegger, M. Spegel, D. Swoboda, P. Szymanski, G. Tabary, J. van Beelen, H. van der Velde, P. Vande Vyvre, A. Vascotto, D. Vranic, S. Wenig, P. Wertelaers, T. Williams and K. Zelazowski.

Chandigarh, India, Physics Department, Panjab University:
M.M. Aggarwal, A.K. Bhatia, V.S. Bhatia, R. Chugh and V. Vashisht.

Clermont-Ferrand, France, Université Blaise Pascal and IN2P3:
J.P. Alard, A. Baldit, N. Bastid, G. Blanchard, M. Brossard, J. Castor, T. Chambon, P. Crochet, F. Daudon, A. Devaux, P. Dupieux, B. Espagnon, J. Fargeix, P. Force, L. Lamoine, F. Manso, S. Mayade, V. Ramillien, G. Roche, O. Roig, L. Royer, P. Saturnini and G. Savinel.

Coimbra, Portugal, Departamento de Física, Faculdade de Ciências e Tecnologia:
R. Ferreira Marques, P. Fonte[1)] and A. Policarpo.

Columbus, U.S.A., Department of Physics, Ohio State University:
T.J. Humanic, M. Lisa, G. Lo Curto, B.S. Nilsen, G. Paić, D.M. Reichhold and E. Sugarbaker.

Copenhagen, Denmark, Niels Bohr Institute:
I. Bearden, H. Bøggild, J. Gaardhøje and B. Nielsen.

Cracow, Poland, Henryk Niewodniczanski Institute of Nuclear Physics, High Energy Physics Department:
J. Bartke, E. Gładysz-Dziaduś, E. Górnicki, M. Kowalski, K. Papiernik, A. Rybicki, P. Stefański and Z. Wlodarczyk[6)].

Darmstadt, Germany, Gesellschaft für Schwerionenforschung (GSI):
A. Andronic, R. Averbeck, C. Blume, P. Braun-Munzinger, A. Deusser, A. Devismes, J. Eschke, P. Foka, C. Garabatos, B. Kolb, J. Lühning, U. Lynen, A.M. Marin, D. Miskowiec, W.F.J. Müller, C. Neyer, A. Sandoval, H. Sann, H.R. Schmidt, H. Stelzer, W. von Rüden and A. Wörner.

Frankfurt, Germany, Institut für Kernphysik, Johann-Wolfgang Göthe Universität:
C. Bormann, P. Buncic, M. Gaździcki, J. Günther, S. Lange, R. Renfordt, G. Roland, R. Stock and H. Ströbele.

Gatchina, Russia, St. Petersburg Nuclear Physics Institute:
V. Guersenchtein, B. Komkov, V. Mylnikov, V. Nikouline, V. Samsonov, S. Volkov and A. Vorobiev.

Heidelberg, Germany, Max-Planck-Institut für Kernphysik:
F. Ceretto, C. Fuchs, J. Rak and J.P. Wurm.

Heidelberg, Germany, Institut für Hochenergiephysik, Ruprecht-Karls Universität[‡]:
F.O. Lesser, V. Lindenstruth and A.G.E. Mass.

Heidelberg, Germany, Physikalisches Institut, Ruprecht-Karls Universität:
H. Appelshäuser, S. Esumi, K. Filimonov, P. Glässel, B. Lenkeit, N. Herrmann, M.J. Richter, W. Schmitz, J. Stachel, H. Tilsner, J.P. Wessels, T. Wienold and B. Windelband.

Ioannina, Greece, University of Ioannina, Department of Physics:
X. Aslanoglou.

Jaipur, India, Physics Department, University of Rajasthan:
A. Bharti, S.K. Gupta, R. Raniwala and S. Raniwala.

Jammu, India, Physics Department, Jammu University:
S.K. Badyal, A. Bhasin, A. Gupta, V.K. Gupta, L.K. Mangotra, B.V.K.S. Potukuchi, N.K. Rao and S.S. Sambyal.

JINR, Russia, Joint Institute for Nuclear Research:
P.G. Akichine, V.A. Arefiev, V.I. Astakhov, A.A. Baldine, A.M. Baldine, V.D. Bartenev, B.V. Batiounia, I.V. Boguslavsky, M. Bondila, Z.V. Borissovskaia, A.V. Chabounov, G.S. Chabratova, I.A. Chichov, V.I. Datskov, V.K. Dodokhov, L.G. Efimov, A.G. Fedounov, O.A. Golubitsky, B.N. Guouskov, O.I. Iouldachev, V.G. Kadychevsky, I.E. Karpunina, A.D. Kovalenko, V.L. Lioubochits, V.I. Lobanov, G.I. Lykasov, E.A. Matiouchevski, K.V. Mikhailov, D.P. Mikhalev, I. Minaev, P.V. Nomokonov, A.N. Parfenov, I.V. Pouzynin, V.N. Pozdnyakov, A.B. Sadovski, S.V. Semashko, A.E. Senner, I.A. Shelaev, A.V. Sidorov, N.V. Slavine, R.V. Slepnev, G.P. Tsvineva, A.S. Vodopianov, M.B. Yuldasheva, S. Zaporozhets and A.I. Zintchenko.

V. Diomkin[7], V. Kuznetsov[7], V. Shestakov[7], A. Vasiliev[7] and A. Zhakovksy[7].

Ts. Baatar[8], B. Khurelbaatar[8] and R. Togoo[8].

K.G. Akhobadze[9], A.K. Djavrishvili[9], T. Grigalashvili[9], E.S. Ioramashvili[9], A.V. Kharadze[9], L. Khizanishvili[9], T.V. Khuskivadze[9], L.V. Shalamberidze[9] and N. Shubitidze[9].

V. Djordjadze[10], N. Grigalashvili[10], Z. Menteshashvili[10], M. Nioradze[10], M. Tabidze[10] and Y. Tevzadze[10].

Jyvaskyla, Finland, Department of Physics, University of Jyvaskyla and University of Helsinki:
J. Aysto, V. Ruuskanen and W. Trzaska.

Kharkov, Ukraine, National Scientific Centre 'Kharkov Institute of Physics and Technology':
G.L. Bochek, V.F. Boldyshev, I.F. Chervonny, A.N. Dovbnya, V.I. Kulibaba, N.I. Maslov, S.M. Potin, I.M. Prokhorets and A.F. Starodubtsev.

Kharkov, Ukraine, Scientific and Technological Research Institute of Instrument Engineering:
V.N. Borshchov, S.K. Kiprich, O.M. Listratenko, G. Protsay, V.E. Starkov and M. Zamirets.

Kiev, Ukraine, Department of High Energy Density Physics, Bogolyubov Institute for Theoretical Physics, National Academy of Sciences of Ukraine:
T. Hryn'ova, D.E. Kharzeev, V. Palshin, O. Pavlenko, A. Velytsky and G. Zinovjev.

Košice, Slovakia, Institute of Experimental Physics, Slovak Academy of Sciences and Faculty of Science P.J. Šafárik University:
J. Fedoršin, M. Hnatič, A. Jusko, B. Kocper, I. Králik, A. Kravčáková, F. Kriváň, I. Kuľková, M. Lupták, G. Martinská, B. Pastirčák, L. Šándor, J. Urbán, S. Vokál and J. Vrláková.

Kurchatov, Russia, I.V. Kurchatov Institute of Atomic Energy:
V. Antonenko, S. Beliaev, R. Cherbatchev, I. Doubovik, S. Fokine, M. Ippolitov, K. Karadjev, A.L. Lebedev, V. Lebedev, V.I. Manko, G. Mguebrichvili, T. Moukhanova, A. Nianine, S. Nikolaev, S. Nikouline, O. Patarakine, D. Peressounko, I. Sibiriak, A. Vasiliev, A. Vinogradov and M. Volkov.

Legnaro, Italy, Laboratori Nazionali di Legnaro:
R.A. Ricci.

Lisbon, Portugal, Departamento de Física, Instituto Superior Técnico:
J. Barbosa, P. Branco, R. Carvalho, J. Seixas and R. Vilela Mendes.

Lund, Sweden, Division of Cosmic and Subatomic Physics, University of Lund:
L. Carlen, S.I.A. Garpman, H.-A. Gustafsson, P. Nilsson, A. Oskarsson, L. Osterman, I. Otterlund, D. Silvermyr and E.A. Stenlund.

Lyon, France, Institut de Physique Nucléaire de Lyon (IPNL), IN2P3-CNRS et Université Claude Bernard Lyon-I:
M.Y. Chartoire, M. Chevallier, B. Cheynis, D. Essertaize, E. Galichet, E. Gangler, M. Goyot, J.Y. Grossiord, R. Guernane, A. Guichard, D. Guinet, G. Jacquet, P. Lautesse, M. Miguet and S. Tissot.

Marburg, Germany, Fachbereich Physik, Philipps Universität:
F. Eckhardt, V. Friese and F. Pühlhofer.

Mexico City, Mexico, Centro de Investigación y de Estudios Avanzados:
R. Hernández Montoya, G. Herrera Corral, L. Magana, H. Mendez and L.M. Montaño.

Minsk, Belarus, Institute for Nuclear Problems, State University:
A.A. Lobko.

Moscow, Russia, Institute for Nuclear Research, Academy of Science:
K.A. Chileev, S.N. Filippov, Ju.K. Gavrilov, M.B. Goloubeva, M.N. Gotra, F.F. Gouber, T.L. Karavitcheva, A.B. Kourepin, V.D. Laptev, A.I. Maevskaya, V.I. Razine, A.I. Rechetine, N.M. Sobolevsky and N.S. Topilskaia.

Moscow, Russia, Institute for Theoretical and Experimental Physics:
A.N. Akindinov, S.V. Boiarinov, V. Golovine, I.G. Grichouk, A.B. Kaidalov, M.M. Kats, I.T. Kiselev, S.M. Kisselev, E. Lioublev, M. Martemianov, A.N. Martemiyanov, P.A. Polozov, S.A. Pozdniakov, V.S. Serov, A.V. Smirnitski, M.M. Tchoumakov, I.A. Vetlitski, K.G. Volochine, L.S. Vorobiev and B.V. Zagreev.

Moscow, Russia, Moscow Engineering Physics Institute:
V. Grigoriev, V. Kapline, V. Loguinov and M. Strikhanov.

Münster, Germany, Institut für Kernphysik, Westfälische Wilhelms Universität:
D. Bucher, T. Peitzmann, K. Reygers, R. Santo, H. Schlagheck and M. Wahn.

Nantes, France, Laboratoire de Physique Subatomique et des Technologies Associées:
L. Aphecetche, T. Bernier, A. Boucham, S. Bouvier, L. Conin, J.P. Cussonneau, H. Delagrange, D. D'Enterria, B. Erazmus, S. Giliberto, B. Guillet, H.H. Gutbrod, M.S. Labalme, P. Lautridou, F. Lefèvre, M. Le Guay, L. Luquin, L. Martin, G. Martinez, V. Métivier, M.J. Mora, P. Pichot, A. Rahmani, O. Ravel, T. Reposeur, F. Retiere, P. Rivoalan, C.S. Roy, D. Roy, Y. Schutz and A. Tournaire.

NIKHEF, The Netherlands, National Institute for Nuclear and High Energy Physics:
M. Botje[11)], A. Buijs[12)], J.J.F. Buskop[11)], A.P. De Haas[12)], P.K.A. De Witt Huberts[11,12)], R. Kamermans[11,12)], P.G. Kuijer[11,12)], G. Nooren[11)], C.J. Oskamp[12)], A. Van Den Brink[12)], N. Van Eijndhoven[12)] and J. Visschers[11)].

Novosibirsk, Russia, Budker Institute for Nuclear Physics:
A.R. Frolov, I.N. Pestov and M.A. Tiounov.

Oak Ridge, U.S.A., Instrumentation and Controls Division, Oak Ridge National Laboratory:
C.L. Britton, W.L. Bryan, J.W. Walker and A.L. Wintenberg.

Orsay, France, Institut de Physique Nucléaire, Université de Paris-Sud:
L. Bimbot, P.F. Courtat, R. Douet, B. Genolini, H. Harroch, D. Jouan, L. Kharmandarian, Y. Le Bornec, M. Mac Cormick, J. Peyré, J. Pouthas, R. Sellem and N. Willis.

Oslo, Norway, Department of Physics, University of Oslo:
A.K. Holme, L.M. Ingebrigtsen, G. Løvhøiden, B. Skaali, T.S. Tveter and D. Wormald.

Padua, Italy, Dipartimento di Fisica dell'Università and Sezione INFN:
F. Antinori, F. Brandolini, N. Carrer, M. Morando, A. Pepato, F. Scarlassara, G. Segato, F. Soramel and E. Zanoni.

Prague, Czech Republic, Institute of Physics, Academy of Science:
J. Mareš, E. Mihoková, M. Nikl, K. Píška, K. Polák and P. Závada.

Protvino, Russia, Institute for High Energy Physics:
A.M. Blik, M. Bogolyubsky, G. Britvitch, S. Erine, G.V. Khaoustov, I.V. Kharlov, V.N. Kolossov, V. Lichine, S.A. Sadovski, V.D. Samoilenko, P.A. Semenov, V.I. Suzdalev, V. Tikhonov and A. Zviagine.

Řež u Prahy, Czech Republic, Academy of Sciences of Czech Republic, Nuclear Physics Institute:
V. Hanzal, J. Hošek, I. Hřivnáčová, V. Kuschpil, A. Kugler, V. Petráček, M. Šumbera, A. Tlustý, V. Wagner and D. Zákoucký.

Rome, Italy, Dipartimento di Fisica dell'Università 'La Sapienza' and Sezione INFN:
S. Di Liberto, M.A. Mazzoni, F. Meddi, D. Prosperi and G. Rosa.

Saclay, France, Centre d'Etudes Nucléaires, DAPNIA/SPhN:
A. Baldisseri, H. Borel, I. Chevrot, J. Gosset, F.M. Staley and Y. Terrien.

Salerno, Italy, Dipartimento di Fisica Teorica e S.M.S.A., Università di Salerno and Sezione INFN:
G. Grella, M. Guida, G. Romano and T. Virgili.

Sarov, Russia, Russian Federal Nuclear Center (VNIIEF):
S. Abramovitch, V. Basmanov, V. Ianowski, R. Ilkaev, L. Ilkaeva, A. Ivanov, A. Khlebnikov,
E. Kolokolnikov, V. Matiev, S. Nazarenko, V. Pounine, S. Poutevskoi, I. Selin, M. Tarasov,
I. Vinogradov, S. Zhelezov and A. Zhitnik.

St. Petersburg, Russia, Institute for Physics of St. Petersburg State University, Mendeleev Institute for Metrology and Meson Scientific Association:
L.Y. Abramova, V.S. Alexandrov, V.M. Baratov, A.A. Bolonine, M.A. Braun, V.M. Dobulevitch,
G.A. Feofilov, O.N. Godissov, S. Guerassimov, S.N. Igolkine, M.I. Ioudkine, A.A. Kolojvari,
V. Kondratiev, I.A. Novikov, S.V. Potapov, O.I. Stolyarov, T.A. Toulina, F.A. Tsimbal, F.F. Valiev,
V.V. Vetchernine, L.I. Vinogradov and L.F. Vitouchkine.

Strasbourg, France, Institut de Recherches Subatomiques:
L. Arnold, M. Ayachi, J. Baudot, J.D. Berst, J.P. Blondé, D. Bonnet, J.P. Coffin, W. Dulinski,
M. Germain, G. Guillaume, L. Hebrard, Y. Hu, F. Jundt, C. Kuhn, J. Lutz, A. Michalon, F. Rami,
C. Suire and A. Tarchini.

Trieste, Italy, Dipartimento di Fisica dell'Università and Sezione INFN:
V. Bonvicini, A. Gregorio, A. Rachevski, A. Vacchi, L. Valentincic and N. Zampa.

Turin, Italy, Dipartimenti di Fisica dell'Università and INFN:
B. Alessandro, R. Arnaldi, S. Beolé, G. Bonazzola, E. Botta, L. Busso, P.G. Cerello, E. Chiavassa,
P. Cortese, F. Daudo, N. De Marco, A. Feliciello, M. Gallio, G. Giraudo, P. Giubellino,
A. Marzari-Chiesa, M. Masera, G. Mazza, P. Mereu, B. Minetti, O. Morra, A. Musso, D. Nouais,
A. Piccotti, G. Piragino, L. Riccati, E. Scomparin, F. Tosello, E. Vercellin and A. Werbrook.

Warsaw, Poland, Soltan Institute for Nuclear Studies:
D. Czerwinski, A. Deloff, K. Karpio, S. Kozak, L. Lukaszek, H. Malinowski, T. Siemiarczuk,
G. Stefanek, L. Tykarski and G. Wilk.

Warsaw, Poland, University of Technology, Institute of Physics:
J. Buryk, J. Grabski, P. Kindziuk, A. Kisiel, P. Leszczynski, A.M. Maliszewski, J.M. Mazur,
T.J. Pawlak, W.S. Peryt, J. Pluta, M. Przewlocki, S. Radomski, A.M. Roszczewski, M. Sarzynski,
P. Skowronski, P. Stepien and P. Szarwas.

Wuhan, China, Institute of Particle Physics, Huazhong Normal University:
X. Cai, Y. Hu, F. Liu, L. Liu, H. Wang and D. Zhou.

Yerevan, Armenia, Yerevan Physics Institute:
R. Asatryan, M. Atayan, R. Avakian, V. Danielyan, V. Gavalian, A. Grigorian, S. Grigoryan,
H. Gulkanyan, R. Hakobyan, V. Kakoyan, S. Mehrabyan, L. Parlakyan, R. Shahoyan and H. Vardanyan.

Zagreb, Croatia, Ruder Bošković Institute:
D. Ferenc, A. Ljubičić and T. Tustonic.

[1)] Also at CERN, Geneva, Switzerland
[2)] On leave from Seasoft, Catania, Italy.
[3)] On leave from JINR, Dubna, Russia.
[4)] On leave from IHEP, Protvino, Russia.
[5)] On leave from Budapest University, Hungary.
[6)] Institute of Physics, Pedagogical University, Kielce, Poland.
[7)] Research Centre for Applied Nuclear Physics (RCANP), Dubna, Russia.
[8)] Institute of Physics and Technology, Mongolian Academy of Sciences, Ulaanbaatar, Mongolia.
[9)] Institute of Physics, Georgian Academy of Sciences, Tbilisi, Georgia.
[10)] High Energy Physics Institute, Tbilisi State University, Tbilisi, Georgia.
[11)] Foundation of Fundamental Research of Matter in The Netherlands.
[12)] Utrecht University, Utrecht, The Netherlands.
[‡)] Applying to join ALICE.

Acknowledgements

It is a pleasure to acknowledge the contribution given by S. Weisz for his help in the topics related to the optics of the beam and the layout of the insertion region. We are also indebted to G. Trinquart and H. Delor for help in preparing the drawings of the beam line elements and the integration of the ZDC detectors.
The collaboration wishes to thank all the technical and administrative staff (in particular S. Barras and S. Stappers) involved during the preparation of this TDR. We also thank M. Jouhet, J. Navarria and G. Prost, from the Desktop Publishing Service, for their professional help with the editing.

Contents

1 Introduction

1.1 The ALICE experiment

The ALICE collaboration has proposed to build a general-purpose detector, dedicated to the study of heavy-ion collisions at the LHC [1]. The experiment will consist of:

- a central barrel, embedded in a large magnet, covering the pseudorapidity region $-1 < \eta < 1$, mainly devoted to the study of hadronic signals and dielectrons;
- a forward detector, dedicated to the study of muon pair production in the interval $2.5 < \eta < 4$;
- other forward detectors ($\eta > 4$), namely a multiplicity counter array close to the interaction region, and two sets of zero-degree calorimeters located far downstream in the machine tunnel, which will provide fast information about the centrality of the collisions.

In heavy-ion interactions, the event-by-event determination of the collision's centrality plays a basic role; it is used at the trigger level to enhance the sample of central collisions and, more generally, to estimate the energy density reached in the interaction. It is therefore important to have several detectors which can provide a fast and reliable characterization of the event geometry.

The primary aim of the experiment is to establish and analyse the formation of a Quark–Gluon Plasma (QGP) in ion–ion collisions. Many QGP signatures manifest themselves as a threshold behaviour of certain observables (e.g. production of charmonia and bottomonia states, strangeness) as a function of the energy density, estimated through the centrality of the collision; a good resolution on the centrality measurement is therefore essential, in order to properly probe the existence of such a threshold, which could otherwise be smeared out.

1.2 Measurement of the collision's centrality

The energy E_S carried away by the non-interacting (spectator) nucleons is the measurable quantity most directly related with the centrality of the collision. It allows a direct estimate of the number of interacting (participant) nucleons N_p through the simple relation:

$$N_p = A - E_S/E_A \ ,$$

where A is the mass number of the ion and E_A is the beam energy per nucleon. Simple considerations link the average number of participant nucleons with the impact parameter b of the collision, in the case of identical nuclei. A more detailed calculation in the framework of the Glauber theory [2] gives:

$$N_p(\vec{b}) = \int d^2s \ \{AT_A(\vec{s})[1-(1-\sigma_N T_B(\vec{b}-\vec{s}))^B] + BT_B(\vec{b}-\vec{s})[1-(1-\sigma_N T_A(\vec{s}))^A]\}$$

where A and B are the mass numbers of the colliding nuclei, $T_{A,B} = \int dz \, \rho_{A,B}(z, \vec{s})$ are the nuclear profile functions, σ_N is the nucleon–nucleon inelastic cross-section, and $\vec{s}$ is a two-dimensional vector in the transverse plane of the collision. The result, showing the monotonic trend of N_p vs b, can be seen in Fig. 1.1 (line). A similar calculation can be performed using a nucleus–nucleus event generator, such as VENUS [3], which also allows the size of the intrinsic fluctuations on the number of participant nucleons at fixed impact parameter (filled circles) to be investigated. The two calculations agree well, showing that the determination of the centrality of a nucleus–nucleus collision through a measurement of the number of spectator nucleons is conceptually possible and largely model-independent.

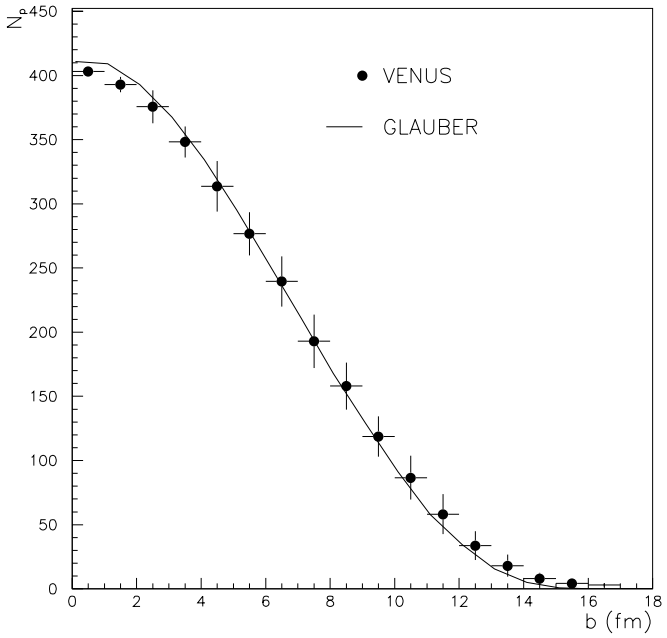

Figure 1.1: The correlation between the impact parameter b and the number of participant nucleons N_p for Pb-Pb collisions at LHC energies.

1.3 ZDCs: fixed-target experiments

At fixed-target experiments the spectator nucleons, which fly away in the forward direction, are usually intercepted by means of zero degree calorimeters (ZDCs), placed on the beam axis, providing a measurement of E_S. This technique has been successfully adopted by several SPS heavy-ion experiments, such as WA80, NA49, and NA50. It has been shown that the measurement of projectile spectators in a ZDC is well correlated with other centrality estimators (transverse energy around midrapidity, charged hadron multiplicity). The resolution on the impact parameter, of the order of $\sim 10\%$ over a large range of centralities, has been found to be dominated by the intrinsic fluctuations on the number of spectator nucleons.

The use of ZDCs in a fixed-target environment poses non-negligible technical problems from the point of view of the detector's design; in fact, such devices also intercept the outgoing ion beam and must therefore be radiation hard and fast. These requirements were of course most compelling for high-luminosity experiments ($>10^7$ incident ions/s), such as NA50, which had to use quartz fibre calorimetry as the detection technique [4]. Other experiments, running at beam intensities around 10^6 ions/s successfully used more classical techniques such as Pb/Fe-scintillator (NA49) [5] or U-scintillator (WA80) [6] devices.

1.4 ZDCs for ALICE

The design of devices for the detection of spectator nucleons for an ion collider experiment, like ALICE, differs significantly with respect to a fixed-target environment. Typically the beams are deflected by means of two separation dipoles at a certain distance from the interaction point (IP), of the order of 50 m in the case of the ALICE IP, in order to reach the nominal distance (188 mm for the LHC) between the beams. These magnets will also deflect the spectator protons, separating them from the spectator

neutrons, which basically fly away at 0°. It is therefore conceptually possible to place between the separation dipoles, on the two sides of the IP, a set of two devices; one of them, positioned between the two beams to intercept the spectator neutrons, and the other one, external to the outgoing beam, to collect the spectator protons.

1.4.1 Detection technique: quartz fibre calorimetry

The design of ZDCs in the LHC environment has to satisfy various technical issues.

Firstly, the amount of space between the separating dipoles which can be allocated to ZDCs is quite small; the transverse dimensions of the neutron device cannot in any case exceed the distance between the two beam pipes in that region ($\sim$ 88 mm), meaning that an extremely compact object is needed. The same remark also applies to the proton device, as the spot of the spectator protons is found to be separated from the outgoing beam by only a few cm. Secondly, the ZDCs, even if they do not intercept the beams (as in fixed-target experiments), will operate at a high radiation level; the deposited dose in the neutron calorimeter is estimated to be $\sim$ 1 Mrad/day, at a luminosity $\mathcal{L} = 10^{27}$ cm^{-2} s^{-1}.

Because of these constraints we have been obliged to choose as the detection technique for the ALICE ZDCs quartz fibre calorimetry, which allows compact and radiation-hard devices to be built, meeting the requests outlined previously. After an exploratory R&D phase, quartz fibre calorimetry has been successfully used for the ZDC of the NA50 experiment, where a device made of quartz fibres embedded in a tantalum matrix, of dimensions $5 \times 5 \times 65$ cm^3, has worked in an environment 10 times harsher than the ALICE one in terms of radiation levels. The measured energy resolution

$$\frac{\sigma(E)}{E} = \frac{3.39}{\sqrt{E(\mathrm{GeV})}} + 0.062 \ ,$$

extrapolated to LHC energies is already $< 10\%$ for a few incident nucleons, corresponding to very central events. Such values are considerably smaller than the intrinsic fluctuations on the number of spectators detected by a single device (expected to be of the order of 14% at $b \sim 4$ fm). Therefore, quartz fibre calorimeters are a reasonable choice also from the point of view of the energy resolution necessary for measuring the spectator nucleons at ALICE.

The first part of Chapter 2 deals with a short introduction to quartz calorimetry. The basic components of this technique (fibres, passive materials, light detectors) and some essential physics concepts (Cherenkov effect in optical fibres) will be discussed.

After the submission of the ALICE technical proposal, we started an R&D programme especially devoted to the optimization of the performance of quartz fibre calorimetry, taking into account the constraints of the ALICE environment. Various prototypes have already been tested in the CERN SPS test beams; the results obtained so far will be discussed in detail in the second part of Chapter 2. The performances of the NA50 ZDC will also be reviewed.

1.4.2 Detector design

The optics of the LHC beams in the insertion regions, where the ZDCs have to be placed, is rather complicated; it includes, apart from the separation dipoles, other magnetic elements, mainly quadrupole triplets, which can distort to a considerable extent the trajectories of charged particles, such as spectator protons, as they have a different magnetic rigidity than that of the beam.

Furthermore, the geometry foreseen for the magnets and the beam pipes includes elements which could generate a non-negligible background for spectator neutron detection.

Therefore, in order to finalize the study of the geometry of the detectors, a detailed simulation of the ALICE insertion region must be performed. As the LHC optics, as well as the design of the various elements connected with the vacuum systems (beam pipes, flanges) is still evolving at the time of drawing up this TDR, the most up-to-date information (corresponding to version 6 of LHC optics) has been used whenever possible.

The simulation, which will be described in detail in the first part of Chapter 3, makes use of GEANT 3.21 [7] for the description of the geometry of the interaction region and of the ZDCs; the same package has also been used as tracking engine. The dynamics of the collision has been simulated using both VENUS 4.12 [3] and HIJING 1.35 [8] as event generators; physics aspects which are not included in the generators but are relevant for the design of the detector (Fermi motion of spectator nucleons, incomplete spectator fragmentation) have also been included.

As a result it has been possible to calculate, as a function of the distance from the IP, the transverse size and position of the spectator neutrons and protons throughout the insertion region. This information is essential in order to choose the best suited region to place the ZDCs as well as their dimensions. Tracking the spectator nucleons in the zone from the IP to the ZDCs, it has been possible to look for the regions where a loss of spectators can be expected, mainly because of interaction in the coils of the magnets and/or the beam pipes. Whenever such losses are so severe that they significantly degrade the performance of the detector, modifications in the layout of the insertion regions have been proposed.

The conceptual and technical design of the detectors, driven by the simulation and by the R&D results will be discussed in detail in the second part of Chapter 3; hereafter we briefly summarize the conclusions. Figure 1.i (in colour, see page 7) shows the layout of the insertion region with the proposed geometry for the ZDCs.

1.4.3 The neutron ZDCs

The neutron ZDCs will be placed at a distance $d_{ZN} = 116.13$ m from the IP, with a displacement of about 1 cm off the horizontal plane of the machine, to account for the 100 μrad/beam crossing angle of the two beams at the IP. At this point the size of the spot of the spectator neutrons, at a 1σ level, is about 0.6×0.6 cm^2. A device of dimensions $7 \times 7 \times 100$ cm^3, made of quartz fibres embedded in a tantalum matrix, allows 80% of the shower generated by spectator neutrons to be contained. The fibres have a core diameter of 365 μm and are oriented at 0° with respect to the beam axis. The quartz to absorber volume ratio foreseen is 1/22. The resolution for a 2.7 TeV neutron is 10.5%, according to simulation. Two calorimeters will be used, one for each side of the IP.

1.4.4 The proton ZDCs

The proton ZDCs will be placed at a distance $d_{ZP} = 115.63$ m from the IP. At this point the size of the spot of the spectator protons is no longer gaussian, mainly because of the influence of the inner triplet of quadrupoles, which results in a de-focussing action in the horizontal plane; 90% of the protons are contained in an area 12.6×2.8 cm^2, centered at 19 cm from the beam axis, on the outgoing beam side. To obtain a shower containment and an energy resolution similar to that of the neutron ZDCs, we will use two devices of $20.8 \times 12 \times 150$ cm^3, made of quartz fibres embedded in a brass matrix, centered at 19 cm from the beam axis. The fibres have a core diameter of 550 μm and are oriented at 0° with respect to the beam axis. The quartz to brass volume ratio foreseen is 1/65.

For both calorimeters the Cherenkov light produced in the quartz fibres will be driven by the fibres themselves to PMTs with a borosilicate window. The expected photoelectron yield is about 300/TeV.

Finally, the calibration of the ZDCs and the monitoring of their response stability is essential in order to safely control the energy response of the devices. An off-line calibration of the ZDCs, at the highest available energies, is foreseen after the assembly phase. The availability of an ion beam, at the SPS or RHIC at that time, would allow a detailed study of the linearity of the response as a function of the number of incoming nucleons. During data-taking, a LED system will allow the time evolution of the PMT gain as well as the radiation damage in the fibres to be monitored, as will be discussed in Section 3.10 on page 64.

1.5 The ZDCs in the ALICE trigger system

The ALICE trigger system is foreseen to work on three levels (L0, L1, L2). The signals from the ZDCs, yielding information on the centrality of the event are used at the L1 level, together with the PMD signals and with information from the dimuon arm. The L1 decision is taken after about 2.4 μs; this delay is mainly due to the time-of-flight and to the transmission of the signals along the cables. By selecting appropriate thresholds on the analog sum of the amplified ZDCs signals, it is possible to select windows in the impact parameter b of the collision. The resolution on the centrality, expected to be of the order of 10% for all but the most central events, allows the use of at least four thresholds, resulting in five centrality bins at the trigger level. Details of the trigger layout are given in Section 3.8 on page 59, whilst the trigger efficiency is discussed in Section 4.7 on page 76.

1.5.1 The layout of the interaction regions: open problems

In order to reach the ZDCs the spectator neutrons and protons have to fly over more than 100 m, crossing various elements of the LHC beam line. Sofar, the only critical region seems to be the one corresponding to the separator dipole D1. The spectator protons entering this magnet will, because of their lower magnetic rigidity, suffer a stronger deflection than the Pb ions. With the presently designed size of the D1 aperture, d_{D1} = 7.3 cm, about 13% of the spectator protons will interact in the coil of D1, resulting in a loss of performance for the proton ZDC. As this parameter (aperture of D1) appears to be critically connected with the correct tracking of the spectator protons, a study of the performance of the detector as a function of the D1 aperture has been carried out. Its results, discussed in Section 3.3.1 on page 42, show that any further decrease in the opening of D1 will lead to a severe loss of spectator protons. The implications in terms of performance of the detector are discussed in Section 4.5 on page 71.

1.6 Performance of the detector

The physics quantity measured in ZDCs is the number of spectator nucleons, which is closely correlated to the geometry of the collision (i.e. to the impact parameter b). A good estimator of the performance of the detector is therefore the resolution on b. The simulation described in Chapter 3 allows such a study to be performed, i.e. to determine σ_b/b as a function of the centrality.

This quantity depends on the physics of the collision (through the fluctuations on the number of spectators at a fixed centrality), on the finite resolution of the detectors, as well as on possible spectator losses through the beam line. Using VENUS or HIJING to estimate the physics fluctuations, the GEANT simulations of the detectors and the present set-up of the insertion region (version 6 of the LHC optics) we reach the result shown in Fig. 1.2, i.e. $\sigma_b/b \leq 8\%$ for $b \geq 4$ fm. For very central events the intrinsic fluctuations on the number of spectators tend to deteriorate the resolution.

A good resolution on the centrality is essential in order to detect QGP signatures which are expected to be seen as a discontinuity in certain observables (e.g. charmonia or bottomonia cross-sections) at a certain value of b or of related quantities.

Typically, a step behaviour due to a phase transition, occurring at a certain b, will result in a drop with a slope comparable with σ_b. The better the resolution on σ_b, the easier it will be to discriminate between a step transition and hadronic mechanisms, which usually produce smooth variations, as a function of the centrality, in the observable quantities.

These topics will be investigated in Chapter 4.

1.6.1 The fragmentation of the spectator nucleons

The quality of a measurement of the centrality via the nucleon spectators can depend to a certain extent on the fragmentation of the colliding nuclei. Clearly, if the fragmentation is complete, i.e. spectator neutrons

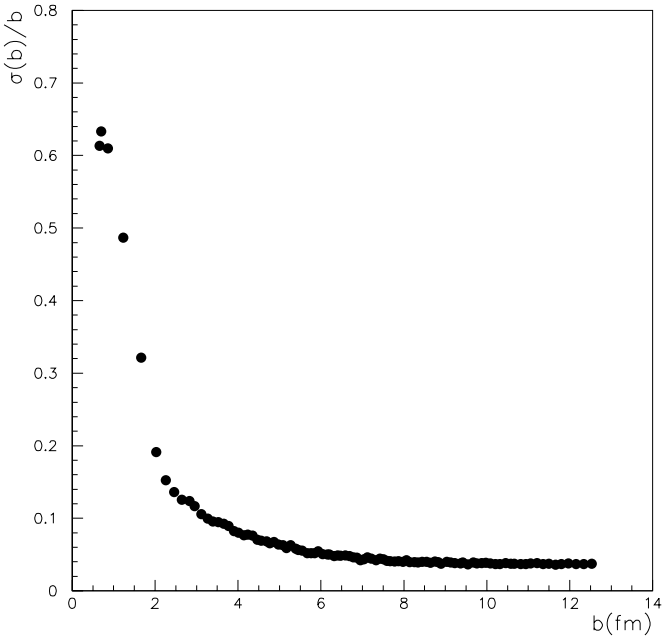

Figure 1.2: Resolution on the impact parameter for the ALICE ZDCs.

and protons fly away as free particles, it is in principle possible to collect all of them in ZDCs. On the other hand, if spectator nucleons are bound into fragments with a charge/mass ratio similar to the one of the beam, they are transported together with the beam itself and cannot be measured. Unfortunately, up to now the issue of spectator fragmentation has been investigated in detail only at rather small beam energies (of the order of 1 GeV/nucleon) [9], while much less information exists for SPS energies [10]. In Section 4.6 on page 72 the existing information on this topic will be reviewed and the influence of spectator fragmentation on a measurement at a collider experiment will be investigated and discussed. As a result it will be shown that the energy measured by the ZDCs is monotonically correlated with b only for $b \leq 11$ fm. Beyond this value of the impact parameter the incomplete fragmentation of the spectators results in a severe loss of performance of the detector. However, such peripheral collisions should already be rejected by the L0 trigger.

1.6.2 The ZDCs as a luminosity monitor

Apart from their use in the determination of the centrality of the collision, ZDCs can monitor the LHC luminosity. It is well known that the cross-section for electromagnetic dissociation of a Pb nucleus at the LHC exceeds the hadronic cross-sections by more than one order of magnitude, and will be one of the limiting factors for the beam lifetime. We plan to measure mutual Coulomb dissociation, which will result in a coincidence of one neutron signal on the two ZDCs, as will be explained in Section 4.8 on page 78. The cross-section for this process can be calculated using the Weizsacker–Williams formalism, leading to $\sigma^{m}_{\mathrm{Pb}} = 0.53$ b [11]. The incertitude on the determination of σ^{m}_{Pb}, and consequently on the luminosity, are of the order of a few per cent. The use of ZDCs in such a context is foreseen at RHIC [12].

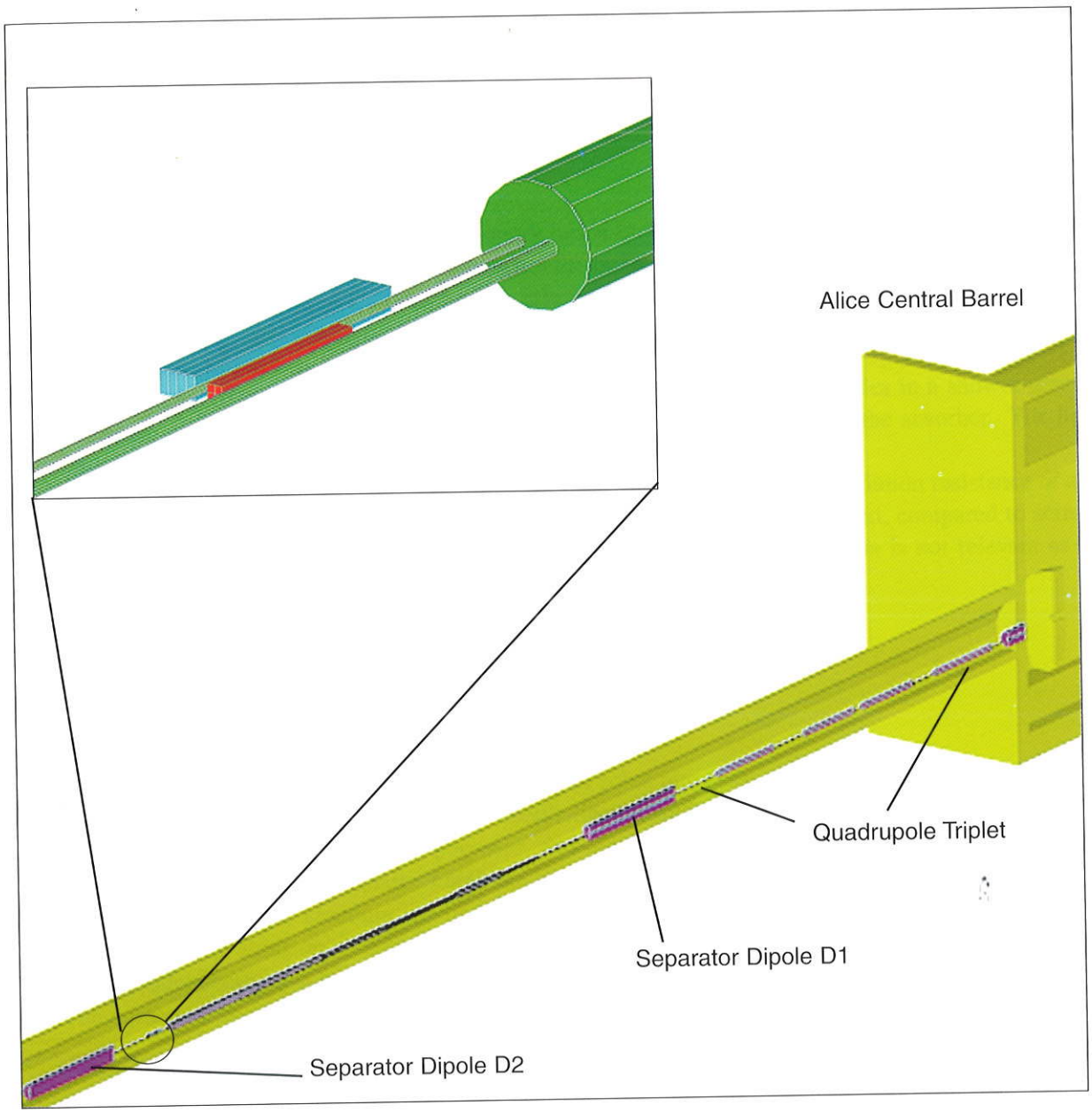

Figure 1.i: Schematic layout showing the ZDC location in the beam line.

2 R&D, prototypes, test results

2.1 Introduction

The first ideas about a new type of calorimetry based on the detection of Cherenkov light generated in quartz fibres were developed by P. Gorodetzky, with the intent of developing detectors working for heavy-ion physics as Zero Degree Calorimeters or calorimeters to be used in very forward regions ($\eta > 2.5$) for the LHC (pp) experiments. Much work on this subject was carried out within the CERN RD40 collaboration, formed to explore the capabilities of the optical fibre calorimetry technique [1–7]. The basic principle of quartz fibre calorimetry is rather simple: the charged particles in a shower generated in a dense absorber produce Cherenkov light in quartz fibres interspersed in the absorber. The light is optically guided by the same fibres towards the photodetectors.

The basic motivations for the development of this new technique are the radiation resistance of quartz and the intrinsic speed of the Cherenkov effect. The relatively small light yield, compared to scintillating fibres, results in a greater energy resolution stochastic term. However, this is not relevant as these detectors are intended to work in a very high energy range.

2.2 Basic components

2.2.1 Fibres

Large diameter ($> 100\,\mu$m) step index silicon fibres come into three categories: sylastic, plastic cladding (both are relatively cheap), and fluorine-doped silicon cladding (very expensive). All of them are used primarily for military and medical purposes, and are usually operated in the visible to infrared wavelengths; as the fluorinated quartz fibres are normally used in the infrared region, they have a thick cladding. Outside the cladding the fibres normally have a coating or buffer to protect the fibre itself against cladding abrasion.

For calorimetry, it is better to use fibres with a thin buffer or even unbuffered (with thicker cladding). The numerical aperture,

$$NA = \sqrt{n^2_{\text{core}} - n^2_{\text{cladding}}}\,,$$

is generally 0.22 for fluorine-doped silica cladding, 0.37 for plastic (fluorine-doped PMMA) cladding, and 0.4 for fibres with sylastic cladding. The numerical aperture is equal to the sine of the nominal limiting exit half-angle for meridional rays (i.e. those rays whose paths are lying in a plane which intersects the fibre's axis); for example, the exit angle corresponding to NA = 0.22 is 12.7°.

The transmittance of the quartz in the visible region remains constant up to 20 Grads [8]. Measurements performed using the 2 MeV electron beam of the Vivirad irradiation facility in Strasbourg on different types of quartz fibres [7] have shown that ultra-pure quartz fibres with a fluorinated quartz cladding show no loss after 2.5 Grad. This type of fibres, manufactured by Spectran, was used in the NA50 ZDC calorimeter for more than three years and they still work satisfactorily, after an integrated dose of $\sim$ 10 Grad, as explained in Section 2.6.

2.2.2 Absorber

The passive material in a hadronic calorimeter should have a small interaction length; the most commonly used materials are copper (λ_i = 15 cm) or lead (λ_i = 17.1 cm). As the material must be cut into sheets and grooved to host the fibres, it should be easily machinable. Very high density materials like

tantalum, tungsten or tungsten alloys can be chosen when the hadronic shower needs to be contained in a particularly limited space.

2.2.3 Light detectors

The dominant part of Cherenkov light is emitted in the UV domain; therefore, working with UV-sensitive photon detectors will maximize photon statistics and reduce the stochastic term in the resolution. Nevertheless, the light yield is normally high enough to compensate the loss caused by the use of standard photocathodes because the energy of the particles hitting the ZDCs is very high. Comparing the simulated response of these two photocathodes for a given calorimeter geometry and for a hadron of 2760 GeV, we found 0.3 photoelectrons per GeV produced at the PMT with a borosilicate window, and 0.8 photoelectrons per GeV when the quartz window is used. The resolution stays constant within the simulation uncertainty.

2.3 The Cherenkov effect in optical fibres

2.3.1 Production and transmission of Cherenkov photons in fibres

The light yield of the Cherenkov effect is given by the formula:

$$\frac{d^2N_{ph}}{dLd\lambda} = 2\pi\alpha z^2 \, \frac{\sin^2\theta_c}{\lambda^2} \, ,$$

where α is the fine structure constant, λ is the wavelength, L is the path of the particle with charge z through the medium, and θ_c is the Cherenkov angle; the Cherenkov light is emitted along a cone with an angular opening given by

$$\cos\theta_c = \frac{1}{n\beta} \, ,$$

where $\beta = v/c$, and n is the index of refraction of the medium.

The refraction index of the quartz as a function of the wavelength, in the interval between 180 and 600 nm, ranges from 1.56 down to 1.46; in this frequency region the opening of the Cherenkov cone for $\beta = 1$ particles ranges from 46.7° to 50.1°.

The fibre's light output depends, for a fixed wavelength and a fixed particle velocity, on the direction of the particle with respect to the fibre's axis (because Cherenkov photons are emitted along the surface of a cone), and on the distance of the closest approach between the particle's trajectory and the fibre's axis (impact parameter). The distribution of photons, produced by a $\beta = 1$ particle, trapped inside a fibre and transmitted to one edge of the fibre is shown in Fig. 2.1, as a function of the impacting angle α and impact parameter b. The fibre considered has a core diameter equal to 365 μm and NA = 0.22; the wavelength distribution of the photons produced is multiplied by the nominal quantum efficiency of a Philips XP2020 photocathode. The maximum of the distribution occurs at $\alpha \sim 40° - 50°$. At low particle momentum, the decrease of β produces a decrease of the Cherenkov angle, and therefore the maximum of the distribution shifts towards smaller angles. For β below 0.7, the photons are emitted almost along the particle trajectory and only those particles which are nearly parallel to the fibres produce light that reaches the end of the fibre.

In a calorimeter, all the values of the impact parameter b, have the same probability. The distribution of the angles of the shower particles with respect to the fibre's axis depends on the orientation of the fibres. In Fig. 2.2 (top) we plot this distribution for fibres placed at 0° with respect to the initial particle trajectory (2760 GeV proton). Folding this last distribution with those of Fig. 2.1 and integrating over all the impact parameters, we obtain the spectrum of the number of photoelectrons produced at the photocathode of the PMT considered. In Fig. 2.2 (bottom) we show the light output as a function of the impacting angle α. It is clear that the particles must cross the fibres within a narrow angular window around 45° in order to produce the maximum signal.

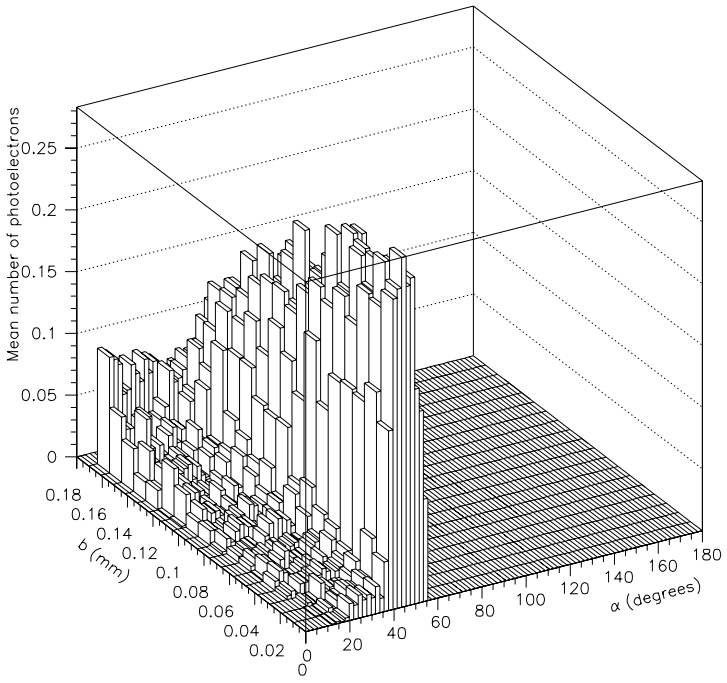

Figure 2.1: Distribution of the number of photons that exit the fibre (ø = 0.365 mm, NA = 0.22) as a function of the incident angle α and impact parameter b of a particle with $\beta = 1$ crossing the fibre.

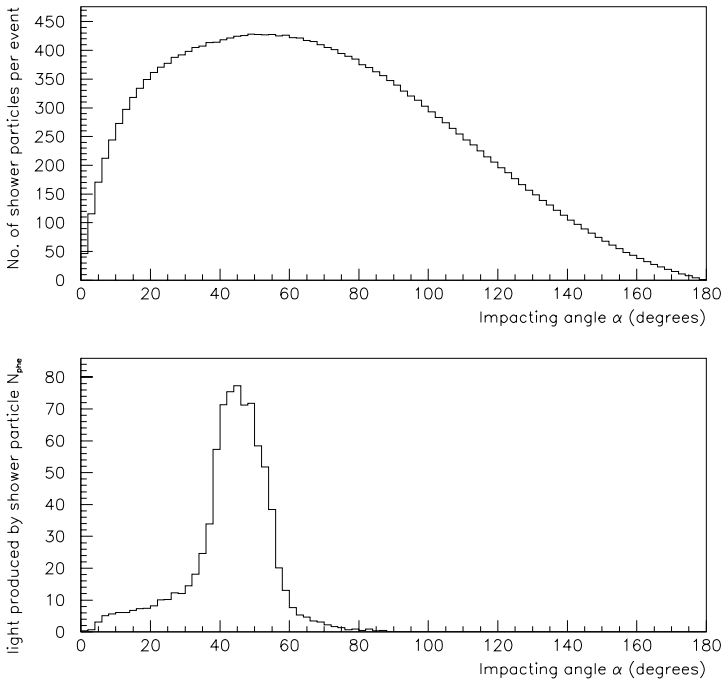

Figure 2.2: Top: distribution of the impacting angles α of the shower particles, originated by a primary 2760 GeV proton, producing Cherenkov light in a calorimeter with fibres at 0°. Bottom: light production as a function of α.

2.3.2 Monte Carlo simulations

The description of the ZDC in the ALICE environment is implemented into the GALICE simulation code [9], based on GEANT 3.21. The program can logically be divided into two parts.

The first part tracks the particles produced and the spectator nucleons through the beam elements up to the calorimeters, and will be detailed in Section 3.3 on page 41.

The second part is the simulation of the shower inside the calorimeters. For the hadronic interactions, we use the GHEISHA package [10].

Cherenkov light production in the fibres and the transport of light to the PMT is determined using a separate program. This program produces the distributions of Cherenkov light yield in optical fibres and creates sets of data tables. The program takes into account the numerical aperture of the fibre, its attenuation length as a function of the wavelength of the light, and the quantum efficiency of the photocathode of the PMT coupled to the fibres. The shower particles are tracked by GEANT in the absorber until they traverse a fibre. The impacting angle α, the particle velocity β, and the distance from the fibre axis b are then used to obtain the photon yield directly from the tables, thus reducing the required total CPU time. A random number with Poissonian distribution is used to determine the number of photoelectrons produced at the photocathode of the PMT.

An important issue about the simulation programs is the choice of the threshold values used in the GEANT package. As the light is due essentially to the electromagnetic part of the hadronic shower, the resolution strongly depends on the value of the GEANT cuts on the γ and $e^{\pm}$ energies. Increasing the value of the threshold for tracking the gammas and electrons saves a substantial amount of computing time, but can give a wrong prediction of the experimental resolution. As an example, for a given geometry the resolution for 2760 GeV protons varies from 7.6% for an $E_{\rm cut}^{em} = 10$ MeV, to 9.7% for an $E_{\rm cut}^{em} = 1$ MeV. Therefore we choose $E_{\rm cut}^{em} = 1$ MeV to ensure a proper treatment of the e.m. shower.

2.4 Speed of response and inherent rate capabilities

Cherenkov radiation, on which the sampling process is based, occurs in a much shorter time scale than the propagation of a hadronic shower through a calorimeter. The limiting factor in speed and rate capabilities of the quartz fibre calorimetry technique is the light detector read-out technology. The optical signal is combined with the response shape of the light detector and with the cable band-pass.

Figure 2.3 shows a typical detector (NA50 ZDC) response to a single incident Pb ion of 158 A GeV/c using a 6-stage Philips XP2242-B PMT, taken with a Tektronix TDS620 digital oscilloscope after a total cable length of 200 m. The PMT signal was in fact amplified by a factor of 10 by means of a fast linear amplifier (LeCroy 612A), after 43 m of C-50-11-1 coaxial cable, and then delayed by 157 m long coaxial cables. The signal has a very short duration: the return to baseline is within 13 ns and the rise time is 3 ns.

The delayed or late hadronic energy deposition (proton recoils, γ-neutron capture, γ secondary fission) for dE/dx based calorimeters, as reported in Ref. [11], produces no signal in a quartz fibre calorimeter and therefore does not affect signal speed. For ALICE no signal processing will be necessary in order to isolate signals from different bunch crossings, separated by 125 ns.

2.5 Proton calorimeter prototypes

Two prototypes of the proton calorimeter, named ZP2 and ZP7, have been constructed with different geometrical and mechanical characteristics, which are summarized in Table 2.1. They are both equipped with polymehtylmethacrylate (PMMA) fibres, equally spaced and parallel to the beam axis. The passive matrix was made of copper for the ZP2 prototype, and brass for ZP7.

The ZP2 (ZP7) prototype was assembled by superimposing 40 (26) identical plates 4 mm (6 mm) thick, grooved on the upper side, where the fibres are located. The plates are stacked to form a paral-

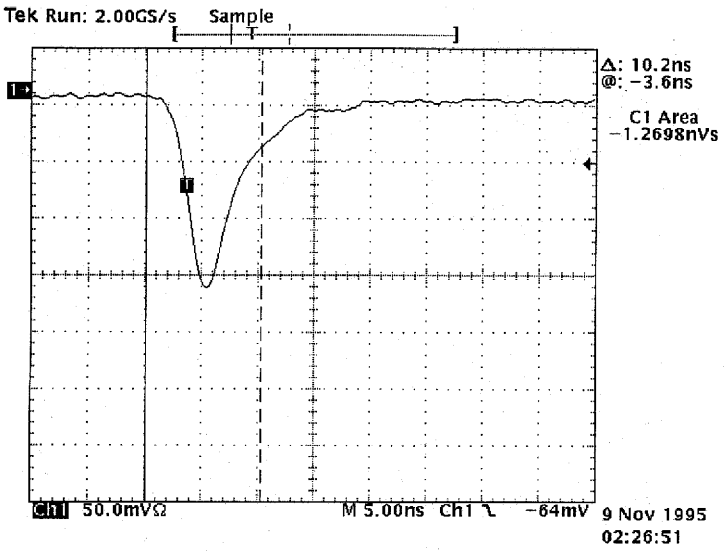

Figure 2.3: Digital oscilloscope plot of the NA50 ZDC detector response to a 158 A GeV/*c* incident Pb ion, using a Philips XP2242B PMT readout and after a total cable length of 200 m.

lelepiped having dimensions of $16 \times 16 \times 150$ cm^3. The fibre spacing has to be smaller than the radiation length of the passive matrix, in order to avoid a loss of the shower electrons, which could be absorbed in the passive material before giving a signal. The transverse dimensions are those foreseen in the TP.

The shower development in the two materials is similar (see Table 2.2). The parameters governing the longitudinal and lateral shower dimensions are small enough to fulfil the requirements for the proton calorimeter. We have chosen two different materials in order to test their mechanical properties. Both are mechanically resistant, easily machinable, and relatively cheap. Another advantage is the low neutron production probability, due to the low Z.

The length of each fibre is 250 cm: the first 150 cm, inside the absorber matrix, represent the active part of the calorimeter, the following 100 cm, bent at 90° with respect to the beam axis, act as a light guide. The Cherenkov light is produced in the fibres and transmitted by multiple reflection to the photocathode of the photomultipliers, located about 1 m from the beam axis, to reduce background caused by

Table 2.1: Characteristics of the two calorimeter prototypes.

	ZP2	ZP7
Dimensions	$16 \times 16 \times 150$ cm^3	$16 \times 16 \times 150$ cm^3
Filling ratio	1/80	1/85
Absorber	copper	brass
Number of plates	40	26
Plate thickness	4 mm	6 mm
fibre type	PMMA	PMMA
Diameter	500 μm	750 μm
Number of fibres	1600	676
fibre spacing	4 mm	6 mm
Number of PM	4	2

Table 2.2: Characteristics of absorber materials.

	ZP2	ZP7
Absorber	Copper	Brass
ρ	8.96 g/cm^3	8.28 g/cm^3
X_0	1.43 cm	1.5 cm
λ_{int}	15.06 cm	18.4 cm

Table 2.3: Filling ratios for different combinations of the PM signals for the two prototypes.

Number of PMT	ZP2	ZP7
1	1/325	1/170
2	1/162	1/85
3	1/108	
4	1/80	

the shower particles impinging on the PMT's window. Figures 2.i and 2.ii (in colour, see page 37) show the front face and the perspective views of the ZP2 prototype.

There are four photomultipliers for ZP2 and two for ZP7. The connection to the fibres is such that each PMT collects the light from a subset of fibres uniformly distributed in the passive material (see Fig. 2.4); in this way, considering one or more PMTs, we obtain different quartz/absorber filling ratios, as reported in Table 2.3. For the purposes of this prototype test, the use of the (10 to 20 times) more expensive quartz Cherenkov fibres is not necessary, as the radiation damage is negligible. In this context, the main difference between the two types of fibres is the numerical aperture (NA), 0.50 for the PMMA and 0.22 for the quartz. On the other hand, the quartz fibres have been extensively tested in the radiation-rich environment of lead-ion beams.

Figure 2.4: Connection of the fibres to the photomultipliers for the ZP2 and ZP7 prototypes.

2.5.1 Off-beam tests and calibrations

Light attenuation in fibres

Light attenuation in fibres was measured at different wavelengths using a monochromator. Measurements were made at CSELT (telecommunications research centre in Torino, Italy). A sample of the plastic fibres used in the construction of the ZP2 prototype was analysed. The measurement was performed with the cut-back technique. Light transmission was first measured for a fibre several metres long, then the fibre was cut to a few metres length, and light transmission was measured again. In this way it is possible to avoid spurious effects caused by the coupling of the fibre with the light source and the spectral response of the photodetector. In Fig. 2.5 we plot the measured light attenuation as a function of the wavelength.

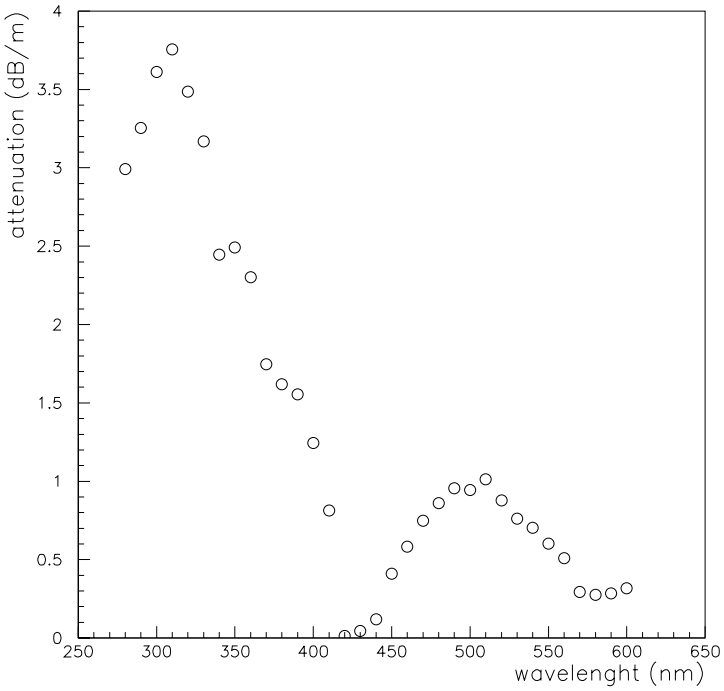

Figure 2.5: Light attenuation of a sample of fibres as a function of the wavelength.

Measurement of the PMT gain

To obtain the absolute light yield of our detector and make a comparison with Monte Carlo simulations, we measured the gain of the Philips XP2020 photomultipliers that were used in the 1998 test. We used an optical bench with a spark light source, whose intensity was very stable during the measurement period. Light emitted was filtered and attenuated by a set of Wratten gelatin filters in order to reach the single photoelectron response condition. The signal from the PMTs was amplified 10 times and then sent to an ADC, with a maximum resolution of 0.25 pC/channel. The signal triggering the sparkle was used to provide a gate for the ADC. In Fig. 2.6 we report a typical single photoelectron spectrum measured with a voltage supply of 2200 V. The first peak on the left is caused by pedestal events, followed by the single photoelectron peak, and a little bump caused by two photoelectrons.

We then raised light transmission by removing part of the filters, and measured the relative gain at different values of voltage supply. In Fig. 2.7 the calibration curve of one of the four PMTs is reported.

2.5.2 Beam test

The performances of the two prototypes were studied by exposing them to the H6 beam line at the CERN SPS. A first data-taking run was made in September 1997 with the ZP7 calorimeter, using a positron beam of 50, 100, and 150 GeV/c, and a hadron beam of 50, 100, 150, and 180 GeV/c.

During May 1998 the ZP2 prototype was tested with 75, 100, and 120 GeV/c positrons, and 50, 100, 120, 150, and 180 GeV/c hadrons.

The experimental set-up is shown in Fig. 2.8. A plastic scintillator hodoscope made it possible to select different triggers, accepting the beam particles inside a square of 1×1 cm^2 ($S_3 \cdot S_2 \cdot S_5$), 2×2 cm^2 ($S_3 \cdot S_1 \cdot S_4$), and 1×1 mm^2 ($S_3 \cdot D_{1V} \cdot D_{2H}$). The two small and movable scintillator-sticks D_{1V} and D_{2H} were used to localize the beam position on the calorimeter surface with an accuracy of 1 mm^2. The calorimeter is placed on a movable platform together with a MWPC installed just in front of it. Two plastic scintillation counters beyond an iron wall (MU_{1V} and MU_{2H}) detect muons.

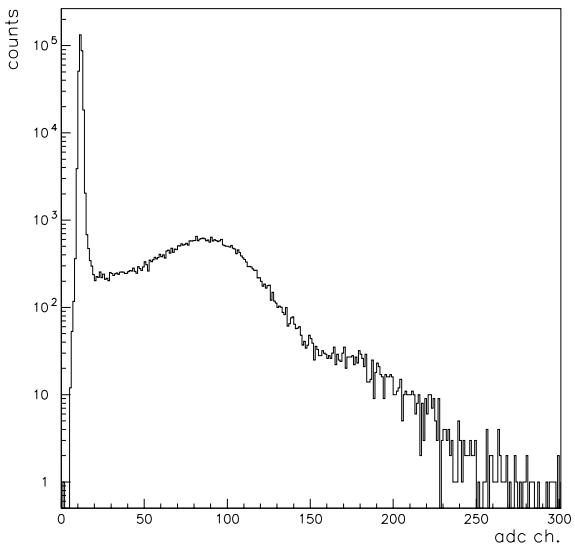

Figure 2.6: Single photoelectron spectrum from an XP2020 PMT at 2200 V.

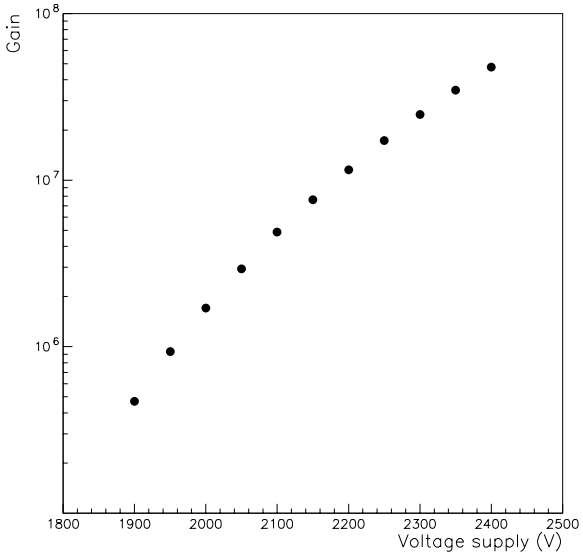

Figure 2.7: Gain of an XP2020 PMT as a function of voltage supply.

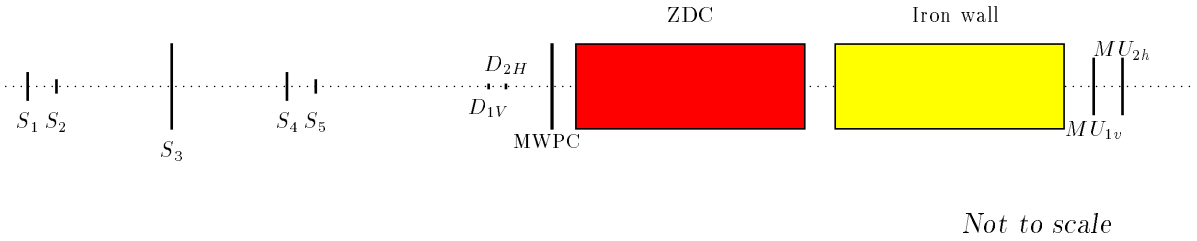

Figure 2.8: Schematic view of the experimental set-up used in the test. S_1, S_2, S_3, S_4, S_5: trigger scintillators. D_{1V}, D_{2H}: scintillator sticks. MU_{1v}, MU_{2h}: scintillators for muon detection.

The calorimeter signals were transported through C-50-11-1 coaxial cables to the counting room. The signals were split using a linear fan-out; one of the two lines was sent to a LeCroy2249 ADC, whilst the other was delayed out of the gate and then digitized. The use of the delayed channels is related to the pedestal subtraction technique, as explained below.

The PMTs were calibrated by sending a 100 GeV hadron beam to the centre of the calorimeter's front face.

During two weeks of data-taking runs with the two prototypes, it was possible to measure:

- the linearity of the detector's response as a function of the energy;
- the energy resolution for different fibre to absorber filling ratios and for different fibre spacings;
- the shower's transverse size;
- the uniformity of the response as a function of the beam impact point on the front face of the calorimeter.

These results were then compared with the predictions of Monte Carlo simulations.

2.5.3 Data analysis

2.5.3.1 Off-line calibration of the ADC channels

Pedestal subtraction

Some special runs without beam were dedicated to the measurement of the ADC pedestals connected to the ZDC PMTs. The method used for the pedestal subtraction makes use of the correlation between the ADC coming from the delayed and the timed PMT signals, measured in the pedestal runs, and shown in Fig. 2.9 for a typical run.

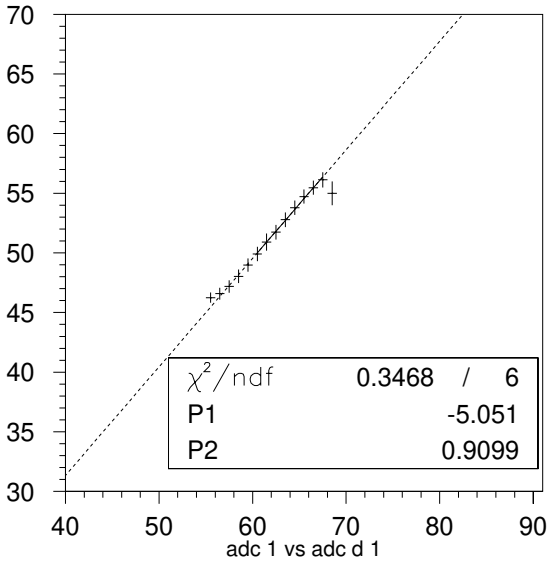

Figure 2.9: Correlation between the timed and the delayed signals and fit with a straight line for a PMT in a pedestal run.

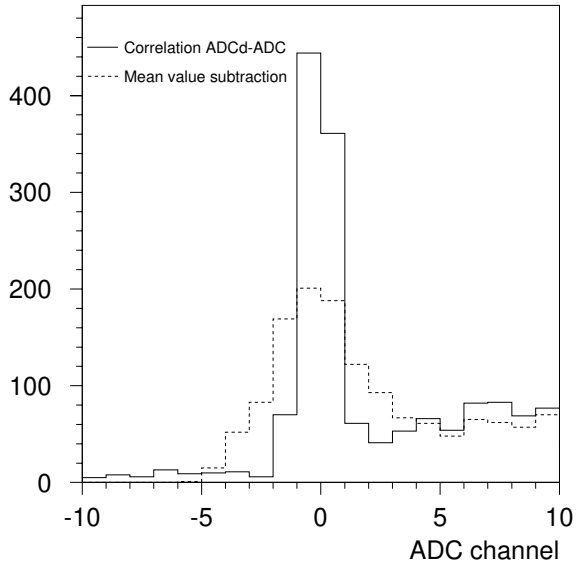

Figure 2.10: Pedestal peak for a standard data-taking run obtained with the correlation between the delayed and the timed signals (solid line) and by subtracting the mean value of the pedestal (dashed line).

In a standard data-taking run the pedestal in the timed ADC channel is calculated from the delayed one and subtracted from the signal event by event. Using this method we obtain a narrower pedestal peak with respect to the usual method based on the determination of the mean value of the peak (see Fig. 2.10).

Several pedestal runs were performed during the test to check the stability of the correlation.

Equalization of the channels

The fibres connected to each PMT are uniformly distributed in the passive matrix, so that each channel must detect the same amount of energy. A first equalization of the PMT high voltages was carried out at the beginning of the test, as described above. A fine tuning of the ADC signals for each channel was made offline to compensate possible small differences.

We fitted the ADC distributions and determined the peak positions; then we calculated the ratio between each peak value and the average, obtaining a correction factor for each channel. We extended this procedure to all the hadron runs with different energies and trigger conditions. For all the runs the beam spot was pointing to the centre of the calorimeter, to avoid edge effects. The choice of hadron runs is justified by the fact that the transverse shower size, in this case, is bigger than the distance between the

fibres, so that the response is independent of the beam coordinate (see Section 2.5.3.7). Then we adopted for each PMT the average correction factor over all the considered runs.

The dispersion of the correction factor for a PMT around the average value is of the order of 2–3%.

Conversion factor between the ADC channel and photoelectrons

To determine the position of the ADC peak corresponding to a single photoelectron signal, we considered muon events. Indeed, the energy loss of muons is very small, so that only a few photoelectrons are produced.

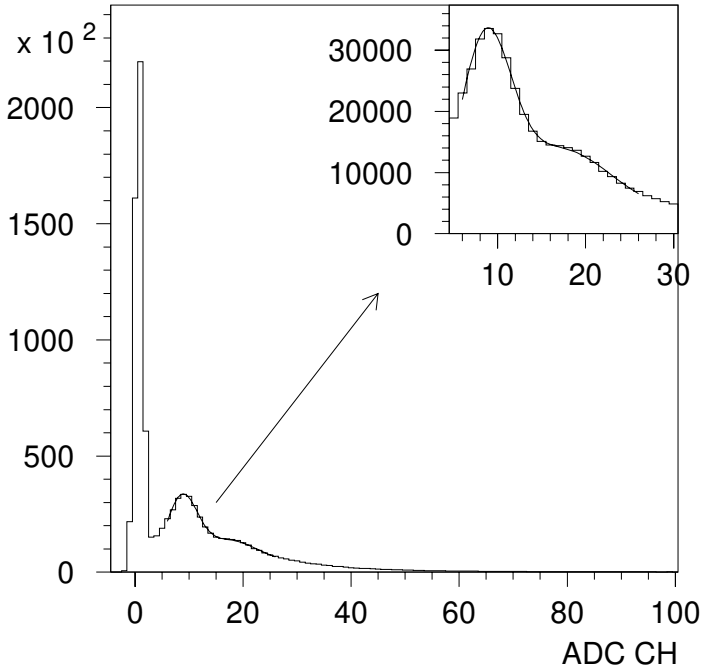

Figure 2.11: ADC spectrum with muon selection for a ZP2 PMT. The single photoelectron peak is clearly evident.

We selected the muons requiring a coincidence of the signals from the MU_{1V} and MU_{2H} scintillators. In Fig. 2.11 the ADC spectrum obtained by cumulating the statistics of all standard runs is shown for a PMT. We performed a fit to the ADC spectrum with the formula:

$$f(x) = P_1 e^{-\frac{(x-\mu)^2}{2\sigma^2}} + P_2 e^{-\frac{(x-2\mu)^2}{2(2\sigma^2)}} \quad . \tag{2.1}$$

The dependence of the results on the fit range and initial parameters was carefully studied. The fit with the lowest χ^2 was taken as the result. The error is due to the uncertainty on the fit procedure. As an example, we obtained a conversion factor for the ZP2 ADC1 of 7.4 ± 0.5 channels per photoelectron, in good agreement with the direct measurement mentioned above.

Using the linear correlation between the beam energy and ADC channels described below, we find a value of 0.81 photoelectrons per GeV, averaged over the four PMTs of the ZP2 prototype.

The single photoelectron measurement for the ZP7 prototype was only determined for one PMT, as for the other one the single photoelectron and pedestal peaks were not clearly resolved. The conversion factor for ZP7 is 6.8 ± 0.5 channels per photoelectron.

2.5.3.2 Data selection

The whole analysis is based on the ADC spectra, pedestal subtracted and equalized. The muon events, identified by means of the muon counters, were removed.

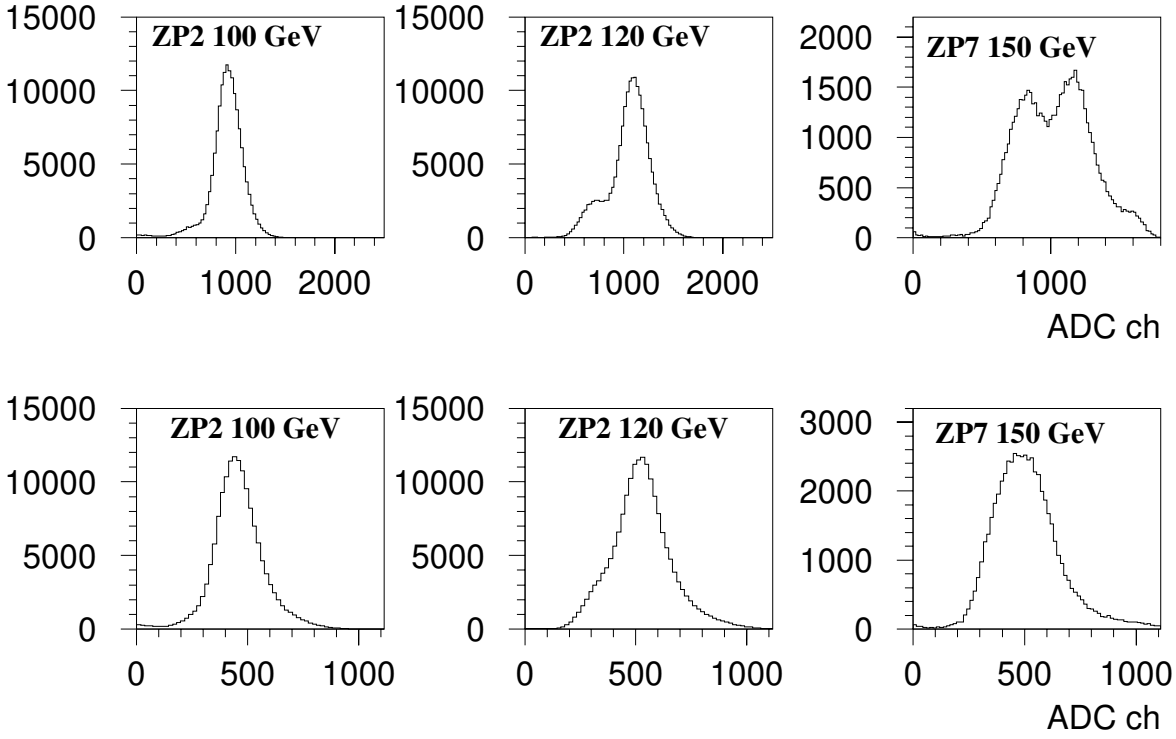

Figure 2.12: ADC spectra for positrons at different energies for a filling ratio of ∼1/80 (top) and ∼1/160 (bottom).

The positron beams at high energies suffered a hadronic contamination. It was possible to resolve the hadron and positron peaks only when the sum of all the PMT signals, corresponding to a filling ratio of $\sim$ 1/80, was considered (Fig. 2.12 top). For lower filling ratios the two peaks are not resolved (Fig. 2.12 bottom) and therefore, in this case, the measurement of the resolution at these energies is unsafe.

The hadron ADC spectra are not symmetric. To fit the spectra, we used the following function:

$$f(x) = Ae^{\frac{-(x-\mu)^2}{2\sigma(x)^2}}, \tag{2.2}$$

with:

$$\sigma(x) = \sigma_0 + \sigma_1 \frac{x-\mu}{\mu}. \tag{2.3}$$

Such a function has the advantage of being simple and giving stable results (very weakly depending on the initial parameters and the range of the fit), thus determining the peak value μ and the local width σ_0 at $x = \mu$ with uncertainties lower than 2%. The parameter σ_1 is related to the asymmetry of the distribution, and ranges from 30% σ_0 to 50% σ_0. All the ADC spectra are fitted with this function (or a combination of two such functions, in case of contamination) and the μ and σ_0 parameters are taken as the peak value and the width. Figure 2.13 shows the typical ADC spectra for hadrons and positrons.

For the linearity and resolution studies, we selected a set of runs collected with a 2×2 cm^2 trigger to avoid effects caused by the distance between the fibres, with a beam spot centred on the front face of the calorimeter.

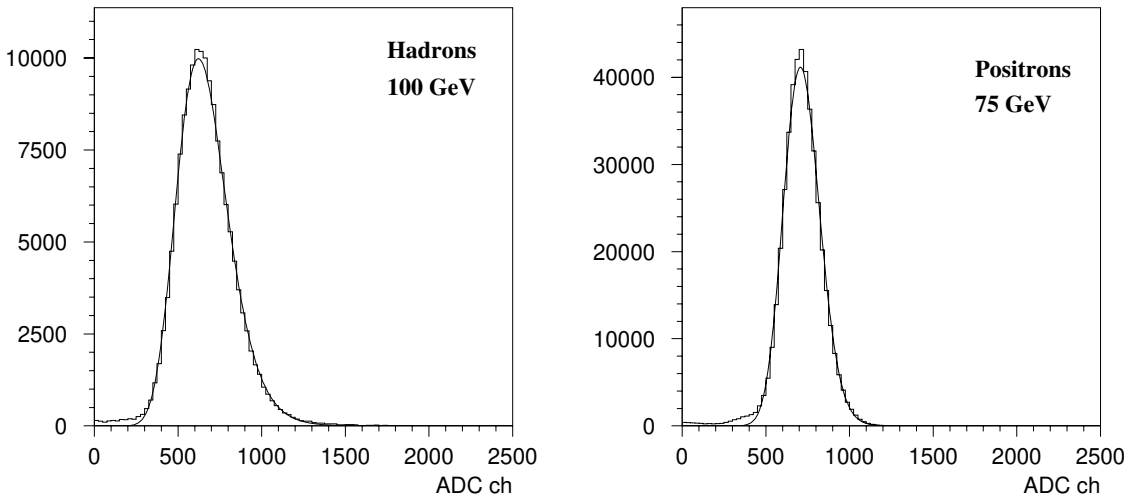

Figure 2.13: Fit to the ADC spectra for 100 GeV hadrons and 75 GeV positrons.

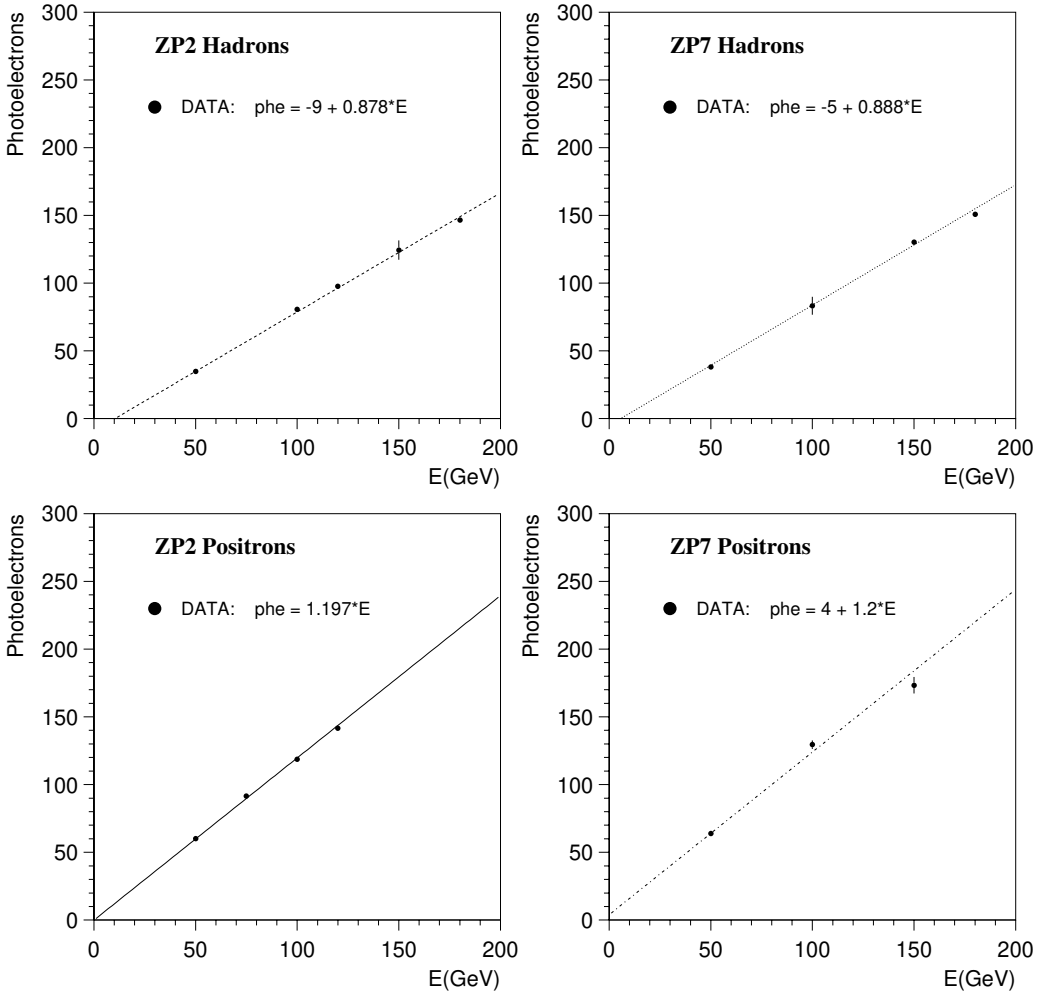

Figure 2.14: Top: response as a function of the hadron beam energy, E, for the ZP2 (left) and ZP7 (right) prototypes. Bottom: same for positron beams.

2.5.3.3 Stability checks

Several runs at each energy were collected during the test to check the stability of the measurements. The spread of μ and σ for different runs at each energy is below 2% for both parameters, with the exception of the 150 GeV runs, where the spread is around 5%.

We also checked the stability during every run. The effect caused by the variation of the response inside a run is $\sim 0.5\%$.

2.5.3.4 Linearity of the response with energy

We measured the response as a function of the energy for both prototypes with hadron and positron beams. The results, expressed in photoelectrons, are plotted in Fig. 2.14. The numerical values are reported in Tables 2.4 and 2.5.

Table 2.4: Resolution, peak value, and width as a function of the energy for the ZP2 calorimeter.

E (GeV)	μ (phe)	σ (phe)	Resolution (%)
ZP2 Hadrons - Data			
50	34.7 ± 0.2	11.1 ± 0.2	32.0 ± 0.7
100	80.7 ± 0.5	19.5 ± 0.4	24.2 ± 0.5
120	97.7 ± 1.4	22.2 ± 0.7	22.8 ± 0.8
150	124.4 ± 7.1	25.4 ± 2.0	20.4 ± 2.0
180	146.5 ± 0.9	27.6 ± 0.6	18.9 ± 0.4
ZP2 Positrons - Data			
50	60.2 ± 0.4	10.6 ± 0.3	17.6 ± 0.5
75	91.5 ± 0.5	14.0 ± 0.3	15.3 ± 0.4
100	118.7 ± 0.7	15.3 ± 0.4	12.9 ± 0.4
120	141.7 ± 0.8	17.1 ± 0.4	12.0 ± 0.3

Table 2.5: Resolution, peak value, and width as a function of the energy for the ZP7 calorimeter.

E (GeV)	μ (phe)	σ (phe)	Resolution (%)
ZP7 Hadrons - Data			
50	38.0 ± 0.7	14.1 ± 0.6	37.2 ± 1.7
100	83.3 ± 6.6	20.3 ± 1.4	24.3 ± 2.5
150	130.3 ± 0.8	26.1 ± 0.6	20.0 ± 0.5
180	150.7 ± 0.9	27.6 ± 0.7	18.3 ± 0.5
ZP7 Positrons - Data			
50	64.1 ± 0.5	12.0 ± 0.4	18.7 ± 0.6
100	129.5 ± 3.1	17.1 ± 0.6	13.2 ± 0.5
150	173.4 ± 6.1	18.1 ± 4.4	10.4 ± 2.6

The response as a function of the beam energy shows a good linearity. An energy threshold at a few GeV can be noted in the hadron data. A similar behaviour is reproduced by the simulation. It should be noted that the positron data suffer a strong hadron contamination at 150 GeV, causing a big uncertainty in the measurement, and therefore only two energies are reliable in the ZP7 positron data.

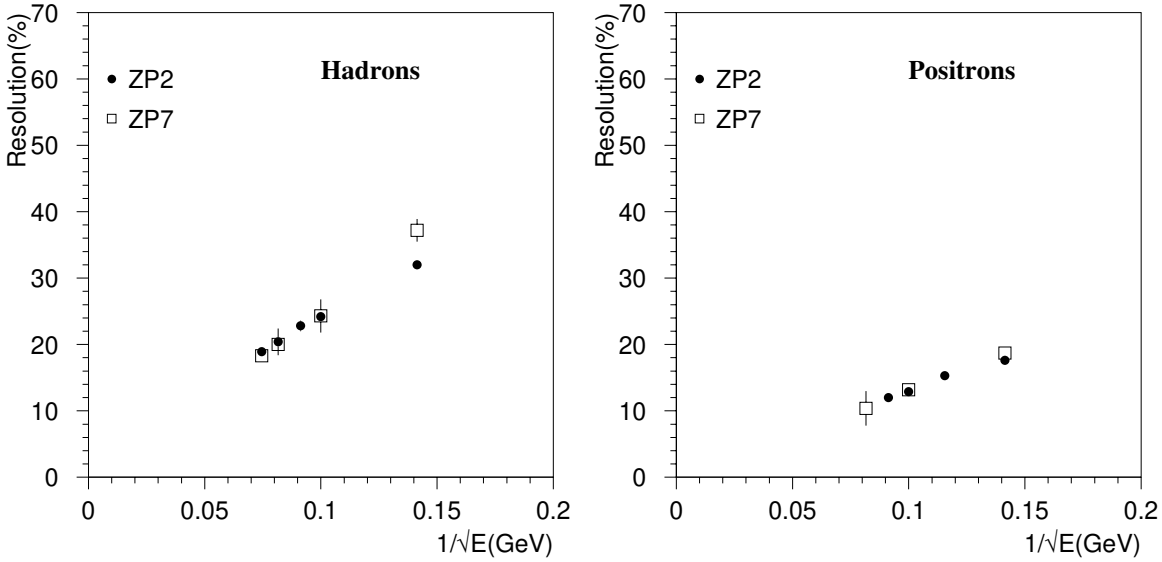

Figure 2.15: Resolution ($\frac{\sigma(E)}{E}$) as a function of $1/\sqrt{E}$ for the ZP2 (copper) and ZP7 (brass) prototypes in hadrons (left) and positrons (right).

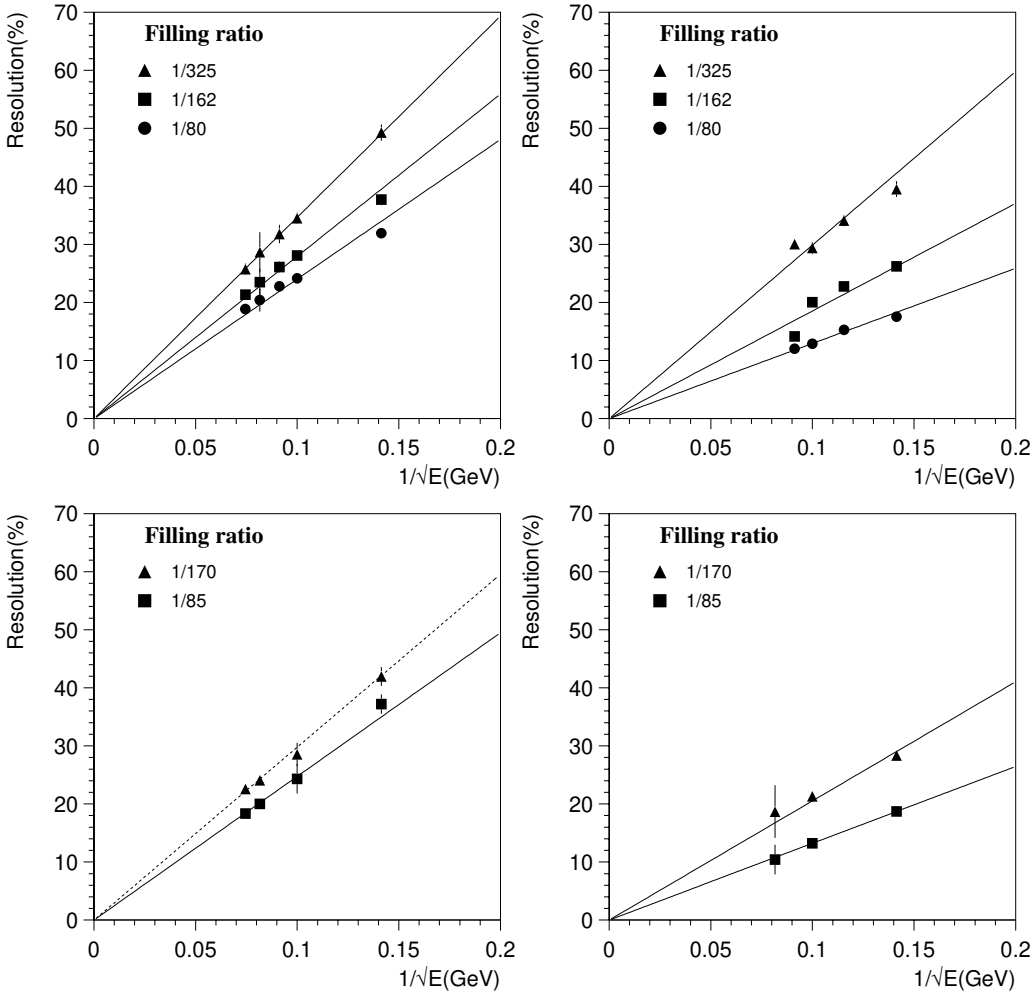

Figure 2.16: Top: resolution ($\frac{\sigma(E)}{E}$) as a function of $1/\sqrt{E}$ for the ZP2 prototype in hadrons (left) and positrons (right) considering different filling ratios. Bottom: same for ZP7.

2.5.3.5 Resolution as a function of the energy

The energy resolution for the two prototypes (Fig. 2.15) is comparable, as they have similar filling ratios. In Fig. 2.16 the resolution is plotted for different filling ratios, obtained selecting the signals from one, two, or four PMTs in ZP2, and one or two PMTs in ZP7. The experimental points are fitted with the function $a/\sqrt{E}$. The determination of a (small) constant term does not appear to be reliable at these energies. We can exclude, with a confidence level of 99%, a value of the constant term greater than 10%.

The simulation for hadrons underestimates the experimental resolution by $\approx 25\%$, as shown in Fig. 2.17, together with the same comparison with a positron beam, which indicates a better agreement.

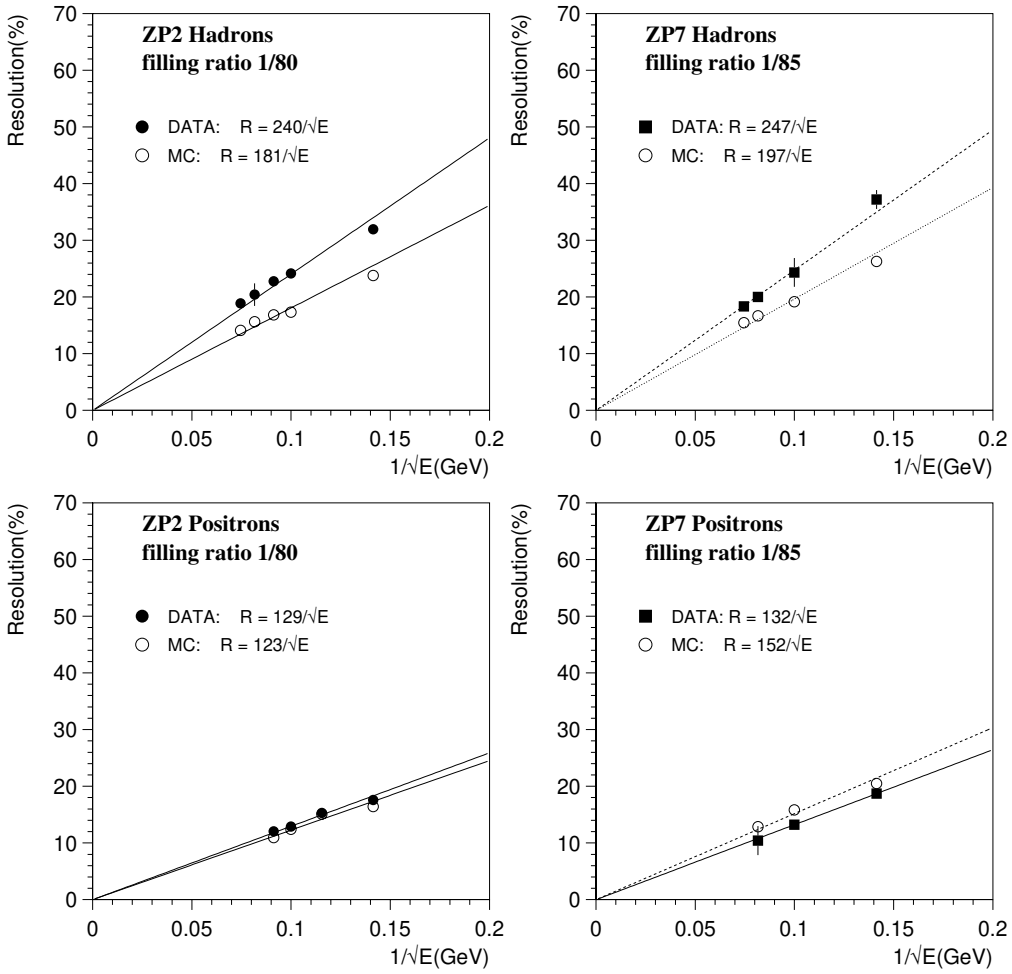

Figure 2.17: Top: resolution ($\frac{\sigma(E)}{E}$) for the ZP2 (left) and ZP7 (right) prototypes in hadrons compared with the Monte Carlo simulation. Bottom: same for positrons.

In order to have an estimate of the resolution at LHC energies, the simulations were performed with hadrons up to 2760 GeV, and the points were fitted with the function $a/\sqrt{E}+b$ (Fig. 2.18). The second term in this function is no longer negligible at very high energies because the fluctuations in the lateral energy loss are dominant with respect to the statistical fluctuations in the number of photoelectrons. The value of the resolution estimated for ALICE is $\sim 6\%$.

However, the use of plastic fibres is not possible at ALICE, where we are forced, because of the high radiation level, to choose quartz fibres with a lower numerical aperture. The simulation of a proton calorimeter with quartz fibres will be described in detail in Section 3.5 on page 53.

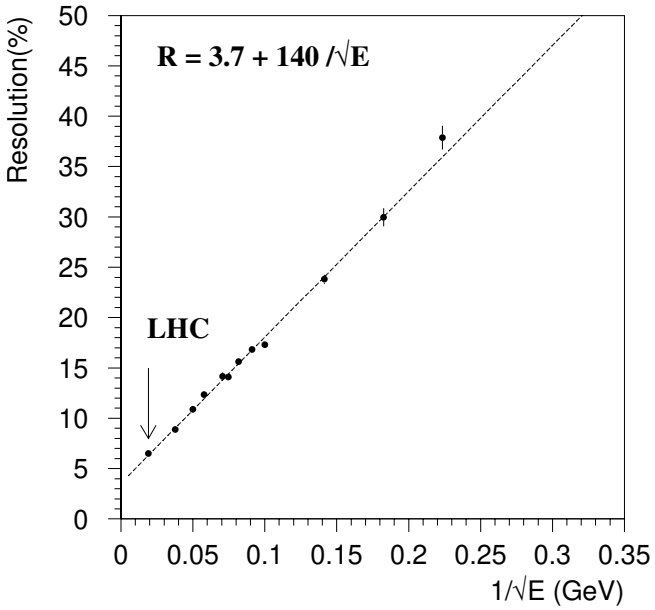

Figure 2.18: Monte Carlo simulation of the resolution for hadrons at several energies.

2.5.3.6 Shower's transverse size

In Fig. 2.19 we report the Monte Carlo simulation of the transverse size of the shower. In the abscissa we plot the position, with respect to the beam impact point, of the shower particle giving a non-zero light response; on the vertical axis the number of photoelectrons is reported.

The distributions are fitted with a superposition of two gaussians. The ratio between the parameters of these two gaussians was then fixed to fit the real data, as explained below.

To evaluate the hadronic and electromagnetic shower's transverse size from the data, we studied the response of the calorimeter as a function of the horizontal beam's impact coordinate. The information about the beam's position is given either by the MWPC or by the 1×1 mm^2 scintillators. As shown in Fig. 2.20 (top), there is a good agreement between the data and the Monte Carlo simulation. In the same figure (bottom) we show the derivative of the previous distributions from which one can estimate the transverse size of the shower. A fit to the hadron data appears unsafe due to the low number of points near the border. We thus fitted the derivative of the Monte Carlo distribution, obtaining a transverse size of 2.2 cm (FWHM). Applying the same procedure to the positron beam sample, we were also able to obtain a direct measurement from the data.

2.5.3.7 Uniformity of the response

It is important to verify whether the detector's response for hadrons is sensitive to the beam impact point with respect to the position of the fibres. We tested this feature on both prototypes, with a selection of the impact point using the MWPC. The four plots in Fig. 2.iii (in colour, see page 38) report, as a function of the beam impact point coordinates, the fraction of light (over the total signal) seen by two of the four PMTs in ZP2 (left plots), and one of the two in ZP7 (right). In this way, the two filling ratios considered (1/162 for ZP2 and 1/170 for ZP7) are comparable. The darker regions correspond to higher light fractions, and the black areas are found at the position of the fibres considered. Whilst a structure is clearly seen with the positron beam (down), it is less evident for hadrons in ZP7, and nearly disappears in ZP2. This behaviour can be explained by the fact that the shower induced by positrons is narrower, and that the fibre spacing in ZP7 (6 mm) is not small enough to provide a uniform response. The choice of a 4 mm fibre spacing, as in ZP2, seems to give a good uniformity.

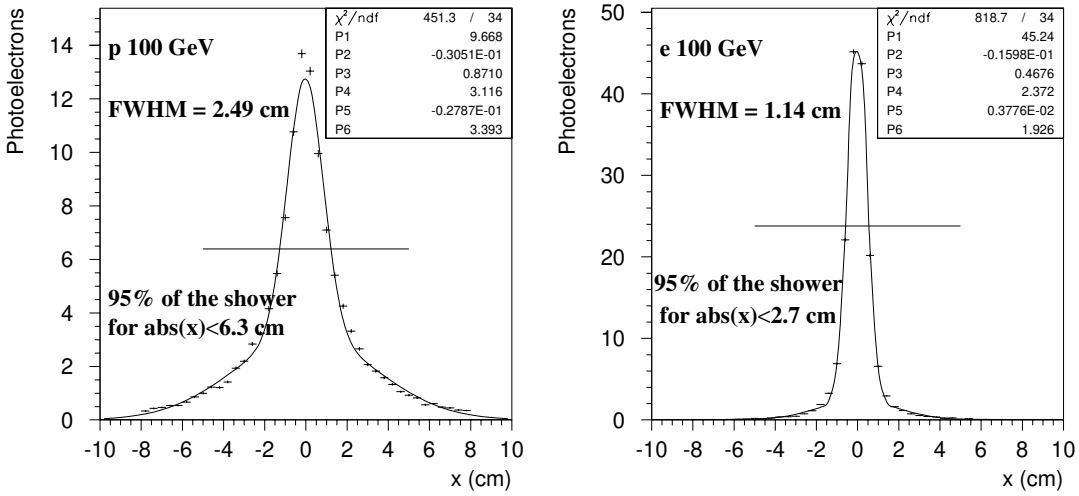

Figure 2.19: Simulation of the shower's transverse profile in hadrons (left) and positrons (right).

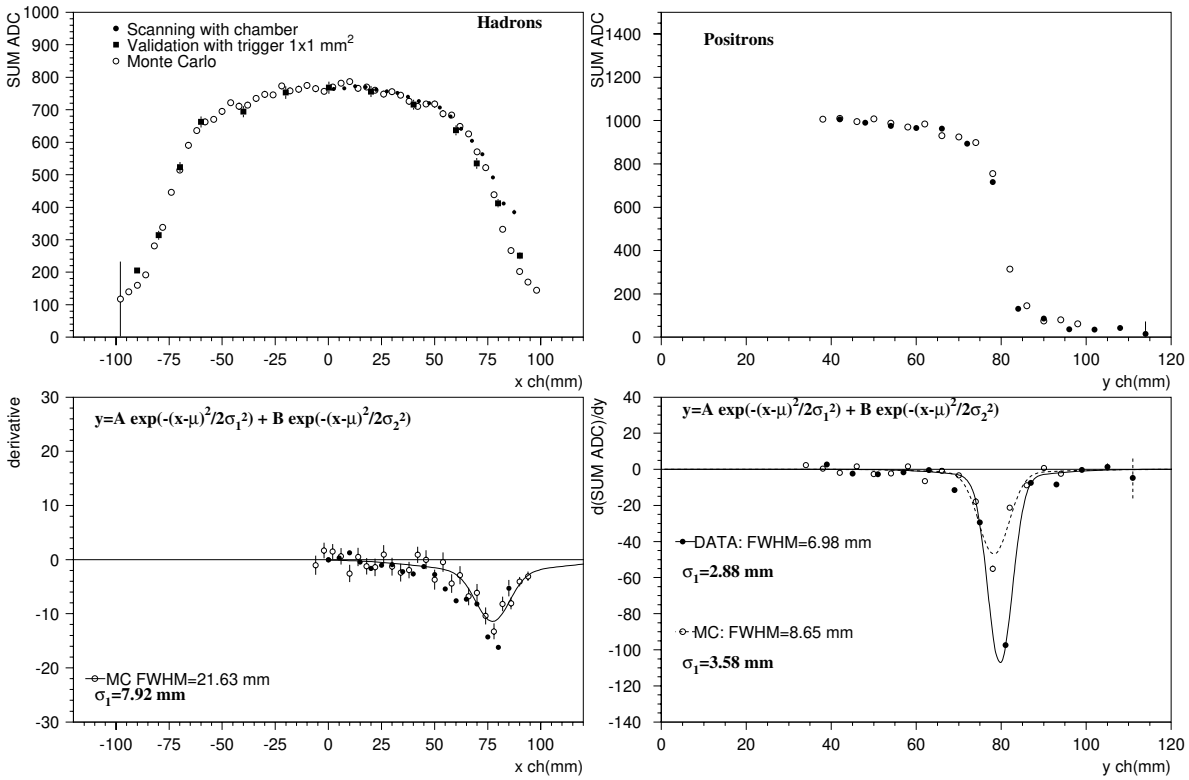

Figure 2.20: Top: calorimeter response as a function of the horizontal beam coordinate along the front face of the detector for hadrons (left) and positrons (right). Bottom: derivative of the above distributions and fits.

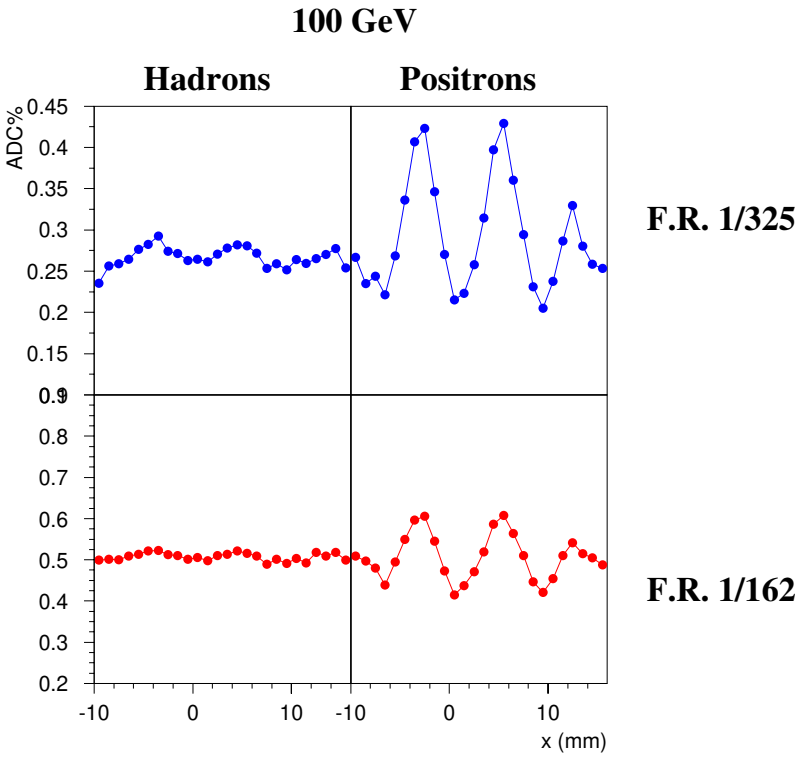

Figure 2.21: Variation of the light response plotted against x for different filling ratios and beams (see text for details).

Fixing a y coordinate corresponding to a fibre plane, in Fig. 2.21 we plotted the fraction of light seen by one (top) or two (bottom) PMT's over the total light collected by the four ZPZ PMTs, as a function of x. On the left side the response for a 100 GeV hadron beam is plotted, whilst on the right the positron results are shown. The response for hadrons with a filling ratio of 1/162 can already be considered uniform.

2.6 The ZDC in the NA50 experiment

The ZDC now in use in the NA50 experiment can be considered equivalent to an ALICE neutron calorimeter prototype. In fact, both detectors have to fulfil similar requirements, such as radiation hardness and geometrical constraints. It should also be noted that the operational conditions in NA50 are more severe than those that a ZDC will encounter in the ALICE experiment.

The NA50 ZDC operated successfully in the 1995, 1996, and 1998 data-taking periods. As it is well known, the J/Ψ measurement requires lead-ion beams of intensity greater than 10^7 lead ions per second. Therefore, the NA50 ZDC must satisfy very strong requirements, summarized hereafter:

- high radiation hardness (in the Grad region)
- low sensitivity to nuclear activation
- short duration of the signal ($\leq$ 10 ns)
- energy resolution of the order of a few per cent

- spatial resolution of some hundred μm for lead ions

To satisfy all these requirements a quartz fibre spaghetti calorimeter with fibres parallel to the beam axis, has been built and operated by the Torino University group [12].

2.6.1 Description of the detector

The structure of the detector is shown in Fig. 2.22.

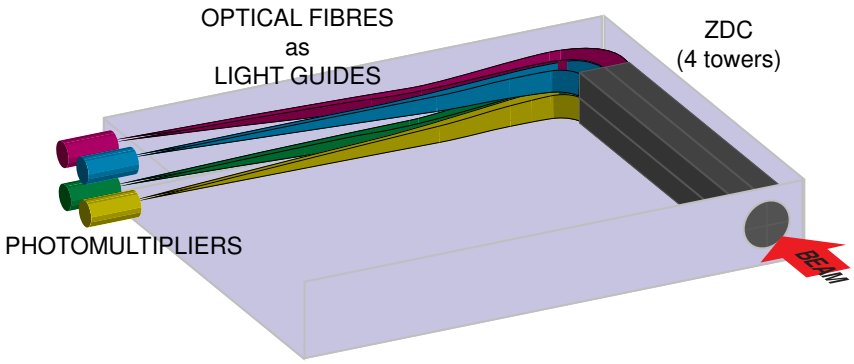

Figure 2.22: Mechanical structure of the ZDC.

It consists of 30 grooved tantalum slabs (each of them 1.5 mm thick), stacked to form a parallelepiped of $5 \times 5 \times 65$ cm^3. The active part of the detector is made of 900 quartz fibres, uniformly distributed with a pitch of 1.5 mm corresponding to a quartz to tantalum volume ratio of 1/17. The fibres are of HCG-M-365-U type (manufactured by SpecTran Specialty Optics Company, USA) and have a pure silica core, silica fluorinated cladding, and a hard polymer coat, with diameters of 365, 400, and 430 μm, respectively; the numerical aperture is 0.22. The total length of each fibre is 180 cm. The first 65 cm embedded in tantalum represent the active part of the calorimeter. The rest (bent at 90° with respect to the ZDC axis) act as a light guide towards the photomultipliers located about 1 m from the beam axis to reduce background caused by shower particles impinging on the PMT window. To be position sensitive the ZDC is divided into four towers grouping the fibres into four bundles of 225 fibres, each bundle seen by one photomultiplier. Consequently the impact point of a lead ion is determined using the centroid of the four signals. 60% of the hadronic shower generated by a proton of 158 GeV entering the centre is contained in the detector. The resolution is dominated by the fluctuations in the part of the hadronic shower contained in the detector. A light yield of about 0.5 photoelectrons per GeV is observed for a PMT with a bialcaline photocathode and a borosilicate window, so that no problem comes from statistical fluctuations on their number. The light yield together with the high intensity of the beam impose the choice of PMTs with low gain (to avoid instabilities due to the increase of the average anode current). For this reason, we used 6-stage Philips XP 2242-B photomultipliers operating at a gain of about 5×10^3; with these conditions a mean current value of 30 μA is obtained for 5×10^7 Pb per burst. To achieve a stable behaviour, particular care has been taken in the design of the voltage divider, made with transistors [13]. The signals were sent to the counting room through very long cables (about 200 m). To preserve the excellent time quality of the Cherenkov signals, bridge-T filters were used before the last stage of amplification. The signal width allows a gate of 12 ns to be used, necessary to cope with the high-intensity beam required by the experiment.

In the NA50 experiment the ZDC detector was located after a 60 cm copper collimator and covered the pseudorapidity region $\eta \geq 6.3$.

2.6.2 Performance of the detector

The response of the detector to a Pb ion beam of 158 A GeV/*c*, at the beginning of the run, is presented in Fig. 2.23.

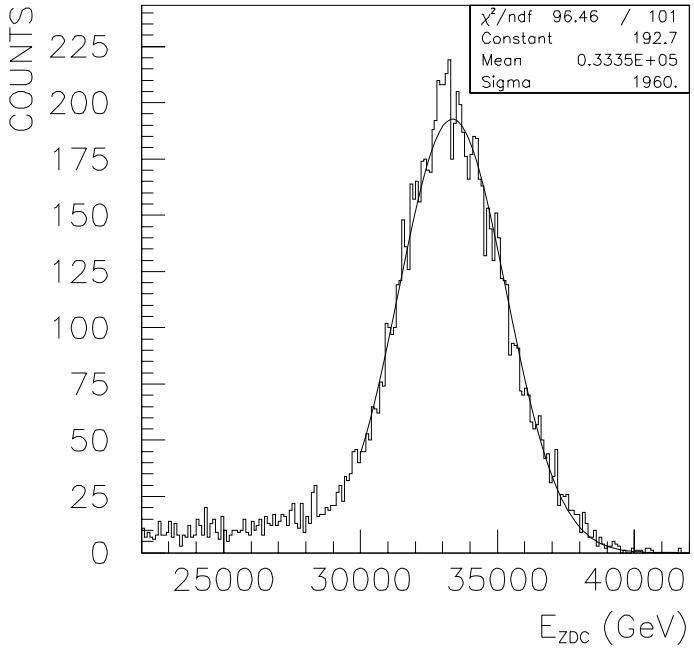

Figure 2.23: Response of the ZDC with the beam hitting the centre of the front face.

The resolution obtained was 6%, with a gate width of 12 ns. During data-taking, the ZDC was continuously monitored by checking the position of the 'lead peak'. The stability of the response of the photomultipliers was monitored by means of a laser diode pulse light optically connected to each photomultiplier through a quartz fibre.

Tests with electron and proton beams, showed that the ZDC is not compensated giving an e/π ratio of 2.4. This implies that the response of the ZDC to hadrons is not linear as a function of their energy.

However, this fact does not create any problems for using the detector in NA50, where the goal is to measure the number of residual nucleons after the interaction of a Pb nucleus with the target nuclei. In this case, spectator nucleons and nuclear fragments detected by the ZDC have the same fixed energy per nucleon as the beam.

To obtain the spectator number it is important to check whether the response of the calorimeter is linear as a function of the number of nucleons entering the detector. To prove this linearity secondary beams of light nuclei (deuterons and alphas) were generated by fragmentation of the SPS Pb beam on a 4 mm lead target.

Unfortunately, with these techniques it is not possible to obtain intermediate mass nuclei. To overcome this problem partially we used an Fe target and we determined the low-energy end point of the ZDC spectrum, corresponding to the most central collisions.

In this case, for central collisions the number of projectile spectator nucleons is given by:

$$(N_A)_{\mathrm{spec}} = 208 \times \left(\left(\frac{208}{A} \right)^{\frac{2}{3}} - 1 \right)^{\frac{3}{2}} .$$

In Fig. 2.24 the response of the ZDC to various nuclei is reported. The ratio ADC(A)/A, normalized to the Pb point, is plotted versus A.

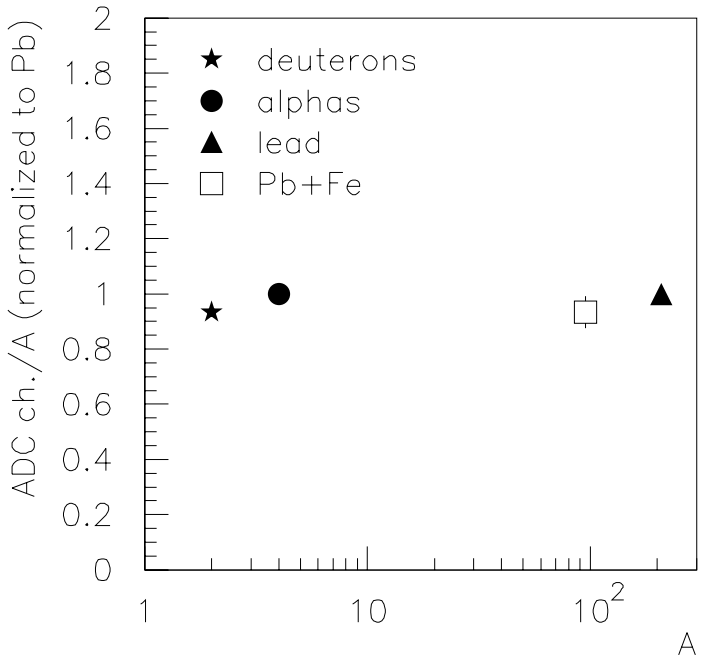

Figure 2.24: Response of the ZDC to nuclear beams of 158 A GeV/c. The filled symbols give the value of the ADC channel corresponding to the peak observed for each projectile, divided by its mass number A. The open symbol refers to the end point of the energy spectrum measured in Pb–Fe collisions.

It can be observed that over the range A = 2–208 these ratios remain constant, indicating a linear behaviour of the detector.

Finally, the energy resolution for protons, deuterons, alphas and lead nuclei has been measured. The data, plotted in Fig. 2.25, show a linear behaviour in the $\sigma(E)/E$ versus $1/\sqrt{A}$ plot, fitted according to:

$$\frac{\sigma(E)}{E} = \frac{a_1}{\sqrt{A}} + a_2 \,,$$

with a_1 = 26.8% and a_2 = 6.2%. In the same figure, we show the points obtained with lead and proton beams using a gate width of 20 ns and a lower beam intensity (filled symbols), and data obtained with a narrower gate (12 ns) with standard NA50 run conditions (open symbols).

2.6.3 Zero degree energy measurement

In Fig. 2.26(a) the ZDC energy spectrum obtained with a minimum bias trigger at a beam intensity of 10^7 Pb/s is shown. A peak corresponding to 33 TeV lead ions entering the ZDC without interacting in the target is clearly seen in the figure. The events on the left of the Pb peak are caused by lead-ions interacting in the target. To reject the non-interacting lead, the information from the NA50 electromagnetic calorimeter can be used. The minimum bias differential cross-section distribution obtained requiring a non-zero transverse energy in the electromagnetic calorimeter is shown in Fig. 2.26(b), together with the VENUS predictions. The experimental and simulated distributions prove to be in good agreement.

In particular, the low-energy parts of the spectra are similar: both show a 'knee' at $E_{\rm ZDC}$ about 6 TeV and a few events at $E_{\rm ZDC}$ smaller than 2–3 TeV. This means that even in the most central collisions a residual energy of 2–3 TeV is emitted at 0°.

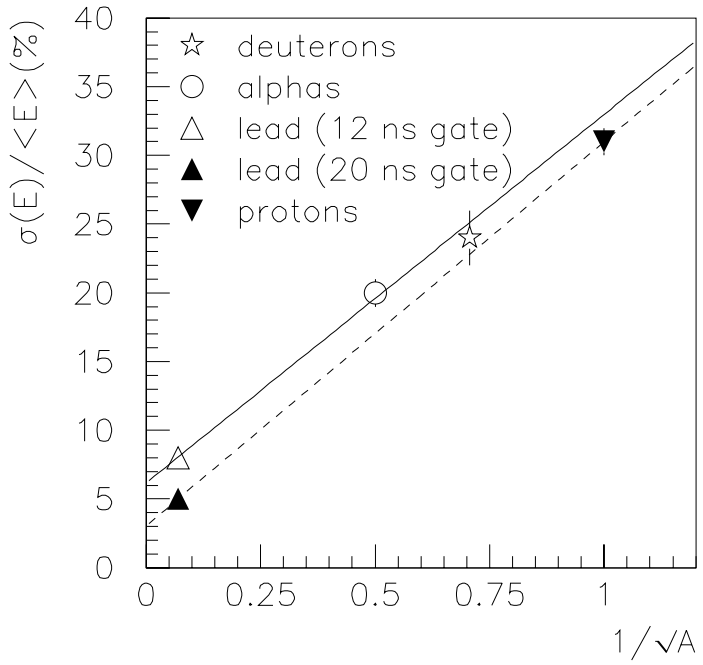

Figure 2.25: Energy resolution $\sigma(E)/E$ for 158 A GeV/c incident nuclei of different mass number A, plotted versus $1/\sqrt{A}$. Open and filled symbols refer to data obtained with gate widths of 12 and 20 ns, respectively.

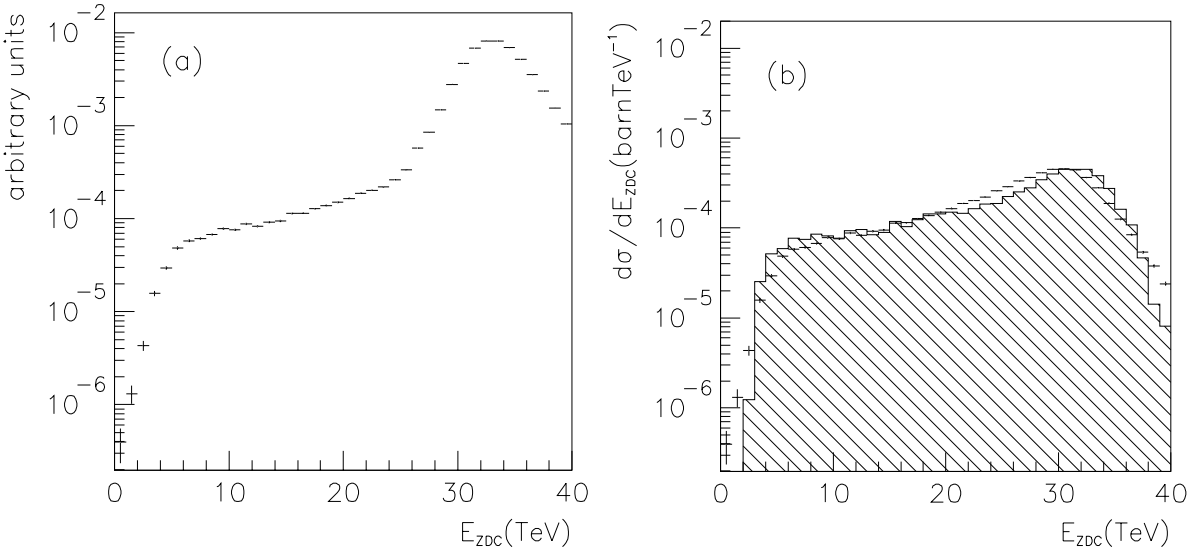

Figure 2.26: (a) Zero-degree energy spectrum obtained with the unbiased trigger; (b) experimental and simulated (hatched histogram) minimum bias differential cross-section.

A further confirmation of the reliability of the detector can be obtained by looking at the correlation between the 0° energy and the neutral transverse energy, measured in the pseudorapdity range $1.1 < \eta < 2.3$ using an electromagnetic calorimeter. Both detectors measure a signal which is expected to be strongly correlated with the centrality of the collision; this is indeed what we see in Fig. 2.27.

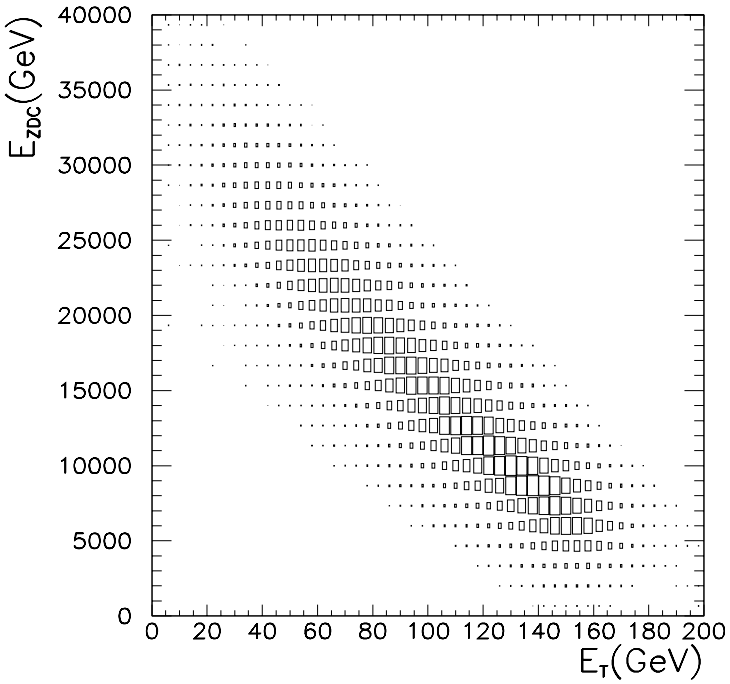

Figure 2.27: Zero-degree energy (E_{ZDC}) vs. transverse energy (E_T) measured by the electromagnetic calorimeter.

2.6.4 Radiation hardness

In Fig. 2.28 the position of the Pb peak is shown as a function of the dose D_{max} absorbed by the detector throughout the NA50 1996 and 1998 data-taking periods; clearly the signals lower with the dose, but they have been recovered increasing the gain of the PMTs.

The dose D_{max} has been evaluated by means of a Monte Carlo simulation based on the GEANT code. It represents the dose deposited in the four fibres closest to the axis of the ZDC, at a depth corresponding to the maximum development of the shower (i.e. between 1 and 2 λ_{I}).

In Fig. 2.29 we can see how the resolution deteriorates as a function of the dose received during the same data-taking period. After an initial worsening from 6% to 8%, the resolution stayed almost stable.

As a last consideration it should be noted that after the 1996 run the detector presented an activity (at the contact) of 20 mSv/h that was reduced to 5 mSv/h before the beginning of the 1998 run. The high activity excludes close contact and long manipulation of the detector. However, it has to be stressed that there was no need of maintenance, except for the replacement of the PMTs after one year of operation.

On the contrary, the calorimeter is almost insensitive to induced radioactivation, due to the fact that the activation products lie mainly below the Cherenkov β threshold.

2.7 Electromagnetic calorimeter prototype

Systematic studies of electromagnetic calorimetry, which sample the Cherenkov radiation of shower particles in optical fibres, were exploited within the RD40 collaboration. The results are resumed in Refs. [7, 14].

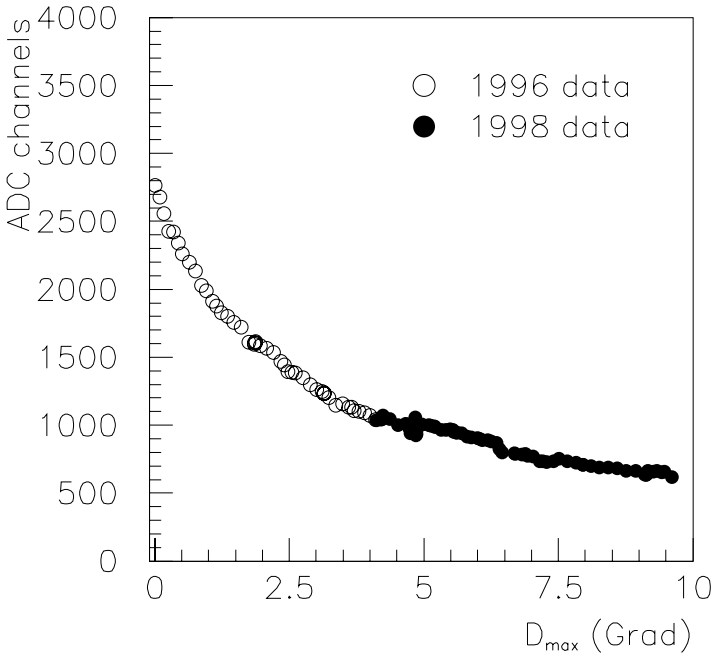

Figure 2.28: Position of the lead peak in the ZDC spectrum as a function of the dose $D_{\max}$ absorbed by the detector throughout the 1996 and 1998 NA50 data-taking periods.

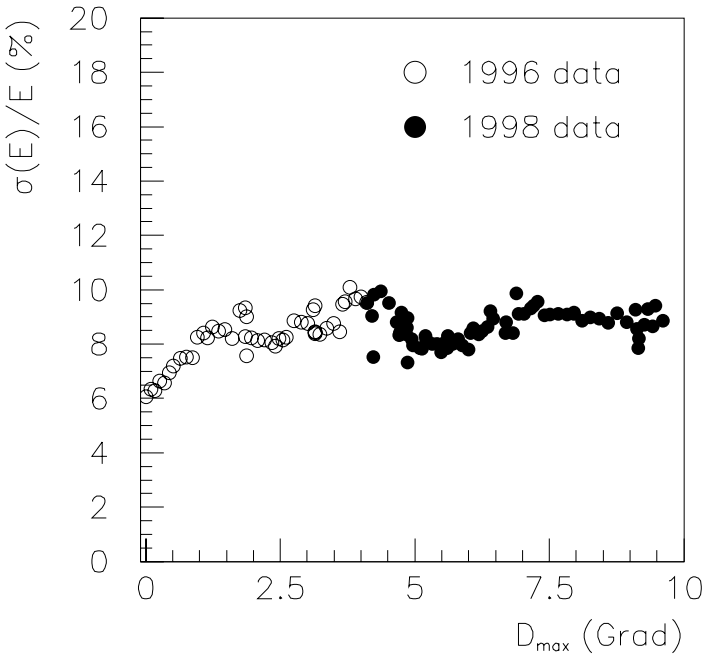

Figure 2.29: Resolution $\sigma(E)/E$ on the ZDC peak measurement as a function of the dose absorbed by the detector throughout the 1996 and 1998 NA50 data-taking periods.

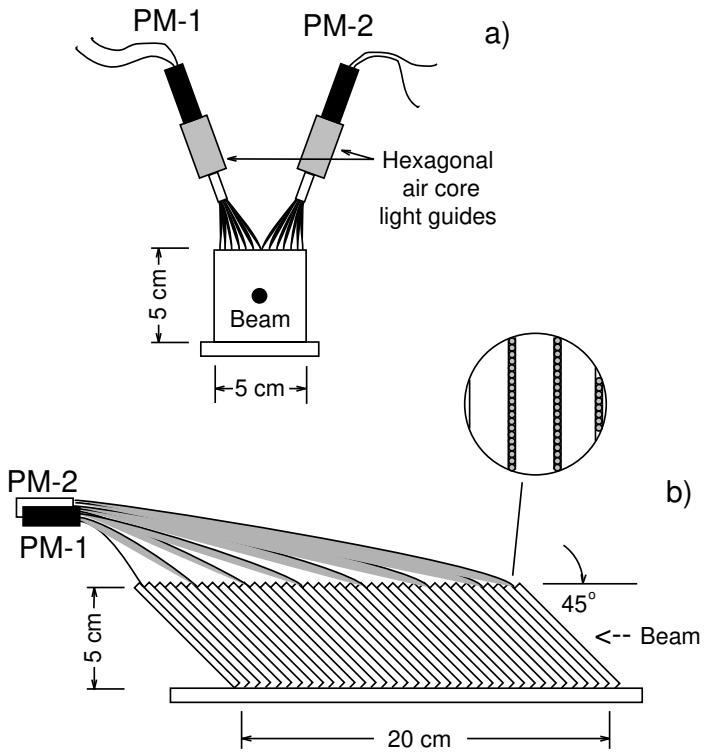

Figure 2.30: Schematic front (a) and side (b) views of the Proto-3 electromagnetic prototype.

Beam tests were performed using 5 to 100 GeV electrons at the CERN SPS. The performances of an electromagnetic prototype, Proto–3, tested in 1993, are briefly summarized here. A schematic view of the e.m. prototype is shown in Fig. 2.30; its outer dimensions were $5 \times 5 \times 20$ cm^3. The prototype was constructed with fibres arranged in ribbons and sandwiched between plates of absorber material, with no transverse separation between fibres. The fibres were tilted at 45° with respect to the incident particle direction, in order to maximize the detector response in terms of collected Cherenkov photons. The fibres (produced by CeramOptec GmbH, Bonn, Germany) were 500 μm in diameter, with a numerical aperture NA = 0.37 and they consisted of a quartz core with PMMA cladding. The fibre planes were separated by 3 mm flat lead absorber sheets which, after the 45° tilt, results in the incoming particles crossing a longitudinal absorber thickness of 4.24 mm. This distance is shorter than 1 radiation length for lead (5.6 mm) ensuring frequent longitudinal sampling of electromagnetic showers. The fibre-to-lead volume ratio was about 1:8. The calorimeter was divided laterally into two independent readout channels. Each tower fully contained the shower electrons impinging at its centre. Readout was carried out using Philips XP2020/Q PMTs with an air core. Hexagonal light guides were used to homogenize the response of the different parts of the photocathode to different fibres.

Figure 2.31 shows the linearity of the response of the detector to electrons with energy between 5 and 100 GeV. The resolution, measured using single channels, is shown in Fig. 2.32. A fit to the data points gives:

$$\frac{\sigma}{E} = \frac{(35.8 \pm 1.8)\%}{\sqrt{E}} \oplus (0.40 \pm 0.80)\ ,\%$$

for the right PMT and

$$\frac{\sigma}{E} = \frac{(37.9 \pm 2.1)\%}{\sqrt{E}} \oplus (0.01 \pm 0.90)\ ,\%$$

for the left PMT.

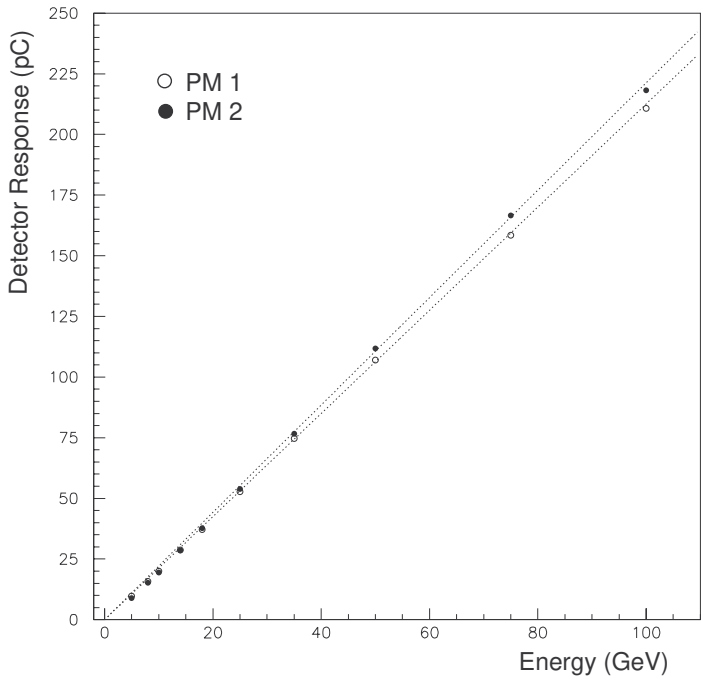

Figure 2.31: Response of the e.m. calorimeter prototype, Proto-3, to electrons of energy from 5 to 100 GeV.

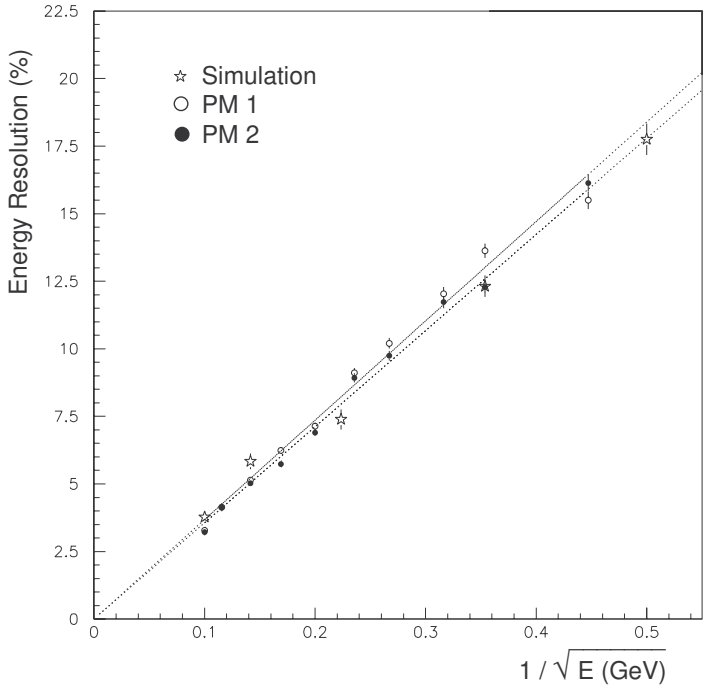

Figure 2.32: Measured electromagnetic energy resolution of Proto-3 as a function of $1/\sqrt{E}$, together with the results from the Monte Carlo simulation.

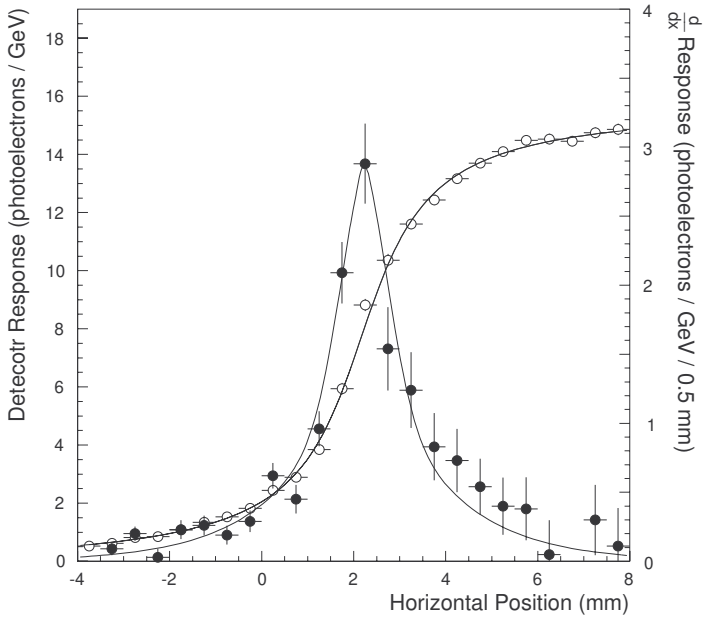

Figure 2.33: Edge scan (open circles and left vertical axis) of Proto-3, measured using a 8 GeV electron beam. The edge position is at x = 2.2 mm. The solid line is an arctangent fit to the data. Also shown is the electromagnetic lateral shower profile for Proto-3 (filled circles and right vertical axis). The solid line is the result of a fit to the sum of two gaussians as described in the text.

A precise measurement of the Cherenkov electromagnetic shower size has also been carried out, performing a scan between the right and left halves of the prototype. Figure 2.33 (open circles and left axis) shows the results for a transverse scan of the prototype with 8 GeV electrons. The response of one PMT is shown and the solid line is the result of a fit to the data with an arctangent function. The same figure shows the electromagnetic lateral shower profile (filled circles and right vertical scale) as the derivative of the data. The electromagnetic lateral shower profile can be fitted as a sum of two gaussian functions, with σ = 0.86 mm and 3.4 mm, with the two contributions having approximately the same integral. Both terms describe a visible shower size which is far below a Molière radius (16 mm for lead).

Beam tests using electrons of energy from 5 to 100 GeV have also been performed on two other similarly constructed prototypes, Proto-4 and Proto-R, in which different types of fibre were used, mainly to measure the influence of the numerical aperture on the calorimeter response. The quartz fibres had a hard polymer cladding (NA = 0.37) in Proto-3, a silicone cladding (NA = 0.40) in Proto-4, and a fluorinated quartz cladding (NA = 0.22) in Proto-R. An e.m. energy resolution of

$$\frac{\sigma}{E} = \frac{(41.7 \pm 0.3)\%}{\sqrt{E}} \oplus (0.7 \pm 0.6)\ ,\%$$

and

$$\frac{\sigma}{E} = \frac{(42.3 \pm 0.7)\%}{\sqrt{E}} \oplus (0.0 \pm 1.1)\ ,\%$$

have been obtained using the sum of both readout channels for Proto-4 and Proto-R, respectively. These results are to be compared with those obtained with Proto-3:

$$\frac{\sigma}{E} = \frac{(35.6 \pm 0.2)\%}{\sqrt{E}} \oplus (0.0 \pm 0.4)\% \ .$$

3 Description of the detector

3.1 Introduction

This Chapter consists of two parts. The first part concerns the tight link between the parameters of the beam line and the acceptance of the ZDCs. The second part is dedicated to a detailed description of the proposed calorimeters.

3.2 ZDC geometry

To detect the spectator neutrons the ZDCs should be located along the LHC beam axis at a point where the distance between the beam pipes has its maximum value, i.e. before the separation magnet D2. The beam elements and the detector geometry are sketched in Fig. 3.1.

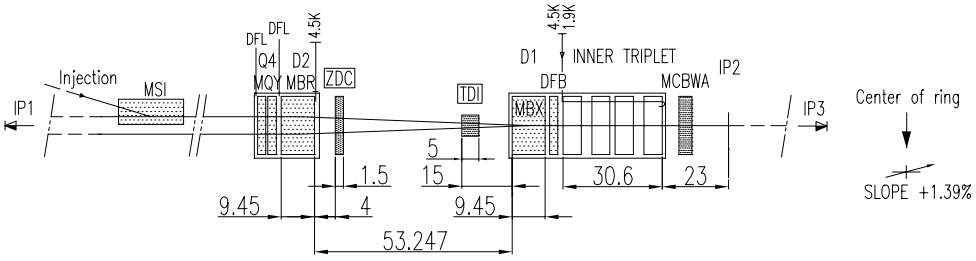

Figure 3.1: Line sketch from IP2 to D2 magnet.

Starting from the intersection point (IP), the first magnetic element, on both sides of the IP, is a small dipole (MCBWA) which compensates the field of the dipole of the ALICE muon arm. It is followed, at 23 m from the IP, by a low-β (or inner) quadrupole triplet. A 9.45 m long superconducting dipole (D1), starting at 58.43 m, separates the two beams. The position and fields of the magnetic elements of the beam line are listed in Table 3.1.

Table 3.1: Parameters of the beam line magnetic elements.

Element	z position (m)	Magnetic length (m)	Nominal field (T) at x (m)
Muon dipole	7.5	4.3	0.75
Dipole corrector	19.2	1.9	-1.1716
First quadrupole	23.0	6.3	$-200.34 \cdot x$
Second quadrupole	31.8	5.5	$200.34 \cdot x$
Third quadrupole	38.3	5.5	$200.34 \cdot x$
Fourth quadrupole	47.3	6.3	$-200.34 \cdot x$
D1	58.4	9.45	3.529

Following D1, a beam pipe, made of conical and straight sections, will contain the beams as well as the spectator nucleons. The diameter of this pipe starts at 7.3 cm and increases along its length to a final diameter of 60 cm, as shown in Fig. 3.2. The beam envelopes shown in the figure take into account the

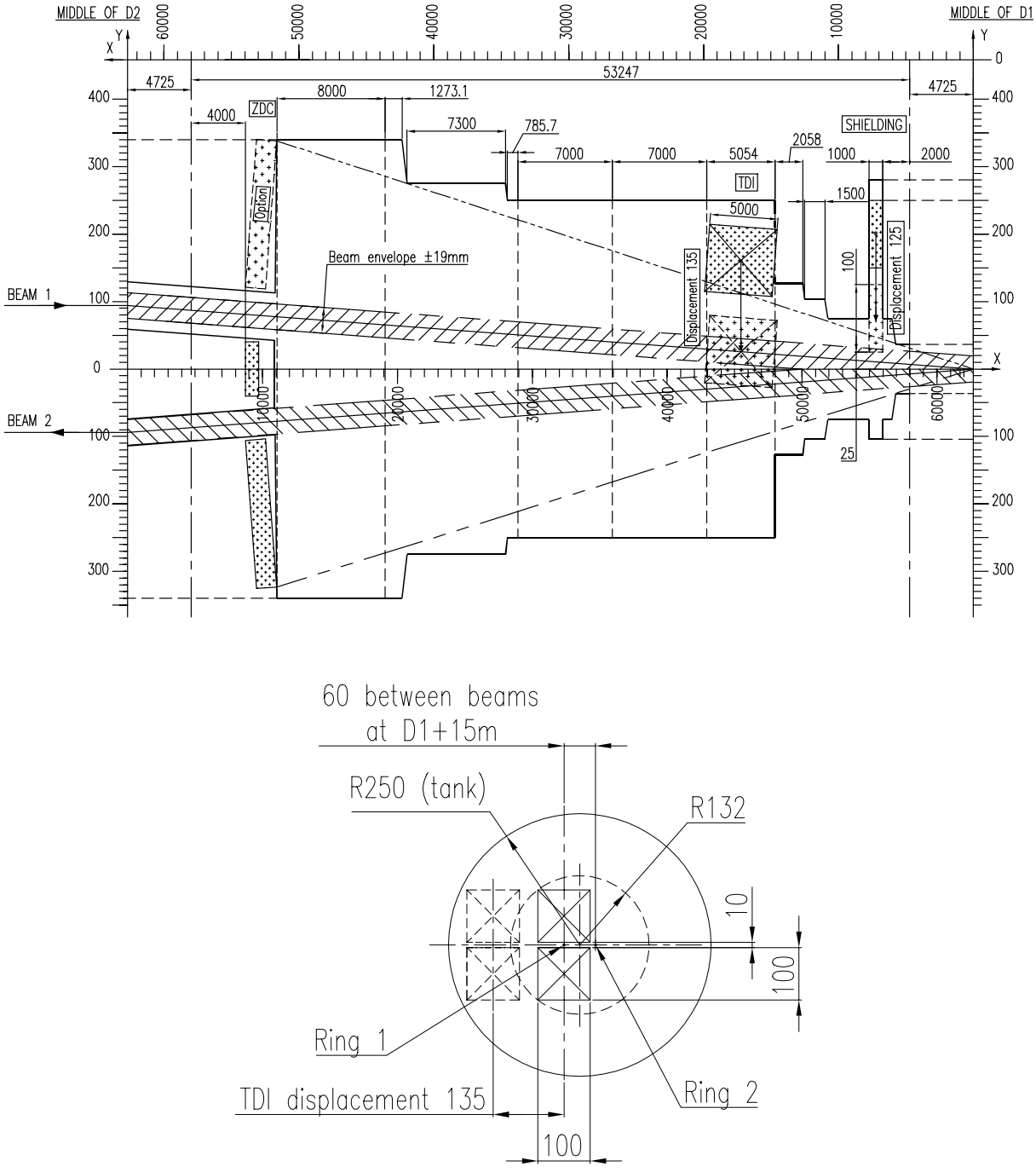

Figure 3.2: Design of the conical pipe from D1 to D2. Longitudinal (top) and transversal (bottom) views.

10 σ beam aperture required to avoid important beam losses (∼ 8.5 mm). Closed orbit errors and the mechanical tolerances of 2 mm over the 40 m of the conical pipe are also taken into account.

We have, at the downstream end of the conical pipe, a distance of 154 mm between the two circulating beams and outer diameters of 44 mm/74 mm for the outgoing/incoming beam pipes. The diameter of the pipe corresponding to the incoming beam needs to be larger in order to accommodate mis-injected bunches that will be dumped in the TDI absorber.

The available transverse space close to D2 is ≃ 10 cm; between the end of the conical pipe and the beginning of D2 a longitudinal space of about 2.5 m is left free for the insertion of the neutron calorimeter. The proton calorimeter can be placed at the same distance from the IP, externally to the outgoing beam pipe, as required by the magnetic rigidity which is smaller than the beam one. A third calorimeter, for measuring the negative particles produced in a momentum range close to the one of the spectator protons, was proposed in the TP and is still shown in the figure. However, its importance is still being investigated, as will be explained in Section 3.3.

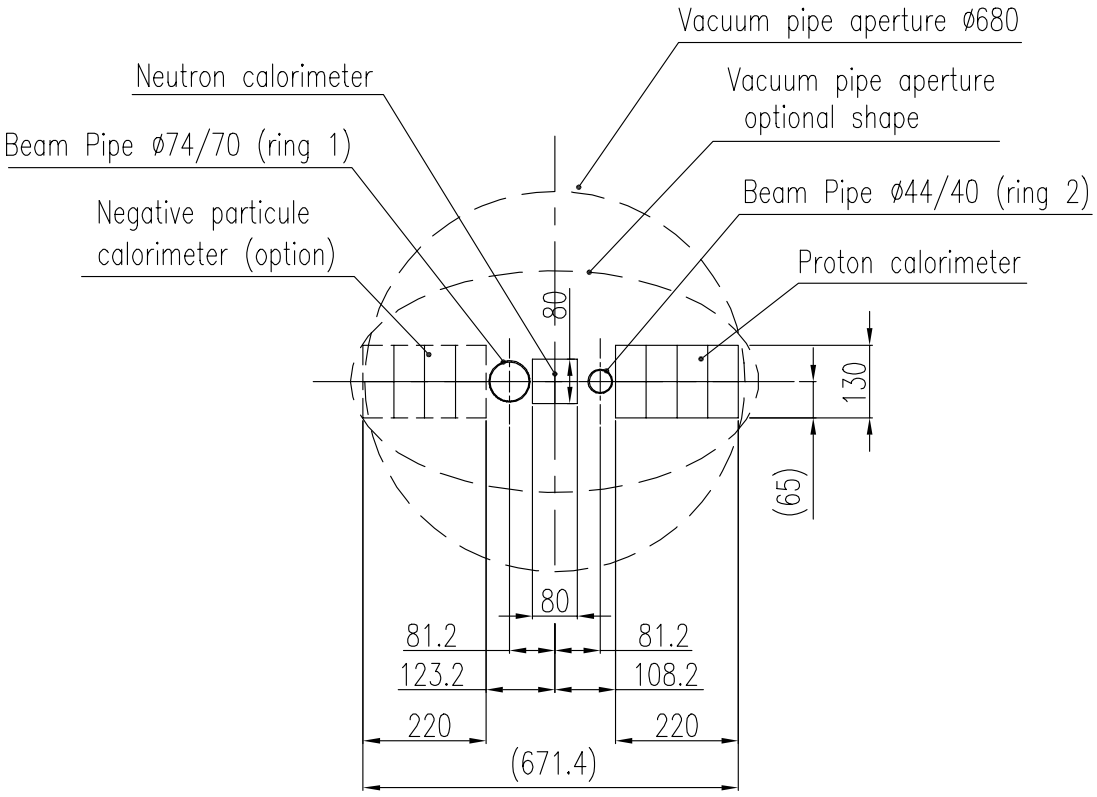

Figure 3.3: Cross-section of the beam line 115 m from the IP, with the possible location for the set of ZDCs.

The total distance from the intersection region to the front face of the neutron calorimeter is then about 116 m, whilst that of the proton calorimeter is about 115.5 m. A cross-section of the beam line at a distance of ≃ 115 m from the intersection point can be seen in Fig. 3.3.

3.3 Simulation of the LHC line

The geometry of the insertion region and the ZDCs have been described by means of GEANT 3.21; the same package has also been adopted to track the particles in the set-up.

The spectator nucleons are generated at the IP taking into account beam parameters such as the crossing angle and the intrinsic divergence. The average momentum corresponds to the nominal beam

energy of 2.76 TeV and the spread due to the Fermi momentum, approximated with a two-gaussian function [1], has been taken into account. The production of fragments, discussed in Section 4.3 on page 69, has been simulated with a parametrization of the ALADIN results [2], and can be included in the simulation. The large rapidity distribution of the secondary particles has been simulated using the VENUS and HIJING event generators.

The set-up description includes the muon dipole, the dipole corrector magnet, the inner triplet, the D1 separator magnet, and the beam pipes.

3.3.1 Tracking of spectator protons

Because of the separation magnet D1 the spectator protons will be separated from the spectator neutrons. The spatial distribution of the spectator protons on a plane normal to the LHC beams axis located 115 m away from the intersection point has been found to strongly depend on the Fermi momentum of the nucleons and on the parameters of the LHC optics.

The longitudinal component of the Fermi momentum is particularly important, being boosted by the Lorentz transformation. In Fig. 3.4 the distribution of the longitudinal component of the spectator proton momentum is shown. The momentum spread, of the order of 400 GeV/c, results in a large horizontal dispersion after the separator dipole D1.

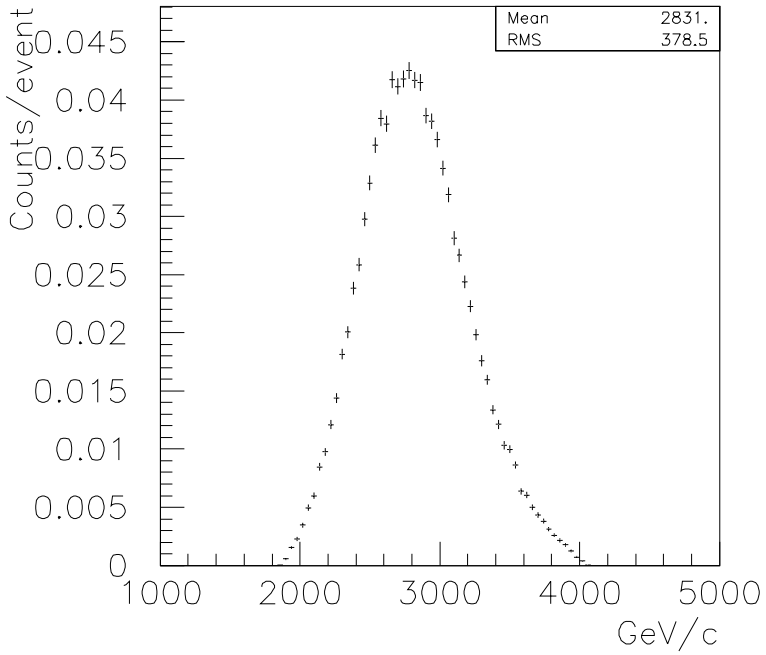

Figure 3.4: Longitudinal component of the Fermi momentum in the lab frame.

The relevant parameters of the LHC optics for tracking the spectator protons are the sign of the field of the insertion quadrupoles (inner triplet) and the crossing angle of the two beams at the IP.

The polarity of the insertion quadrupoles is imposed by the beam injection system. It corresponds to the optimal protection of the experiment and of the machine elements in case of a mis-firing of the injection kickers. A $\pm 100\,\mu$rad beam crossing allows the beam-beam tune shift due to parasitic crossings in the region common to the two rings to be limited. However, the azimuth of the plane containing the crossing trajectories is still a free parameter: we studied the influence of this tilt of the crossing plane on the size and position of the spectator spot at the ZDC location.

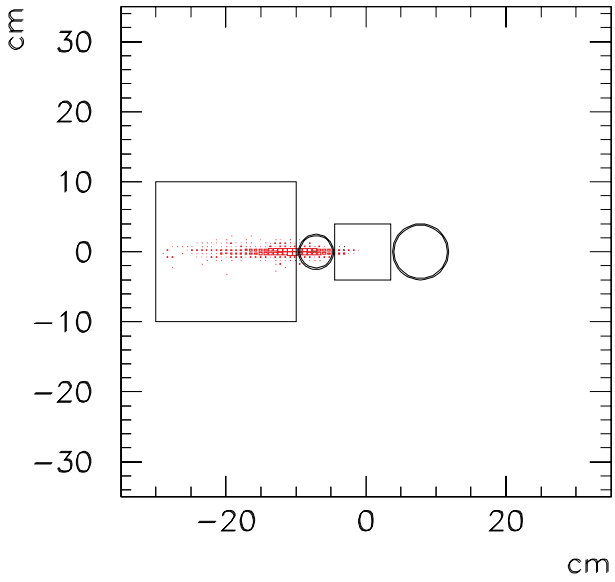

Figure 3.5: Spectator proton's spot on a plane normal to the LHC axis for a horizontal crossing angle.

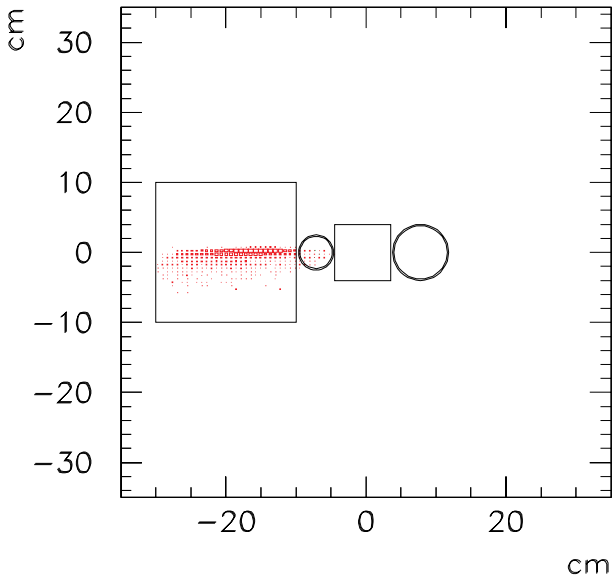

Figure 3.6: Spectator proton's spot on a plane normal to the LHC axis for a vertical crossing angle.

In Fig. 3.5 one can see the proton spot, together with a possible choice of the detector geometry, when the crossing angle is in the horizontal plane, whilst in Fig. 3.6 the proton distribution is plotted when the crossing angle lays in the vertical plane. It is clear that a vertical crossing plane is a considerably better choice, leading to 95% detection efficiency for spectator protons. If the crossing plane is kept horizontal, 38% of the protons are lost inside the beam pipe.

All the previous calculations were performed using the LHC optics version 5. The requirement for a vertical crossing plane has been accepted by the LHC parameter committee and it has been implemented in the recent version 6.

Finally, the acceptance of the proton ZDC closely depends on the aperture of the separation magnet D1. Figure 3.7 gives an idea of the trajectories of the spectator protons and clearly shows that the aperture of D1 is the crucial point in the line. Assuming an inner diameter of 73 mm for the beam pipe inside

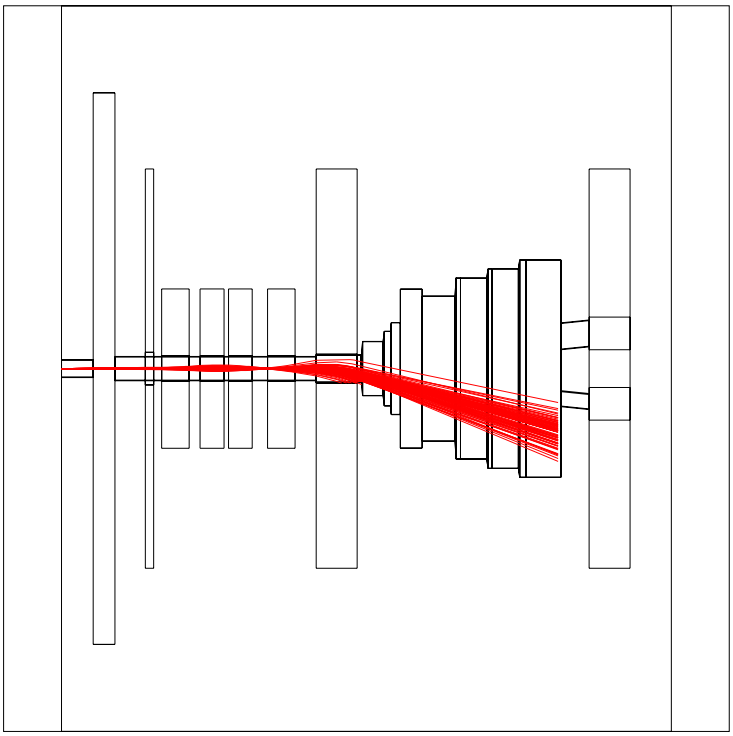

Figure 3.7: GEANT display of a set of spectator proton tracks. Secondary particles are not considered.

the coils of D1, the simulation shows that 13% of the protons interact within the beam pipe at the exit of D1 and miss the ZDCs. Clearly, any further decrease of the D1 aperture as well as variations of the position of the closed beam orbit (expected to be of the order of 1 mm [3]) could result in a stronger loss of the spectator protons. To further investigate this point, we studied the acceptance of the proton beam calorimeter varying both the aperture of the $\sim$ 1 m long pipe just beyond the D1 coils (i.e. inside the cryogenic tank of the magnet) and the displacement of the closed orbit in the horizontal plane. The results, shown in Fig. 3.8, indicate that the number of protons reaching the ZDC strongly decreases with the aperture of the beam pipe. Furthermore, the dependence of the proton loss on the aperture becomes much steeper as the orbit displacement increases. This shows that both the beam pipe aperture and the position of the orbits have to be carefully controlled in this area.

3.3.2 Tracking of nuclear fragments

With the same simulation program we tracked fragments produced in the collision. Owing to their magnetic rigidity, very close to the beam one, we find that at the ZDCs' location all the fragments are contained in the 44 mm beam pipe and cannot be detected. The fragmentation algorithm used in the simulation and the consequences of the limited nuclear fragmentation on the performances of the detector will be detailed in Section 4.6 on page 72.

3.3.3 Tracking of spectator neutrons

The spectator neutrons are emitted with the same momentum direction as the beam. The smearing due to the Fermi momentum is taken into account as for the spectator protons; only the transverse component of the Fermi momentum plays a role in determining the size of the spot at the ZDC location. Therefore, the transverse spread on the front face of the neutron calorimeter, as can be seen in Fig. 3.9, is quite small (0.6×0.6 cm^2 at 1 σ level) and we expect no losses of neutrons along the beam line.

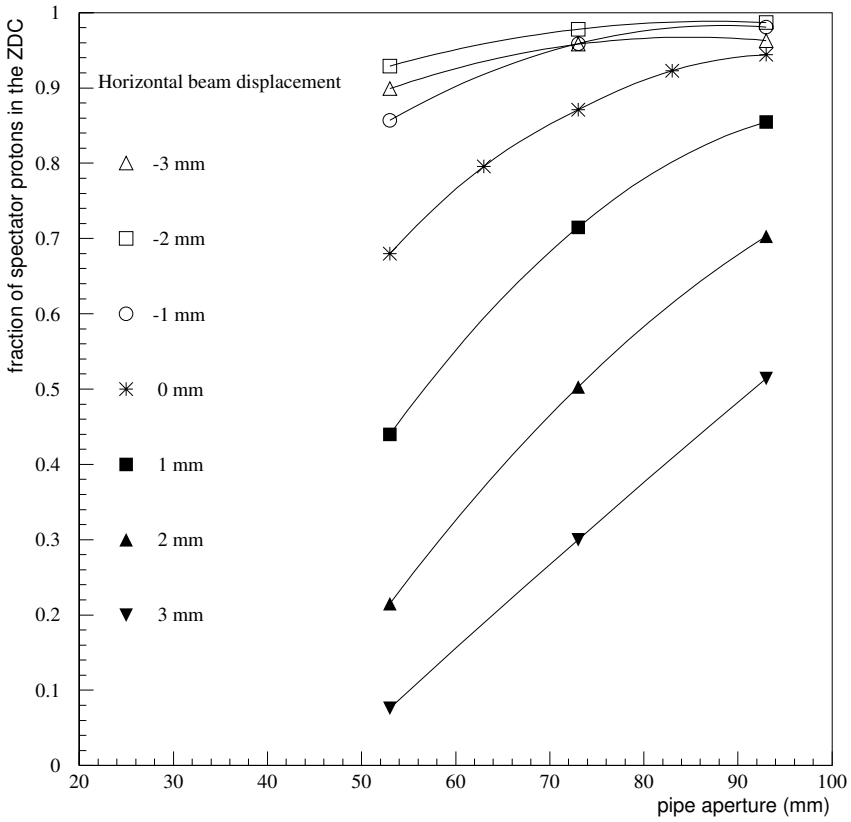

Figure 3.8: Fraction of spectator protons seen by the ZDC as a function of the aperture of the pipe beyond D1, for different horizontal displacements of the closed beam orbit.

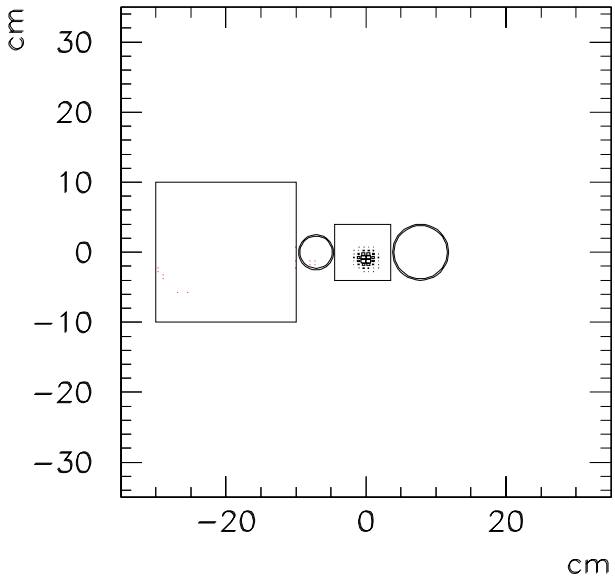

Figure 3.9: Spectator neutron's spot on a plane normal to the LHC axis for a vertical crossing angle.

3.3.4 Tracking of participants

In a ZDC, the energy carried by the secondaries generated in the collision, being correlated with the impact parameter, represents a source of background for the spectator's detection. To investigate this topic a sample of 1500 minimum bias events has been generated using VENUS. The secondary particles after the resonance decays have been tracked through the set-up. Firstly we calculated the number of particles produced at the IP (participant protons and neutrons, charged pions, photons). As can be seen in Fig. 3.10, the contamination is quite small (at most one participant neutron/min bias event). If the

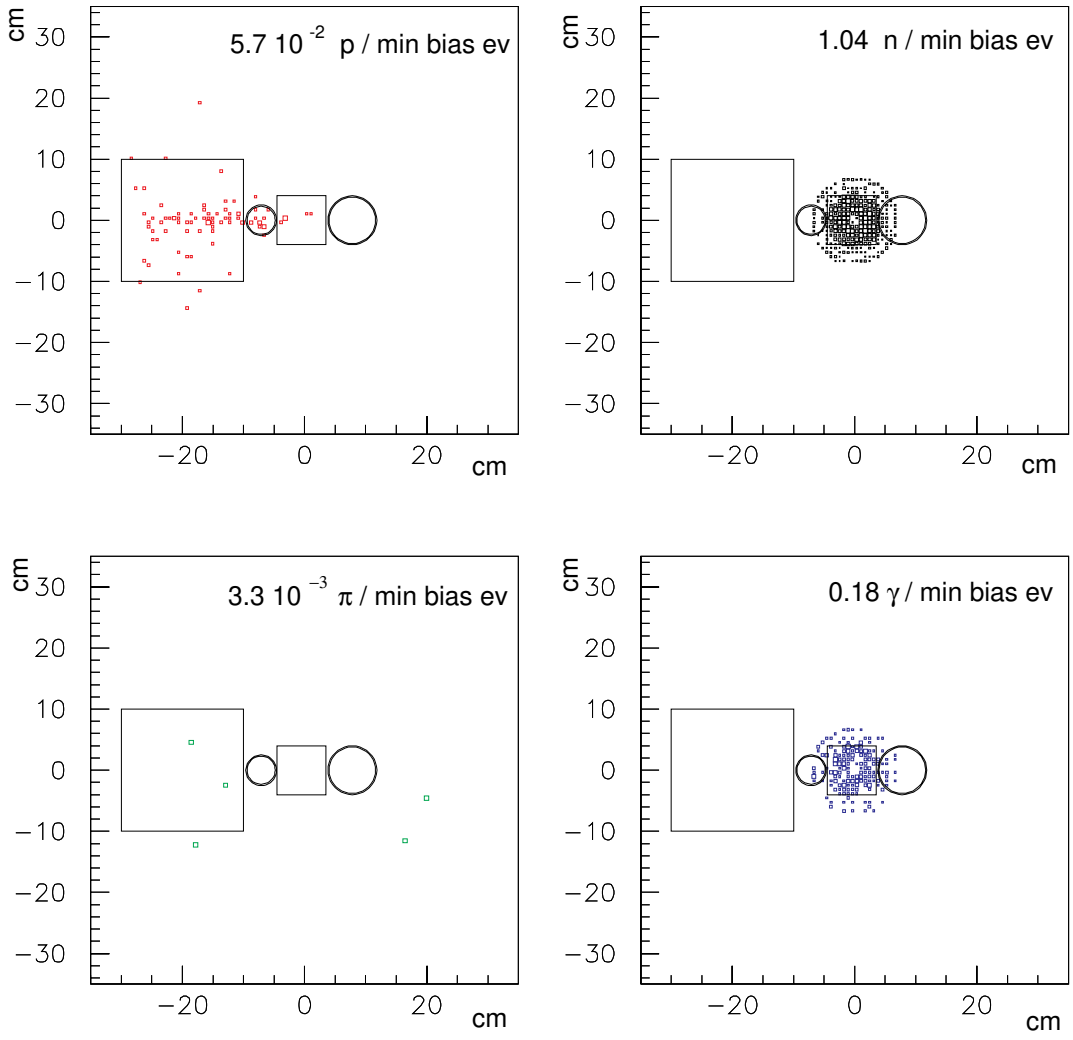

Figure 3.10: Spot of secondaries produced at the IP, tracked up to the front face of the ZDCs.

particles generated along the beam line through interactions with the magnets and/or the beam pipes are taken into account, the only source of background which strongly increases is the one due to photons, as can be seen in Fig. 3.11. However, most of these particles are quite soft, and do not significantly affect the ZDC energy measurement. For the most central events, where the contamination is larger, the amount of this background is of the order of 10% for the neutron ZDC. For the proton ZDC the participant induced background is found to be negligible.

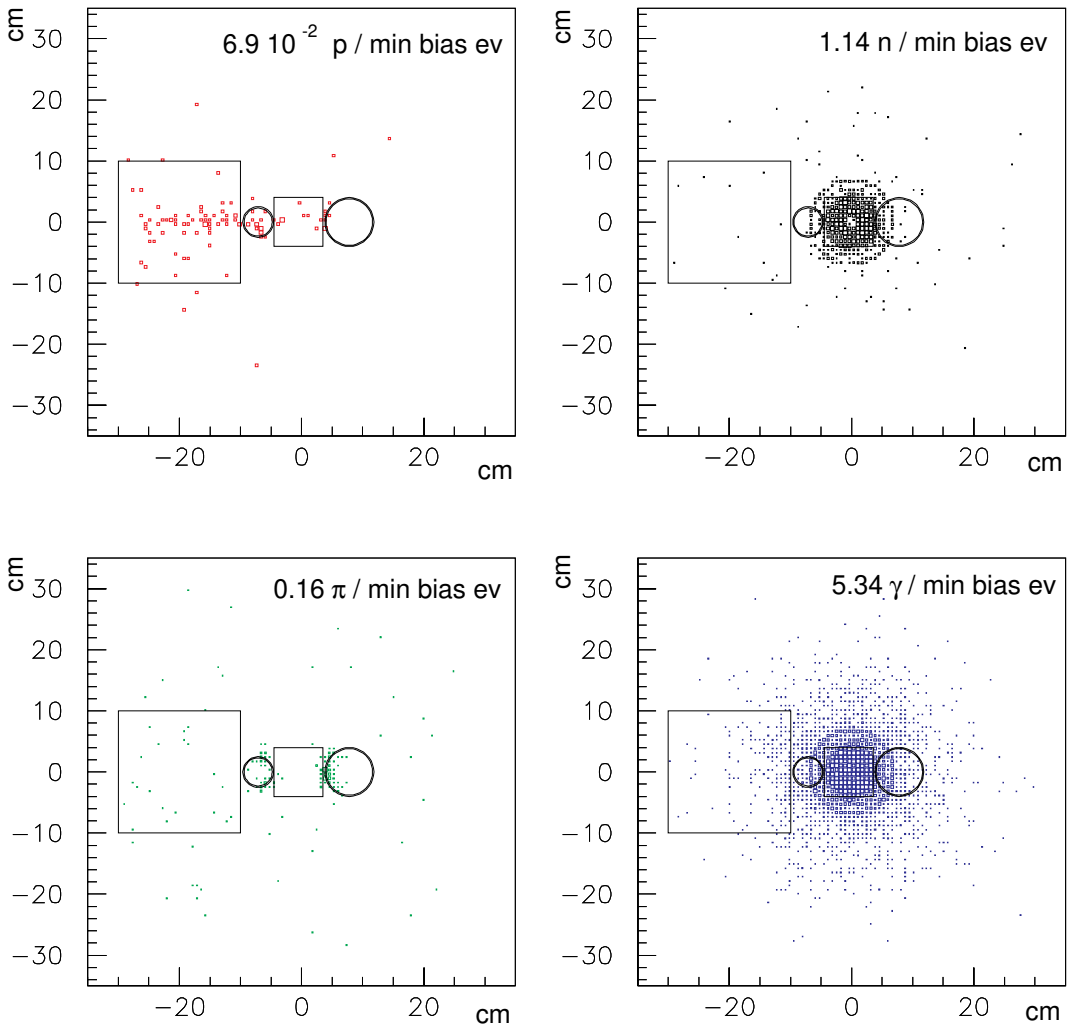

Figure 3.11: Spot of secondaries produced at the IP and along the beam line, tracked up to the front face of the ZDCs.

3.3.4.1 Detection of negative-charged particles in a ZDC

In the TP a third calorimeter (ZNP), placed symmetrically to the proton ZDC was proposed, to detect the negatively-charged particles produced in the collision, mainly pions; the aim of this device was to help subtract the background caused by the participants in the proton ZDC. However, as discussed above, the background in the proton calorimeter, caused by the particles produced in the collision, turns out to be negligible. This can be seen further in Fig. 3.12, where the energy caused by the participants and the spectators is compared.

Therefore, at this stage of the project, it does not seem useful to build a calorimeter for negative particles; nevertheless, we propose not to modify the conical pipe and to leave some free space for a possible insertion of a dedicated detector at very high pseudorapidity, if the physics requires it.

3.4 The neutron calorimeter

The design of the neutron calorimeter is similar to that of the NA50 ZDC. It consists of heavy metal absorber plates stacked to form a parallelepiped. The quartz fibres embedded in the absorber are placed

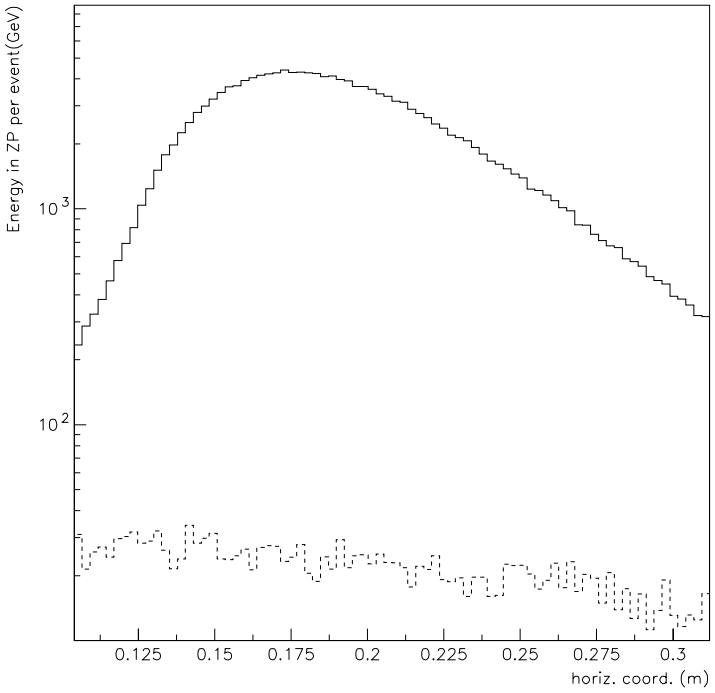

Figure 3.12: Energy of spectator protons vs. the distance from the LHC beam axis, with the background caused by participant particles (dashed histogram).

at 0° with respect to the LHC axis. The spectator neutrons, impinging on the front face of the detector, produce showers in the absorber/quartz matrix and the charged particles above the Cherenkov threshold produce photons that are transmitted through the quartz fibres up to the photodetectors.

3.4.1 Absorber

As we have seen in the previous section, the distance between the beam pipes in the horizontal plane (7 cm) is the major geometrical constraint for the neutron calorimeter.

In order to have maximum shower containment we are forced to use a dense material with a small value of the interaction length. We choose tantalum because it can be machined in our local mechanical workshop and the price (about 1 kCHF per kg) is affordable. Denser materials which could be used are either tungsten or tungsten alloys; however, the first cannot be grooved and the second is too expensive (more than twice the price of tantalum). The density of tantalum is 16.65 g/cm^3 and its interaction length is 11.5 cm.

3.4.2 Fibres

The maximum light yield from the fibres is obtained with fibres placed at 45° with respect to the initial particle direction. However, at the LHC energy, the number of photoelectrons produced in calorimeters with fibres oriented at 0° is so large that its fluctuations are negligible and the resolution is dominated by a constant term due to the loss of particles outside the calorimeter and to non-uniformities in the calibration of the various towers. In fact, the simulation and the NA50 results tell us that 0.3 to 0.5 photoelectrons per GeV are produced in calorimeters with the fibres placed at $\simeq 0°$.

We plan to use the same type of fibres (HCG-M-365-U manufactured by SpecTran Specialty Optics Company, USA) adopted for the NA50 ZDC; a raw estimate of the received dose in the ALICE experiment (1 Mrad per day) allows us to establish that they should not be seriously damaged after ten years of

LHC operation. The fibres have a pure silica core, silica fluorinated cladding, and a hard polymer coat with a diameter of 365, 400, and 430 μm, respectively. The numerical aperture is 0.22.

3.4.3 Dimensions and filling ratio

The choice of the the filling ratio, i.e. the ratio of active volume to the absorber volume, and the dimensions of the detector have been finalized on the basis of a simulation of a calorimeter filled with quartz fibres uniformely distributed in the absorber, with a fixed transversal size (7×7 cm^2) imposed by the available free space between the beam pipes.

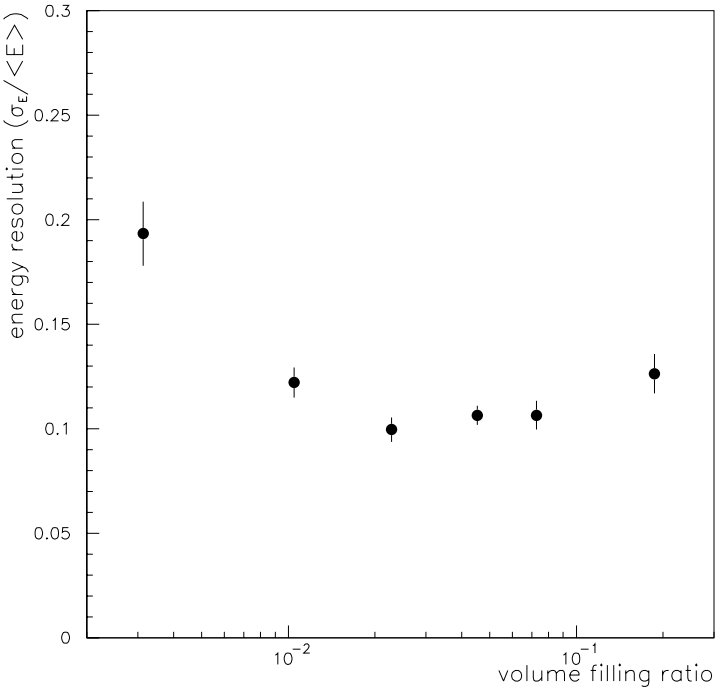

Figure 3.13: Resolution of the neutron calorimeter as a function of the filling ratio.

The filling ratio has to be chosen to optimize the energy resolution. We have considered a calorimeter made of tantalum and 365 μm diameter fused silica fibres with a numerical aperture value of 0.22. Neutrons with 2.7 TeV incident energy have been generated, with a gaussian spatial distribution (the σ of the distribution was 0.6 cm, according to the results obtained in the previous section), and the hadronic shower has been propagated in the detector. In Fig. 3.13 the resolution as a function of the filling ratio is shown for a 1 m long calorimeter. We decided to have a filling ratio equal to 1/22, which corresponds to 1936 fibres. The distance between adjacent fibres is 1.6 mm, resulting in a transverse dimension of 7.04 $\times$7.04 cm^2. The distance between the fibres is smaller than $X_0/2$ (X_0^{Ta} = 0.4 cm), in order to have a unifom response as a function of the particle impact point on the front face of the calorimeter, as we have seen in the prototype tests.

The resolution and the response of the calorimeter have then been studied as a function of its length, with the results shown in Fig. 3.14. The dashed area corresponds to the results for a calorimeter of infinite length. A length of $\sim$ 100 cm, corresponding to 8.5 λ_i, has been chosen for the neutron ZDC. With such a length the expected resolution is $\sim$ 10%; additional material in the longitudinal coordinate does not significantly improve the resolution of the device.

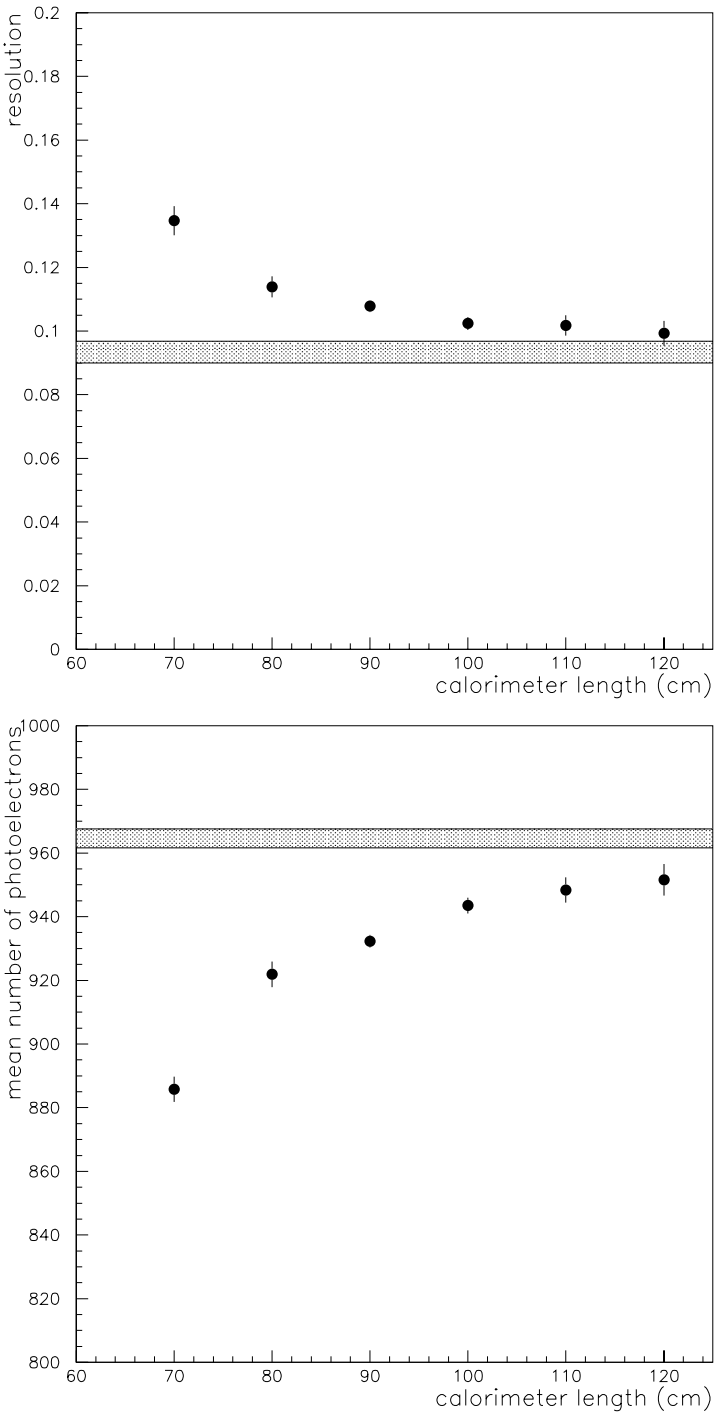

Figure 3.14: Resolution (top) and mean number of photoelectrons (bottom) of the neutron ZDC as a function of the calorimeter's length.

3.4.4 Mechanical structure

The calorimeter is made of 44 stacked tantalum plates mechanically independent. The plates are grooved as shown in Fig. 3.15; in Table 3.2 the dimensions and tolerances of the grooves are listed.

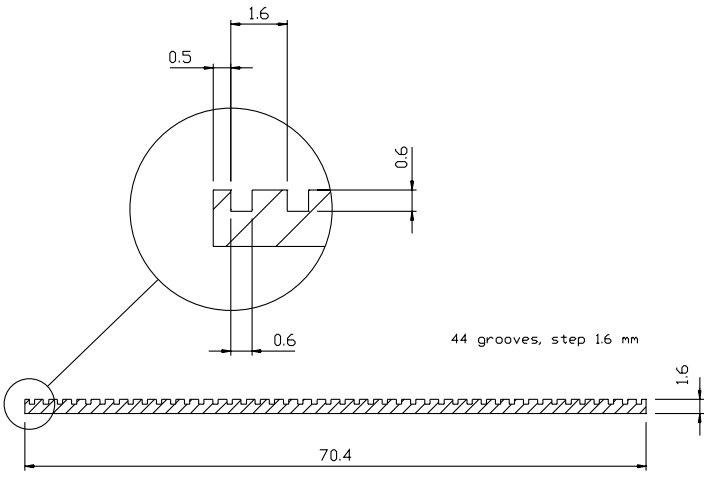

Figure 3.15: Schematic layout of a neutron ZDC grooved plate.

Table 3.2: Dimensions of grooves in the neutron ZDC absorber plates.

Groove centre to centre (mm)	1.6 ± 0.05
Groove depth (mm)	0.6 ± 0.06
Groove width (mm)	0.6 ± 0.05

The containing box is made of a bottom plate and two lateral walls. On the top, there are cross bars with a 10 cm pitch; in each of these bars there are a couple of screws that vertically press the tantalum plates by means of a stainless steel plate. The mechanical structure of the calorimeter box is shown in Fig. 3.16.

3.4.5 Segmentation

A good spatial reconstruction of the impact point on the front face of the calorimeter is not essential for the 0° energy measurements.

Nevertheless, it could be useful to divide the optical readout of the calorimeter into four independent towers; in this way it is easy to see if the calorimeter is centred and to monitor the relative damage to the different sections. On the other hand, in order to make the energy calibration easier, it could be helpful to have the light from the whole calorimeter read by a single photodetector. The online calibration could then be provided by the signal due to the electromagnetic dissociation of the colliding nuclei, as discussed in Section 3.10.

To fulfil these two requirements and to allow for some redundancy, we plan to send one out of every two fibres to a single photodetector (PMTc) and the remaining fibres to four different photodetectors (PMT1 to PMT4) collecting the light from the four towers. The connections of the fibres to the different photodetectors are shown schematically in Fig. 3.17.

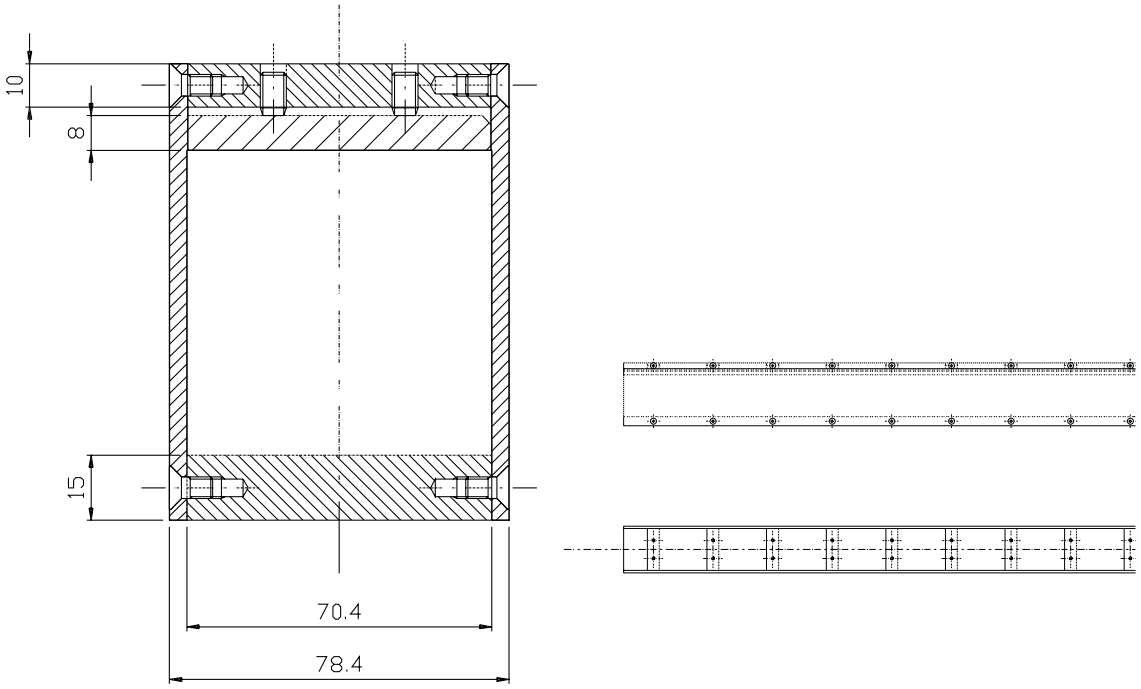

Figure 3.16: Layout of the box containing the neutron calorimeter.

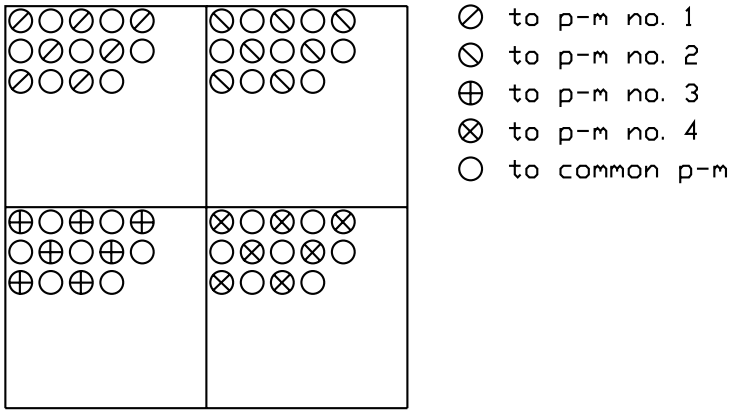

Figure 3.17: Schematic connections of the fibres to the PMTs for the neutron calorimeter.

3.4.5.1 Compensation

The quartz fibre calorimeters are fully sensitive to electromagnetic showers but not to the low-energy charged pions that represent a sizable fraction of the hadronic shower. Therefore, the response to electrons and pions of the same energy is not equal; in particular the ratio e/π between the two responses depends on the energy of the incoming particles. As an example, the ratio measured for the NA50 ZDC was ~ 2.4. The non-compensation implies that the response of the ZDC to hadrons is not linear as a function of energy [4]. However, this non-linearity is not an issue for the ZDCs, as these calorimeters mostly detect spectator nucleons, all of them with the same energy, apart from the Fermi momentum spread; the contribution of non-spectator nucleons is negligible, being at most 10%, as seen in Section 3.3.4. Therefore, we will not longitudinally segment the calorimeter into e.m. and hadronic sections.

3.4.6 Photodetectors

The specifications for the PMTs are based on the experience gathered in the design of the NA50 ZDC and on the R&D work on the prototypes. The basic phototube properties are determined by requirements on:

- photocathode type and PMT window
- dynamic range
- average and peak anode currents
- gain

The photocathode is of the standard bialkali type, with a quantum efficiency around 25%. The use of a standard borosilicate glass window gives a loss of UV light of about a factor of 3, but does not significantly affect the energy resolution of the calorimeter.

The maximum dynamic range required for PMTc goes from 200 to 9×10^4 photoelectrons, whilst the dynamic range for the four PMTs connected to each tower goes from 10 to 2.2×10^4 photoelectrons. The minimum number of photoelectrons corresponds to only one neutron coming out from the e.m. dissociation, and the maximum number is reached in the very peripheral events when all the spectator neutrons hit the front face of the calorimeter. Therefore, the linear dynamic range required for the tubes is less than 3000, a value which presents no difficulty for standard PMTs.

The PMT gain has to be chosen to keep the average anode current I_a below the maximum acceptable value (for example, about 100 μA for an XP2242B tube [5]). In fact, when I_a approaches this value, instabilities of the PMT response start to occur. The acceptable gain value should be around 10^5, taking into account the expected luminosity and the cross-sections for the e.m. dissociation and the hadronic interaction of the Pb nuclei.

Particular care is also taken in the design of the voltage divider, where transistors have to be used to achieve a stable behaviour [6].

The final choice of the PMTs will be made at the time of ordering, depending on the models available from the commercial manufacturers which satisfy the aforementioned requirements. The use of other photosensors, such as HPDs, with a higher dynamical range but smaller gain, could also be envisaged as a possible option.

3.5 Proton calorimeter

The design of the proton calorimeter is conceptually similar to that of the neutron one. The main constraint comes here from the need to optimize the detection of the spectator protons, which are spread over the horizontal coordinate by the separator magnet D1, as seen in Fig. 3.7 on page 44.

3.5.1 Absorber

Even if a very high density material, like tantalum, is well suited as an absorber for the proton calorimeter (ZP), the size of the spot of the spectator protons (90% of the protons lay in a 12.6×2.8 cm^2 large area) leads us to the design of a rather large device, thus requiring the use of a less expensive absorber, such as copper or brass. We prefer to use brass, as it can be easily machined; its density is 8.48 g/cm^3, and its interaction length is 18.4 cm.

3.5.2 Fibres

Following the considerations outlined in Section 3.4.2, we will use quartz fibres, positioned at 0° with respect to the LHC axis.

The core, the cladding, and the polymer coat diameters are 550, 600, and 630 μm, respectively, larger than the ones used for the neutron ZDC, in order to reduce the number of fibres at a constant filling ratio, and consequently the complexity of the absorber machining. The type of the fibres is HCG-M-550-U, manufactured by SpecTran Specialty Optics Company, USA. The numerical aperture of the fibres is 0.22.

3.5.3 Dimensions and filling ratio

We simulated a calorimeter made of brass and 550 μm diameter quartz fibres. Protons with 2760 GeV incident energy were tracked through the beam line from the IP to the ZDC location. We chose 20.8 $\times$ 12 cm^2 as the transverse dimension for ZP. This choice ensures that 99% of the protons which have not been lost along the magnetic line are collected. The hadronic shower was then followed in the detector and the energy resolution as a function of the filling ratio calculated. The results are shown in Fig. 3.18. We chose a filling ratio equal to 1/65, which corresponds to 1560 fibres. The distance between the fibres is 4 mm; such a spacing of the fibres ensures a good uniformity of the response as a function of the impact point, as seen for the ZP2 prototype (Fig. 2.iii, in colour, on page 38) which has an identical fibre pitch.

We have chosen for ZP the same length, expressed in λ_i, as that of the neutron calorimeter. This leads to a 150 cm long calorimeter.

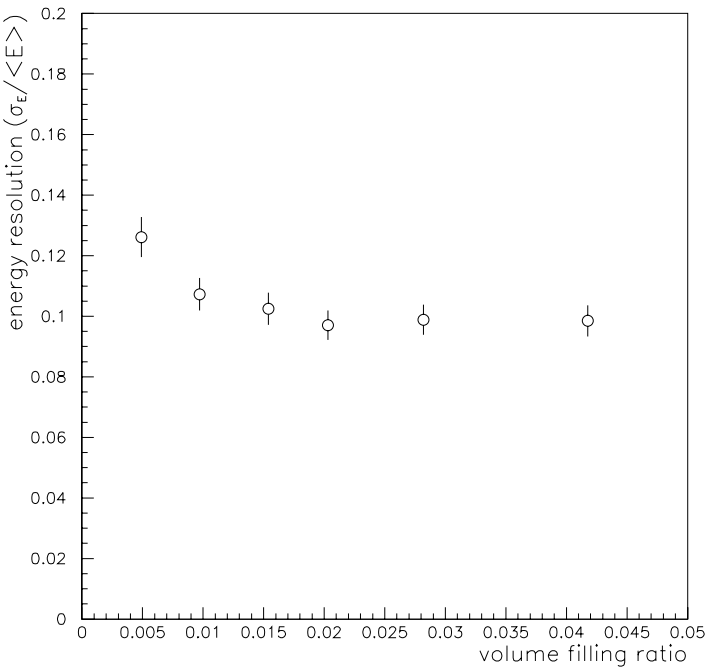

Figure 3.18: Resolution of the proton calorimeter as a function of the filling ratio.

3.5.4 Mechanical structure

The calorimeter is made by stacking 52 brass grooved plates. Fig. 3.19 shows one grooved plate and in Table 3.3 the dimensions and tolerances of ZP grooves are listed. The containing box is conceptually similar to the neutron calorimeter one, except for the larger dimensions.

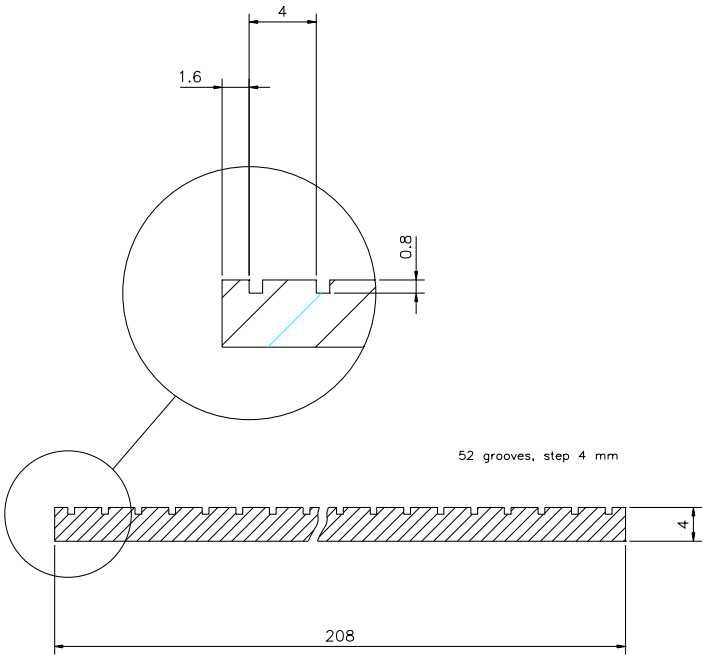

Figure 3.19: Schematic layout of a grooved plate of the proton ZDC.

Table 3.3: Dimensions of grooves in the proton ZDC absorber plates.

Groove centre to centre (mm)	4.0 ± 0.05
Groove depth (mm)	0.8 ± 0.06
Groove width (mm)	0.8 ± 0.05

3.5.5 Segmentation

As with the neutron calorimeter, we plan to divide the optical readout into five PMTs. One of the PMTs collects the light of half of the fibres uniformely distributed inside the calorimeter. This allows an easy on-line check of the stability of the response of the calorimeter, through the e.m. dissociation, as already discussed in Section 3.4.5. With the remaining fibres we define four towers of 5.2×12 cm^2, read out by four PMTs. The schematic arrangement of the fibres is shown in Fig. 3.20.

3.5.6 Photodetectors

As the signal from the PMTs of the proton calorimeter are of the same order of magnitude as those from the neutron one, we plan to use the same type of photodetector.

3.6 Electromagnetic calorimeter

Further information on the centrality of the collision can be provided by an electromagnetic calorimeter (ZEM), which detects, event-by-event, the energy carried by photons in the forward direction.

The original idea in the TP was to place a small e.m. calorimeter just in front of the neutron one. The simulations have shown that the energy carried by γs, mostly originated by π^0 decays, in the pseudorapidity interval covered by the neutron calorimeter, is less than 10% of the energy carried by the neutrons

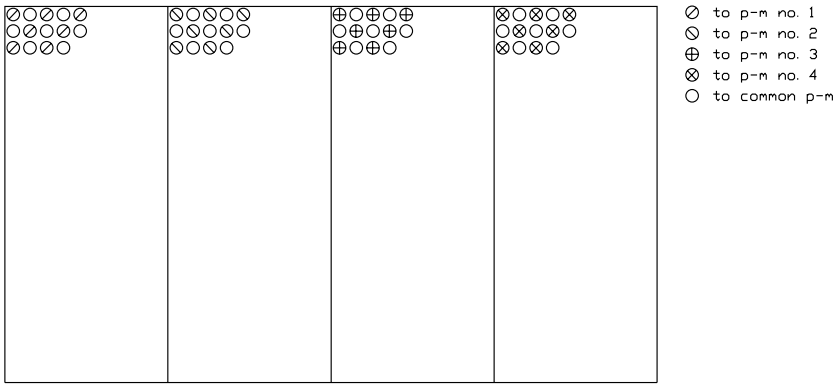

Figure 3.20: Schematic connections of the fibres to the PMTs for the proton calorimeter.

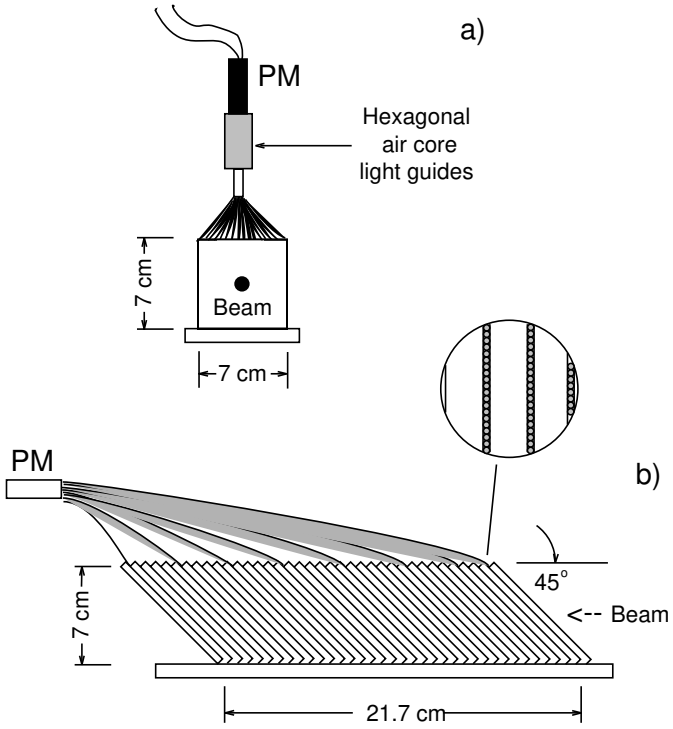

Figure 3.21: Schematic front (a) and side (b) views of the e.m. calorimeter.

(both spectator and participant neutrons). This means that the fluctuations on the energy released by the neutrons in the e.m. calorimeter are so big that they can spoil the measurement of the e.m. energy. In particular, if the energy carried by γs is less than 20%, the calculations have shown that there is no chance of distinguishing the two contributions event-by-event.

Nevertheless, the measurement of the γ forward energy can still be carried out, by placing the e.m. calorimeter outside the acceptance of the neutron ZDC. Assuming an aperture of the separator magnet D1 of 73 mm, there is still an opening of a few centimetres on the top of the neutron calorimeter, where the γs produced at the IP can travel without encountering any obstacles. As a calorimeter placed just on top of the ZN is outside the acceptance of the spectator neutrons, it only measures the energy carried by participants and secondary particles. Therefore, this energy is anti-correlated with the impact parameter of the collision and it could be used to make the centrality trigger more selective and less sensitive to possible effects related to the fragmentation of the nuclei (see Section 4.6 on page 72).

We plan to add an e.m. calorimeter on each side of the IP; its dimensions will be $7 \times 7 \times 21.7$ cm^3 and it will be placed 115.2 m from the IP, 30 cm before and 7 cm above the neutron calorimeter.

The R&D tests performed during recent years and discussed in Chapter 2 suggest the use of lead as the absorber material and the use of quartz fibres tilted at 45° with respect to the LHC axis. The total absorber length corresponds to 30 X_0. The fibres have a pure silica core of 550 μm diameter with fluorinated cladding and a numerical aperture of 0.22; we will use exactly the same fibres as for the proton calorimeter. The fibres are arranged in ribbons, sandwiched between the absorber layers, consisting of flat lead plates. A schematical view of the e.m. calorimeter is shown in Fig. 3.21.

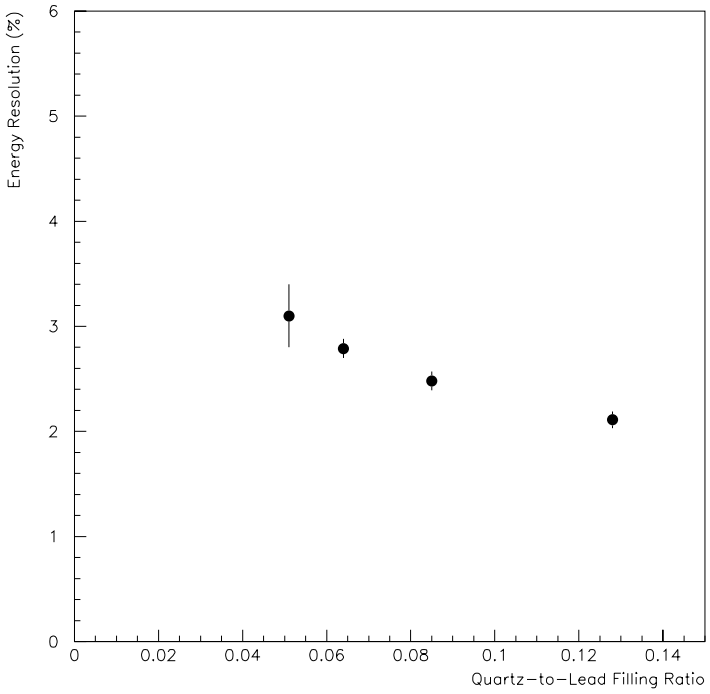

Figure 3.22: Energy resolution of the e.m. calorimeter as a function of the quartz-to-lead ratio for 270 GeV γs.

The simulation of the e.m. calorimeter has been performed using the GEANT code. The thickness of the lead plates has been varied from 2 to 5 mm, in order to study the resolution as a function of the quartz-to-lead volume ratio. Figure 3.22 shows the calorimeter energy resolution as a function of the volume ratio for 270 GeV incident photons; this energy value falls within the expected range predicted by HIJING at very forward rapidities. A packing fraction of 1/11.7 has been chosen; therefore the fibre planes will be separated by 3 mm lead absorber sheets (40 in total). The lead plates, after the 45° tilt,

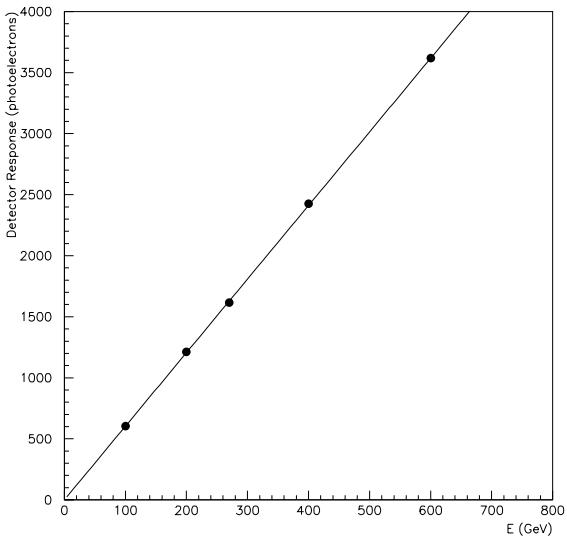

Figure 3.23: Response of the e.m. calorimeter to γs of energy from 100 to 600 GeV. The line represents a linear fit to the data.

will present to incoming particles a longitudinal absorber thickness of 4.24 mm, shorter than 1 X_0 for lead (5.6 mm) ensuring frequent longitudinal sampling of electromagnetic showers.

The linearity of the calorimeter response has been verified for simulated γ energies of 100, 200, 270, 400, and 600 GeV (see Fig. 3.23). A linear fit gives six photoelectrons per GeV.

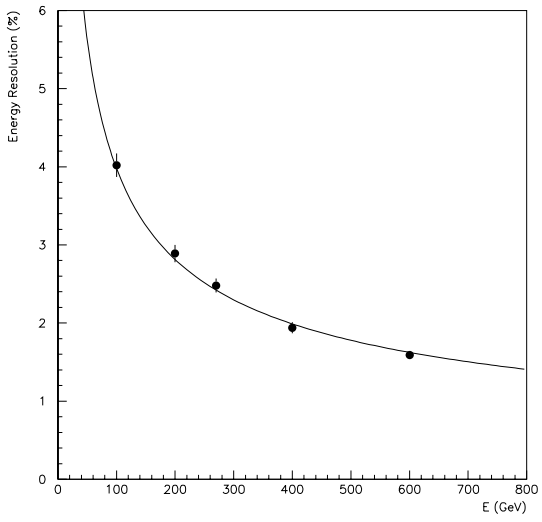

Figure 3.24: Energy resolution of the e.m. calorimeter as a function of the γ's energy.

The electromagnetic energy resolution as a function of the γ energy is shown in Fig. 3.24; a fit to the simulated points gives

$$\frac{\sigma}{E} = \frac{(39.8 \pm 0.6)\%}{\sqrt{E}} \oplus (0.0 \pm 0.4)\ \% \ .$$

The previous results were obtained for γ's entering the centre of the calorimeter with a uniform spatial distribution 0.5 cm wide. The uniformity of the response as a function of the impact point on the front

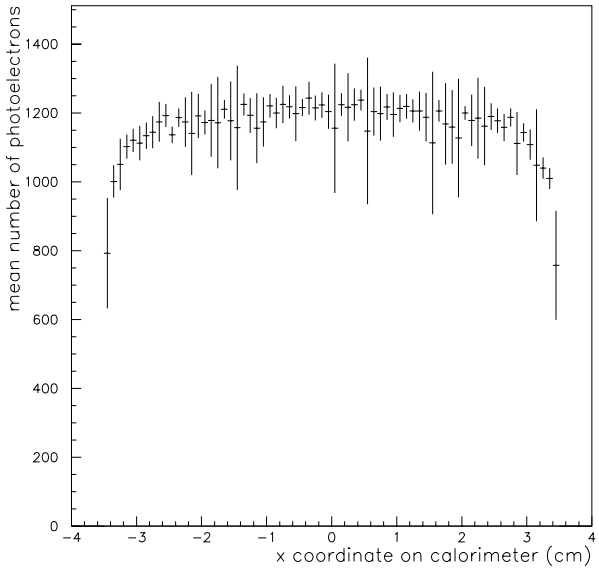

Figure 3.25: Calorimeter's response versus the horizontal coordinate of the impact point on the front face.

face of the calorimeter can be seen in Fig. 3.25.

The fibres will be extended out of the top of the absorber material to a Philips XP2020 PMT, after an air core, hexagonal light guide, used to homogenize the response of the different parts of the photocathode to different fibres.

3.7 Signal readout and transmission

The quartz fibres emerging from the back of the calorimeters are gathered together in bundles, which are turned and routed towards the photomultipliers which are located approximately 50 cm far from the end of the calorimeter in rows outside the beam horizontal plane. The fibre bundles terminate in a hexagonal aircore light guide. The light guide is needed to mix the light coming from the fibres. The signal of each PMT is transmitted through a long C-50-11-1 coaxial cable (211 m for the right set of ZDCs and 311 m for the left one) to the counting room, where the trigger logic is built.

3.8 Trigger layout and electronics

The ZDC electronic circuit is shown in Fig. 3.26. The signals from the PMTs are amplified by a factor of 10 by means of a linear amplifier (LeCroy 612A). The analog sum of the amplified signals related to each detector is performed with linear fan-in/fan-out modules (LeCroy 428F), to obtain a signal proportional to the total energy measured in each detector. These signals are indicated in the figure as 'ZNR_low-gain', 'ZPR_low-gain', 'ZNL_low-gain' and 'ZPL_low-gain' for the neutron and proton calorimeters on the right and left side of the IP, respectively. The sum of these four signals, proportional to the total number of spectators coming out from the interaction, will be sent to several inputs of a discriminator (CAEN V258B) and then to a programmable logic unit PLU1 (CAEN V495) to provide the Level 1 trigger for several centrality intervals.

The mutual electromagnetic dissociation (see Section 4.8.2 on page 79), usually gives a signal equivalent to one nucleon. We will therefore use a second amplifier stage to have such signals in the middle of the ADC range. We will fix, for each detector, a threshold window between the noise (Dlt) and the

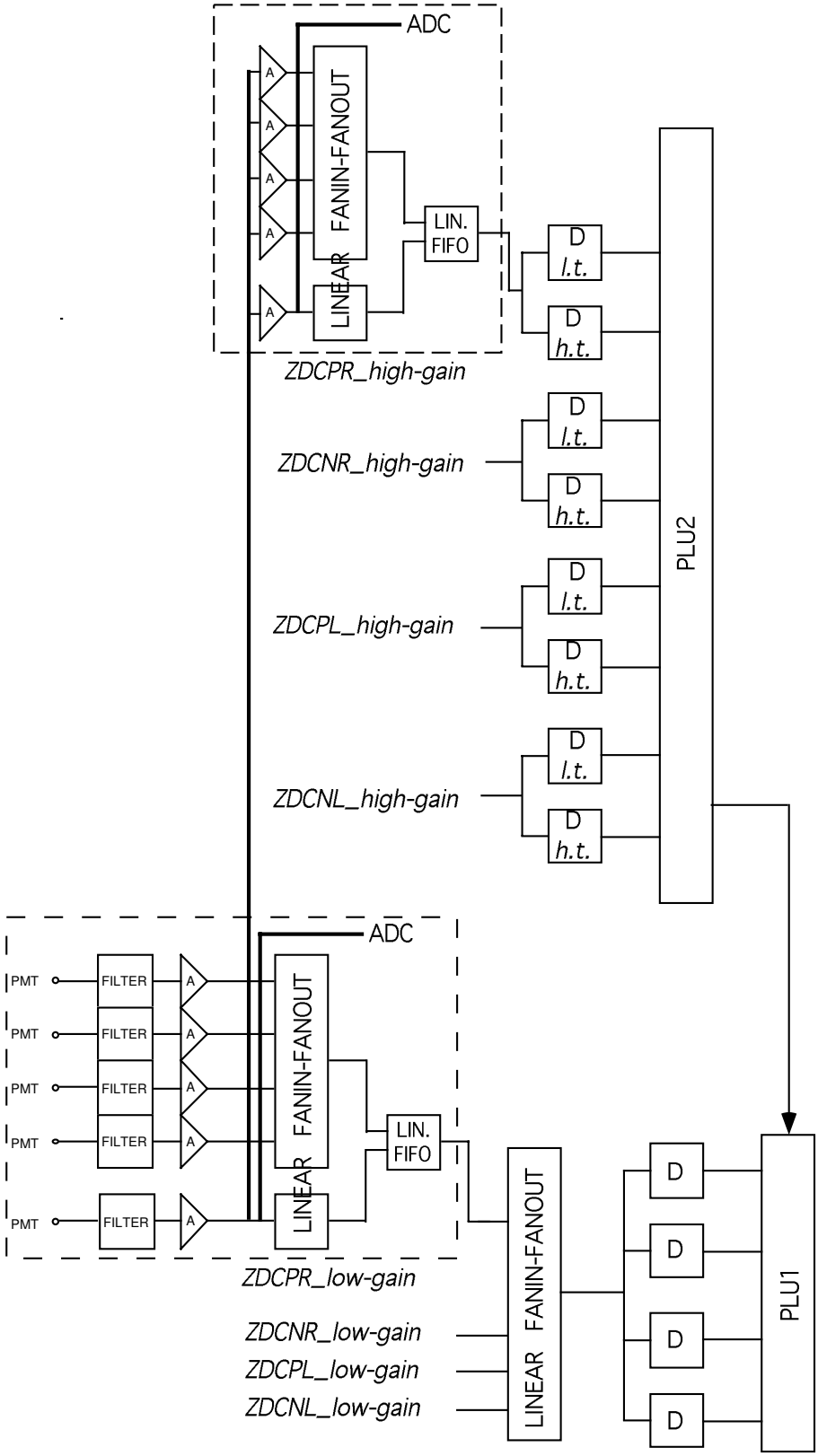

Figure 3.26: Schematic diagram of the ZDC trigger.

physical minimum bias signal (Dht), expected to be equivalent to a few nucleons at least. The coincidence of two such signals for the two sides of the IP, implemented in a programmable logic unit (PLU2), can be considered as the trigger for the mutual e.m. dissociation events. The fourfold coincidence of high threshold signals in PLU2 corresponds to a Pb-Pb hadronic interaction and will be used to strobe the PLU1.

To recover the signal widening, caused by the total cable length of more than 200 m, the analog signals are filtered in a bridge-T filter before amplification. One output signal from each amplifier will be opportunely delayed and sent to the ADC modules after being strobed by the trigger signal in linear gate modules [7], allowing the use of a gate width narrower than in a normal commercial ADC.

At the entrance of the linear gate preceding the ADC, the duration of the analog signal is expected to be about 15 ns and the gate could be 20 ns wide. All the electronics will be placed in the lowest level counting room: the amplifiers and fan-in/fan-out do not require special control during the routine data-taking whereas the discriminators will have programmable thresholds.

3.9 Trigger logic and data acquisition

3.9.1 Introduction

The ALICE trigger system is subdivided into three levels: level 0, level 1, and level 2. The ZDC detector provides information on the centrality of the collision and is used for trigger level 1.

Different types of trigger are handled by the ZDC:

- physics trigger: central interactions, dimuon triggers and electromagnetic dissociations;
- ZDC test trigger: triggered by a laser flash.

For the physics triggers, the ZDC data will be read out together with other trigger information. These data will then be assembled as a subevent and sent to the data acquisition system (DAQ) to be included in the complete event. The ZDC data will be transfered from the experimental area to the counting room by means of the ALICE Detector Data Link (DDL).

For the test triggers, the ZDC data will be read out and sent to the DAQ in a similar way. In addition, these data will be monitored to check the quality of the ZDC detector data.

The overall architecture of the ZDC readout and data acquisition system is shown in Fig. 3.27.

3.9.2 The data transfer system

The ZDC electronics of trigger level 0 and 1 will be located in the experimental area, near the ALICE detector. The readout electronics of the ZDC work permanently and provide the centrality information to the trigger logic for level 1. These electronics are located on the ZDC readout cards in the trigger system crate.

When a trigger level 1 is issued, the ZDC electronics will convert the signals and make them available for the DAQ on the ZDC readout cards. When a positive trigger level 2 is issued, the DAQ will transfer the data from the trigger system crate to the Front-End Digital Crate (FEDC). This data transfer uses the DDL in the mode to transfer data from one crate to another (see Fig. 3.28).

The physics data transferred by the DDL are buffered in the ALICE Read-Out Receiver Card (RORC) [8]. The RORC has several functions:

- be the mother card for the DDL Destination Interface Units (DIU)
- act as the receiving memory for the physics data transferred by the DDL to the DAQ;
- detect the end of the data blocks and manage the data blocks received through the DDL.

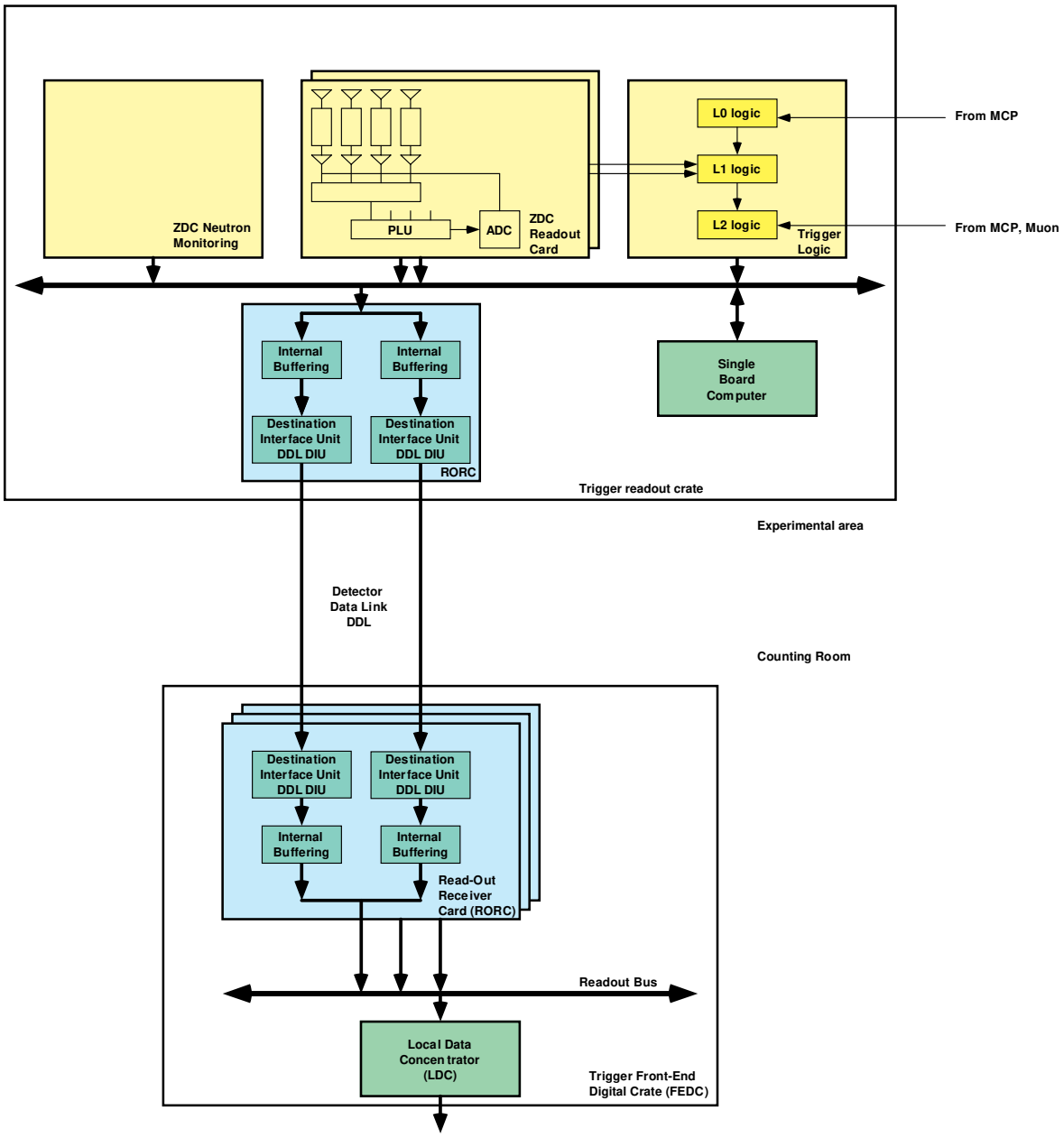

Figure 3.27: ZDC readout and data acquisition system.

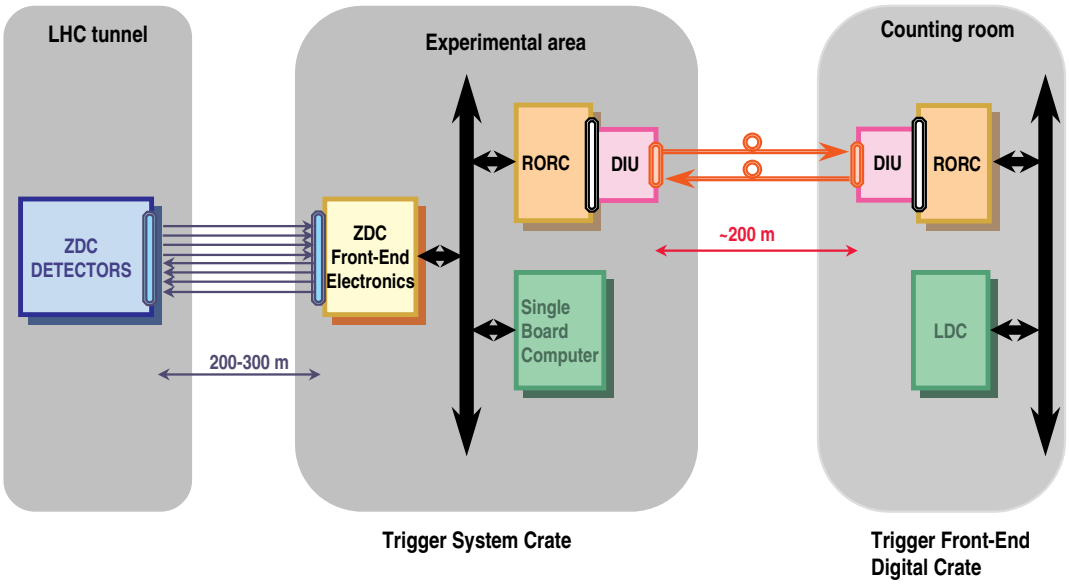

Figure 3.28: Trigger and ZDC data transfer over the DDL.

Once the data have been transferred to the RORCs, they are under the control of the DAQ system. The RORC includes enough buffering to store several tens of events from the trigger and the ZDC.

A prototype of the DDL DIU and of the RORC have been developed and are working properly. Their main characteristics correspond to the needs of the ZDC.

The data transfer system of the trigger will consist of a single Front-End Digital Crate (FEDC) including 4 RORCs and one Local Data Concentrator (LDC). A standard computer (workstation or PC) is also included in the system. It allows the trigger sub-system to work independently during the integration and installation phases and to run interactive programs to perform local tests or debugging after installation.

The current prototypes of the data transfer system use VME crates and the LDC is implemented as a single board computer running the UNIX operating system. The implementation will most probably follow the technology evolution but the main functionalities will remain.

3.9.3 The data acquisition system

The main functions of the data acquisition system when it takes part in a global run with the other ALICE detectors are [9]:

- to read out the data fragments from several RORCs and assemble them into one sub-event;
- to send the sub-event to the computer designated as the event-builder by the event building and distribution system, to build the complete ALICE event.

The data acquisition system allows data to be taken in stand-alone mode as well. In this case, the LDC records the data locally instead of sending them to the event-builder computer. This facility can be used for tests during the preparation and installation phases of the experiment.

The ZDC monitoring program will be executed by one of the DAQ computers: for example by the LDC of the FEDC trigger.

3.10 Energy calibration and stability monitoring

The calorimeter calibration and monitoring system is designed to determine the absolute energy scale and monitor the responses of the individual photodetectors for changes during the lifetime of the experiment. Three different complementary systems are envisaged for these purposes:

- test beam calibration
- light injection with a blue LED
- physics events.

The performances of each proton, neutron and e.m. calorimeter after assembly will be measured on a test beam; these runs will serve to check the response to electrons and hadrons of the highest available energies in order to intercalibrate the individual PMTs, to verify the uniformity of the responses as a function of the impact point of the particles on the front face of the calorimeter, and to measure the light yield per GeV. The availability of an ion beam at that time would be interesting to check the linearity of the response as a function of the number of incoming nucleons.

To accurately monitor the radiation damage of the fibres and the PMT gain stability, we plan to use a LED system. The whole system is sketched in Fig. 3.29. A few fibres in each calorimeter (ZF in the figure) will be longer than the normal ones and will exit from the front face of the calorimeter towards the light source. A second set of fibres (RF) will go from the source up to the front face and will be curved back to an additional PMT to monitor the radiation damage of the part of the fibre outside the calorimeter. A short fibre (SF) carries the LED light to one PMT that monitors the stability of the light source. As a light source we plan to use a fast and bright blue LED ($\lambda \simeq 470$ nm), driven by a LED driver module (e.g. CAEN C 529). A software command will pulse the LED driver and a special trigger will be used to record the monitoring events. The LED can fire during the regular data-taking, monitoring response variations with an accuracy at the level of 2 %. Two of these systems are needed to monitor the two set of ZDCs, left and right of the IP.

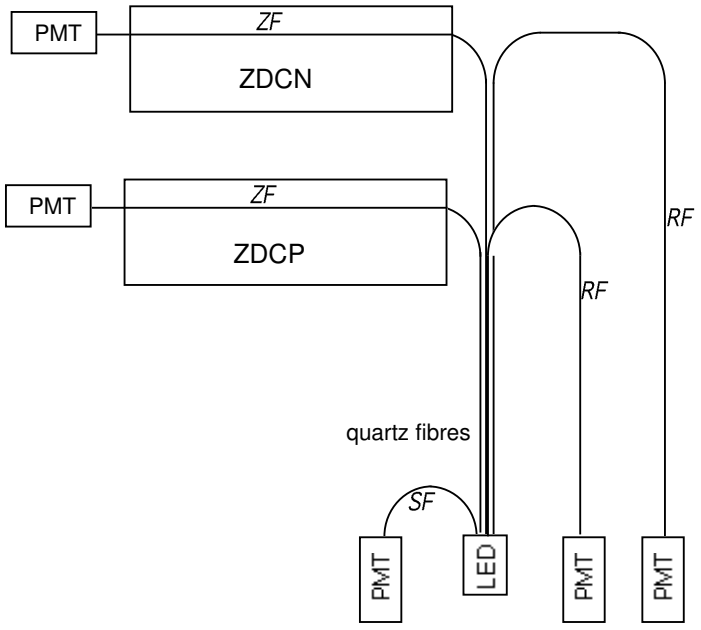

Figure 3.29: Schematic layout of the LED monitoring.

An adequate number of spare fibres will be installed to avoid problems caused by the fragility of the fibres themselves.

The mutual e.m. dissociation of the colliding nuclei results in the emission of a few neutrons, as will be explained in Section 4.8.2 on page 79. The *in situ* physical calibration will be carried out by monitoring the single neutron spectrum, obtained by the coincidence signal of one neutron on both sides of the IP.

3.11 Slow control and services

The high-voltage supply will be delivered to the PMT using some commercial units located in a rack far from the detector. The setting of the HV and the monitoring of the voltage and of the current will be performed remotely by means of a Field Bus standard (i.e. CAN), which will hopefully be adopted by the whole ALICE experiment. The number of channels to be monitored will be no more than 50 (25 for each side of the intersection point).

4 Performance of the detector

4.1 Introduction

In the previous chapters the feasibility of a set of zero degree quartz fibre calorimeters for the ALICE experiment has been demonstrated and the details of their technical design have been discussed.

In this chapter it will be shown that such detectors can provide a determination of the centrality of the nucleus–nucleus interaction, through the estimation of the impact parameter of the collision with an accuracy better than 10% over a large range of centralities. The consequences in terms of the capability of the detection of a threshold effect as a function of the centrality, as foreseen for a phase transition, will be shown.

The possible effect of a limited fragmentation of the colliding nuclei on the performance of the detector will also be investigated.

An evaluation of the efficiency of a centrality trigger based on the ZDCs, which is strictly correlated with the previous topics, will then be discussed.

Finally, the possible use of the ZDCs as a luminosity monitor will be presented.

4.2 Zero-degree energy and collision centrality

As already discussed in Chapter 1 the number of spectator nucleons N_S, which is the measurable quantity in a ZDC, is strongly correlated with the impact parameter b of the collision. By means of an analytical calculation, in the framework of the Glauber theory, or using an event generator such as VENUS or HIJING, this correlation has been evaluated and found to be largely model-independent (see Fig. 1.1 on page 2). Of course, the fluctuations in the number of spectator nucleons at fixed impact parameter limit the resolution that can be achieved through a measurement of N_S. This can be seen in Fig. 4.1 where we plot, for Pb-Pb collisions at the LHC energy, the b vs N_{Sp} and b vs N_{Sn} correlations obtained with

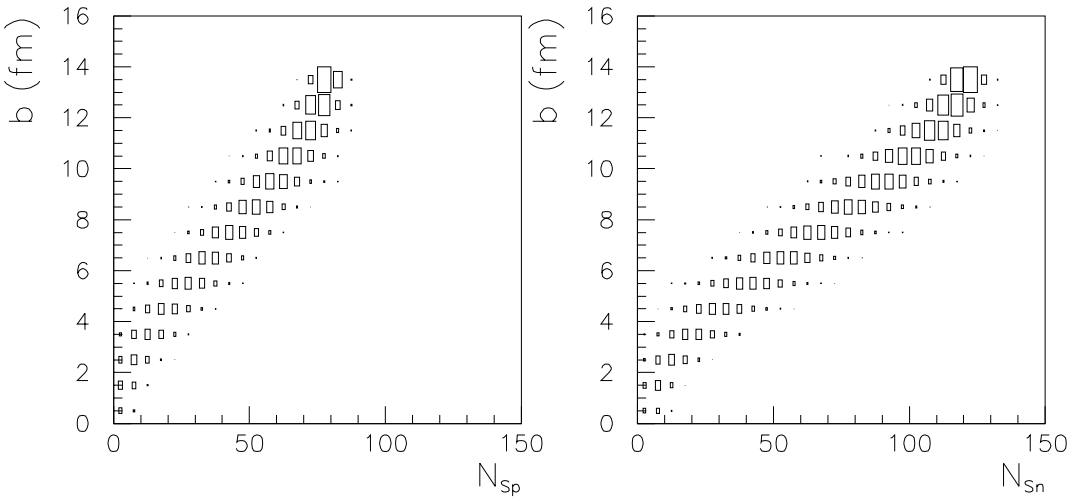

Figure 4.1: Correlation, from VENUS, between the impact parameter b and the number of spectator protons (left) and neutrons (right).

VENUS, where N_{Sp} and N_{Sn} are the number of spectator protons and neutrons, the two quantities we separately measure with the ALICE ZDCs.

To further quantify the resolution on the centrality which can be achieved through a measurement of the spectators one can easily calculate from these correlations the relation between b and σ_b/b. The result, presented in Fig. 4.2, shows that for $b > 5$ fm the resolution on the impact parameter, caused by the fluctuations of the spectators' signal, is $< 10\%$. For very central events the resolution is slightly worse, but is anyway ≤ 1 fm down to $b \approx 2$ fm.

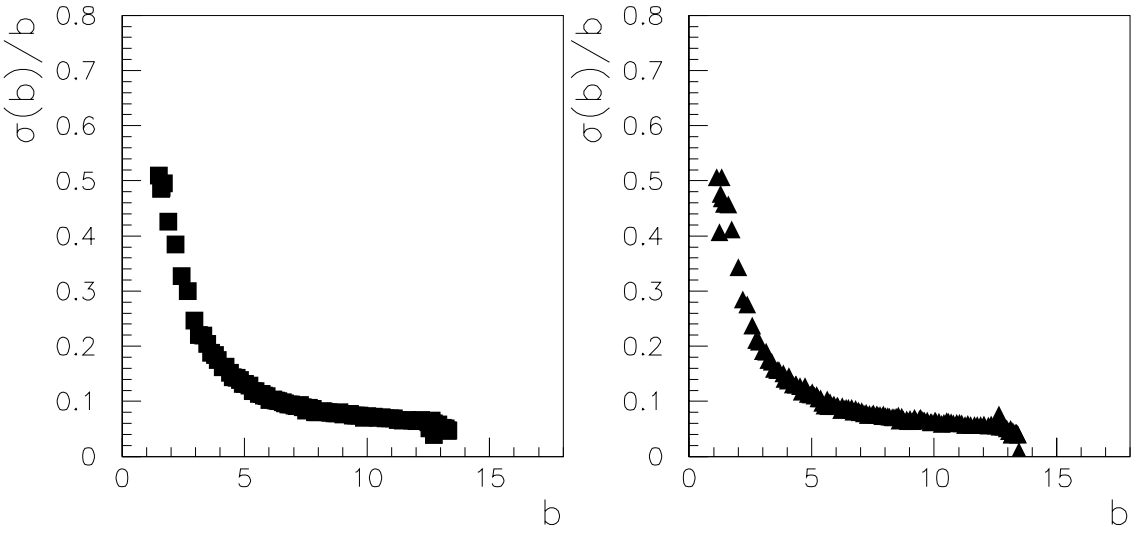

Figure 4.2: Resolution on the impact parameter from the measurement of spectator protons (left) or neutrons (right).

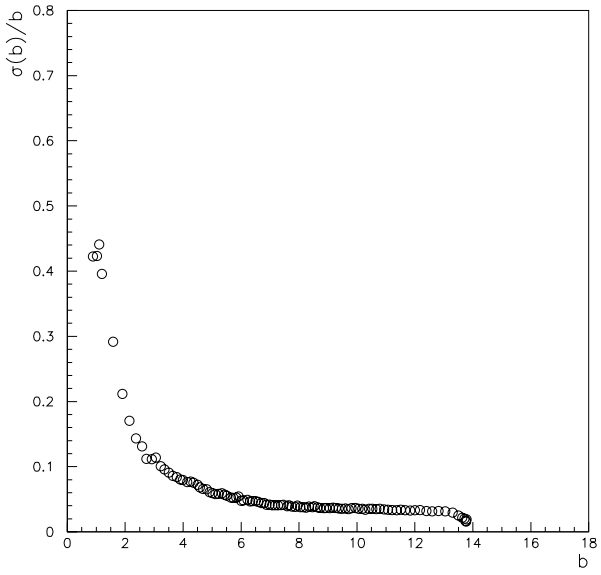

Figure 4.3: Resolution on the impact parameter by measuring spectator protons *and* neutrons for both colliding nuclei.

The fluctuations in the number of spectators can be reduced by measuring, as will be done in ALICE, the number of spectator protons and neutrons for *both* colliding nuclei, by means of the two sets of two ZDCs. This is shown in Fig. 4.3 where the resolution on the impact parameter for a simultaneous

measurement of spectator protons *and* neutrons for the two colliding nuclei is presented. Even for very central events ($b \sim 2$ fm) the resolution is excellent (about 0.4 fm).

4.3 Energy resolution of the detectors

The resolution on the measurement of the centrality depends not only on the fluctuations in the number of spectators (intrinsic resolution) but also on the precision we can achieve on their energy measurement. The resolution on the energy measurement of the spectators in the ZDCs at a certain centrality must be at most of the same order of magnitude as the intrinsic resolution we have at that centrality.

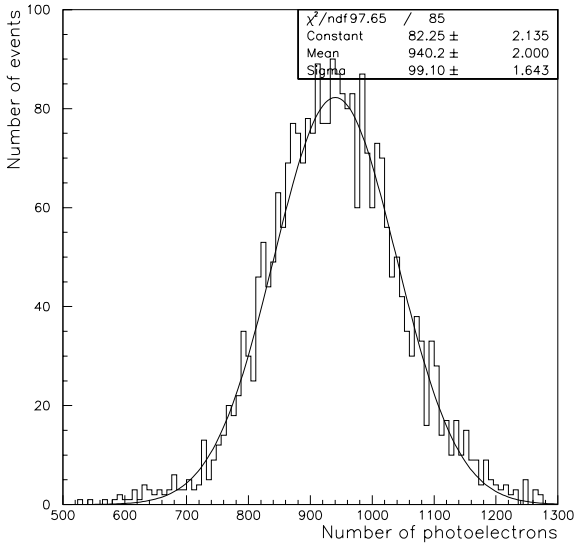

Figure 4.4: Resolution of the neutron calorimeter summing the response of all the PMTs.

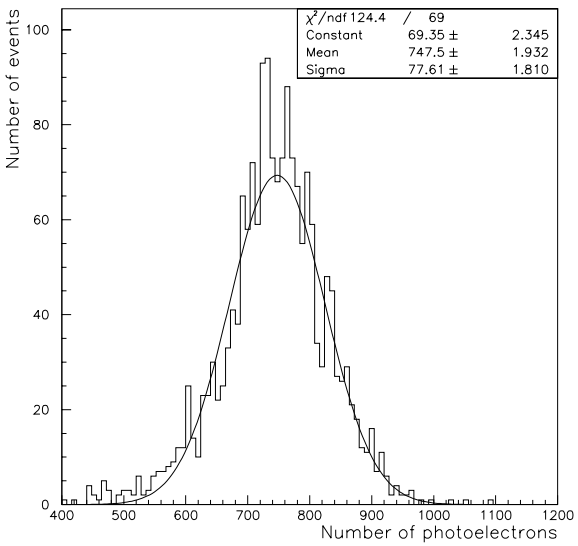

Figure 4.5: Resolution of the proton calorimeter summing the response of all the PMTs.

From the simulation of the ALICE ZDCs, described in Chapter 3, one obtains, for a single 2.7 TeV incident neutron on the neutron detector, the response shown in Fig. 4.4. The response of the proton calorimeter, for a 2.7 TeV incident proton, can be seen in Fig. 4.5. In the plots the photoelectron yield has been calculated as the sum of the responses of the five photomultipliers; the resolution of the neutron calorimeter turns out to be 10.5%, whilst for the proton calorimeter we obtain 10.3%.

The contribution from participant nucleons and secondary particles has been shown to be negligible (see Section 3.3.4 on page 46). Therefore the expected energy spread for N spectator nucleons, having the same incident energy (apart from the smearing caused by Fermi motion), can be approximated as

$$\sigma(E)_N = \sqrt{\Sigma_i \sigma(E)_i^2} = \sqrt{N}\sigma(E)_i \ .$$

Even for very central events the number of spectator nucleons is not negligible, leading to a quick decrease of $\sigma(E)/E$. For example, at $b = 2$ fm, where the total expected spectator yield for the two colliding nuclei is ~ 30, we obtain $\sigma_E/E = 1.8\%$.

4.3.1 Loss of spectator nucleons

The conclusions stated above are valid only if one assumes that *all* the spectator neutrons and protons produced at the IP are effectively seen by the ZDCs. Clearly, any loss of particles along the beam line will decrease the total energy incident on the calorimeters and therefore limit the achievable resolution. In Section 3.3.3 on page 44 we have seen that there is basically no loss of neutrons, as their emission cone

is quite narrow (of the order of 50 μrad at 1σ level). On the contrary, it has been shown in Section 3.3.1 on page 42 (see Fig. 3.8 on page 45) that the optics of the beam line distorts the emission cone of the protons and that in the region around D1 a loss of protons can be expected, depending on the aperture of the beam pipe. This effect must be properly taken into account in the calculation of the detector's response as a function of the centrality, as will be shown in the next section.

4.4 Centrality resolution

Knowing the relationship between b and the number of spectators (from VENUS), the response of the ZDCs with their resolution (from a GEANT simulation of the detectors), the loss of signal along the beam line (from a GEANT simulation of the insertion region), and taking into account the emission angle (100 μrad/beam) and the angular spread due to the beam divergency and to the Fermi motion of the nucleons, we have calculated the expected correlation between the energy measured by the ZDCs and the impact parameter. The results are shown in Fig. 4.6, separately for the proton calorimeter (a), the neutron calorimeter (b), the sum of the response of the two calorimeters (c), and for the whole set of ZDCs (i.e. on the two sides of the IP) (d).

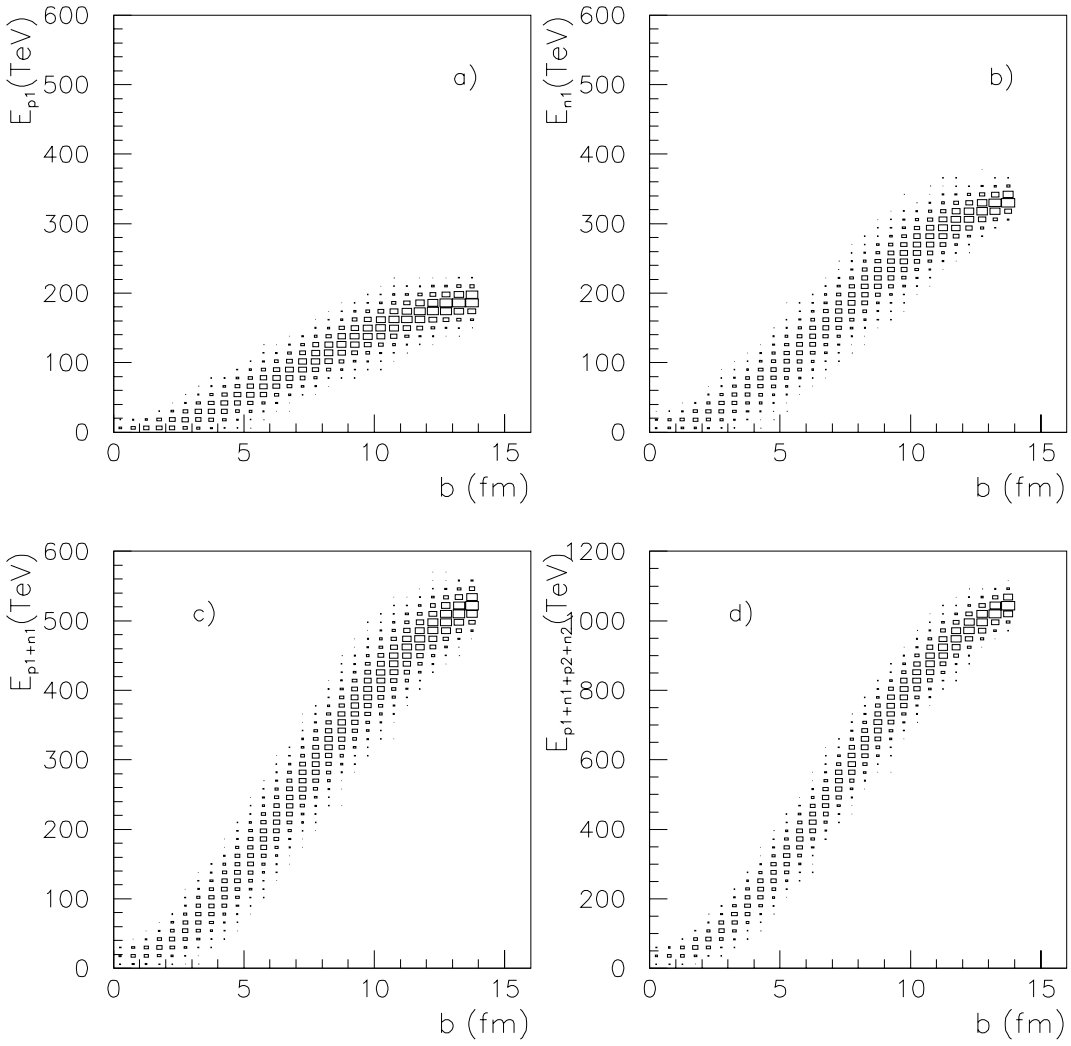

Figure 4.6: Correlation between the energy measured by the ZDCs and the impact parameter. E_{p1}, E_{p2} are the energies in each of the two proton ZDCs, E_{n1}, E_{n2} are the energies in each of the two neutron ZDCs.

Clearly, the correlation is narrower when we sum the signals over the whole set of ZDCs. This can be seen further in Fig. 4.7, which shows the resolution on the impact parameter for the four cases presented in Fig. 4.6.

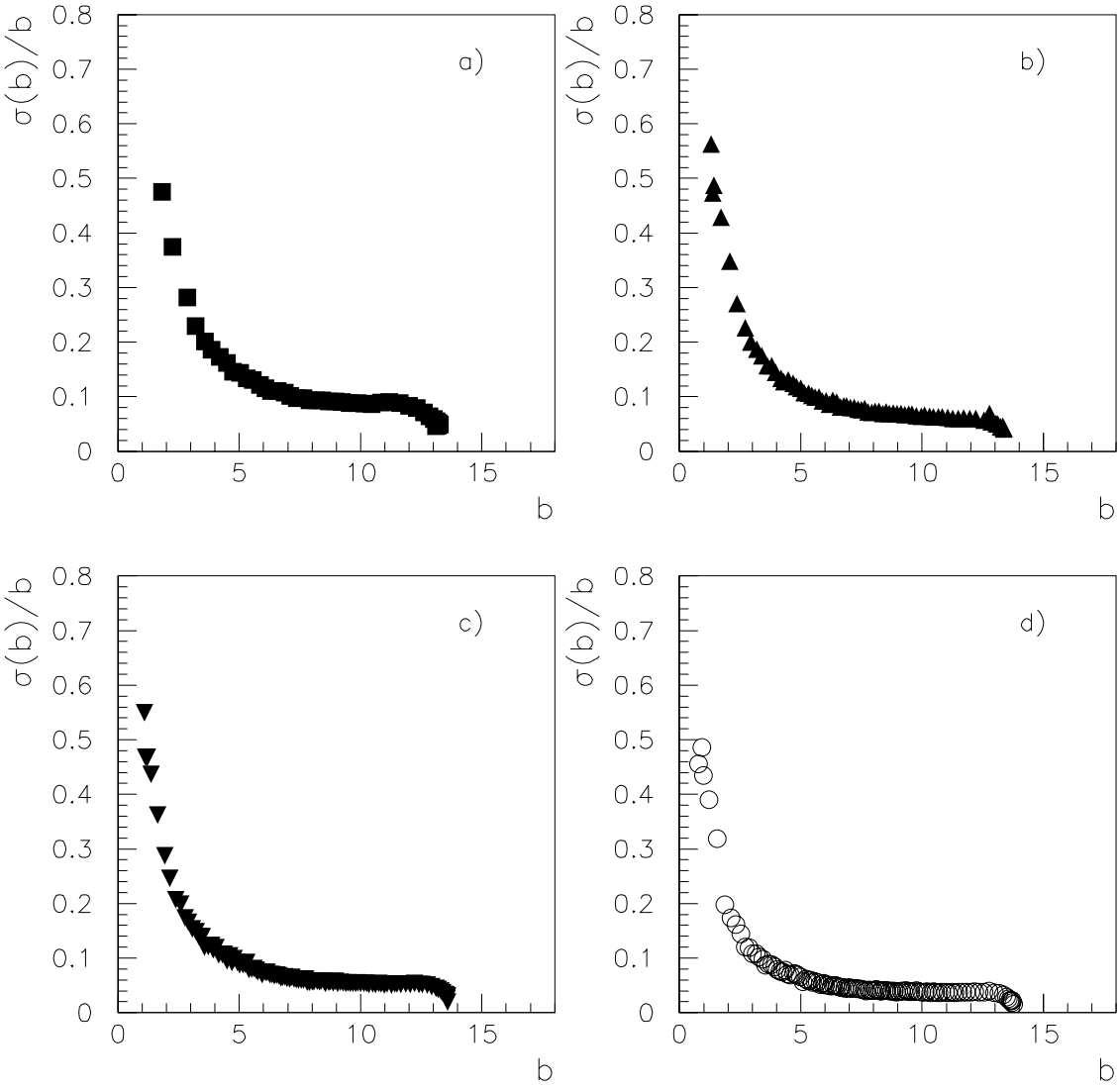

Figure 4.7: Resolution on the impact parameter for a measurement of spectator protons (a), neutrons (b), protons and neutrons (c), and protons and neutrons for the two colliding nuclei (d).

We conclude that the use of two sets of two ZDCs helps to reduce the fluctuations on the measurement of the centrality. It can also be noticed that the resolution on the impact parameter when all the experimental effects are taken into account (energy resolution, loss of spectators, etc.) does not differ significantly from the intrinsic resolution due to the fluctuations on the number of spectators at fixed impact parameter (compare Fig. 4.7(d) with Fig. 4.3). This means that the proposed design for the ALICE ZDCs ensures a precise and unbiased estimation of the centrality of the collision.

4.5 Identification of QGP signatures

Typically, in heavy-ion physics, an effect on some observables (such as strangeness enhancement or charmonia suppression), occurring in a certain centrality region, can be either explained as due to a phase

transition to a QGP or in the framework of a classical hadronic scenario. A phase transition is expected to lead to a threshold effect, i.e. to a sudden step in the observable as a function of the centrality; on the contrary a classical hadronic mechanism (reinteraction of secondaries, nuclear absorption, etc.) leads to an effect which is smeared over a certain centrality range. It is therefore quite important to achieve a good resolution on the centrality measurement in order to distinguish between the two scenarios.

As we have seen in the previous sections, the centrality resolution which can be obtained with ZDCs is well below 1 fm down to very central events (we have $\sigma_b \sim 0.4$ fm at $b = 2$ fm). We can hope to distinguish, at a certain value of b, the threshold-like signal caused by a phase transition from any smooth variation of a certain signature, provided that such variations occur over a b-interval larger than σ_b.

As an example we can suppose that for b = 5 fm we have a 50% drop of a certain quantity α (such as J/ψ cross-section), because of the onset of a phase transition. Taking into account the resolution on the impact parameter b obtainable with the ZDCs (see Fig. 4.7), we can calculate the evolution of the quantity α as a function of the *measured* value of the impact parameter $b_{\rm meas}$. On the other hand, we may suppose that a hadronic mechanism leads to the same decrease in α, but over a certain b range, of the order of 2 fm (i.e. larger than σ_b at $b = 5$ fm). Also, for this case, we calculate α as a function of $b_{\rm meas}$.

In Fig. 4.8(a) we show the two simulated behaviours as a function of b, whilst in Fig. 4.8(b) the expected smearing on the impact parameter determination has been introduced, assuming that the centrality is calculated by means of the complete set of four ZDCs. Even if the finite resolution on b introduces some smearing of the QGP-induced drop (solid line), we can still distinguish between the two scenarios.

Clearly, if for any reason the resolution on b becomes worse, the smearing of $b_{\rm meas}$ reduces the capability of distinguishing between the two situations. As an example, in Fig. 4.8(c) and Fig. 4.8(d) we plot α as a function of $b_{\rm meas}$, for the two scenarios, when we measure the centrality through the two neutron ZDCs (c) or only one of the proton ZDCs (d). Because of the larger smearing induced by the loss of resolution on b, it becomes increasingly difficult to distinguish between a sharp drop and a smooth decrease of the quantity α. Such a worsening of the impact parameter resolution could be induced, for example, by a severe loss of spectators in the elements of the beam line. It is therefore necessary to keep such effects under control as much as possible. They are caused, for example, by the collimators being too narrow along the beam line or by instabilities in the beam orbit, as pointed out in Section 3.3.1 on page 42.

4.6 Fragmentation

4.6.1 Physics remarks

As the energy carried by the fragments produced in the collision will not be detected by the ZDCs (see Section 3.3.2 on page 44), it is important to know how the fragment production depends on the impact parameter at LHC energies.

The problem of the production of fragments in nucleus–nucleus collisions has been studied by various experiments at different energies: at the Bevalac (about 1 A GeV) [1, 2], at SIS (between 0.1 and 1 A GeV) [3, 4], at AGS (about 10 A GeV) [5], at SPS (160 to 200 A GeV) [6–8].

Comparing the results of these experiments one finds that the cross-section for fragment production has a weak beam energy dependence and is strongly correlated with the geometry of the collision.

The dominant feature of the systematic study performed at SIS with the Aladin spectrometer [4] is the $Z_{\rm bound}$ universality that is obeyed by the fragment multiplicities and correlations, where $Z_{\rm bound}$ is the sum of the atomic number Z_i of all projectile fragments with $Z_i \geq 2$. In particular, the experiments at SIS have found that the number of intermediate mass fragments (with $3 \leq A \leq 30$), the charge distribution of the produced fragments, and the greatest charge of the fragments, do not depend either on the projectile energy or on the particular colliding system, when all the previous quantities are plotted against the variable $Z_{\rm bound}$.

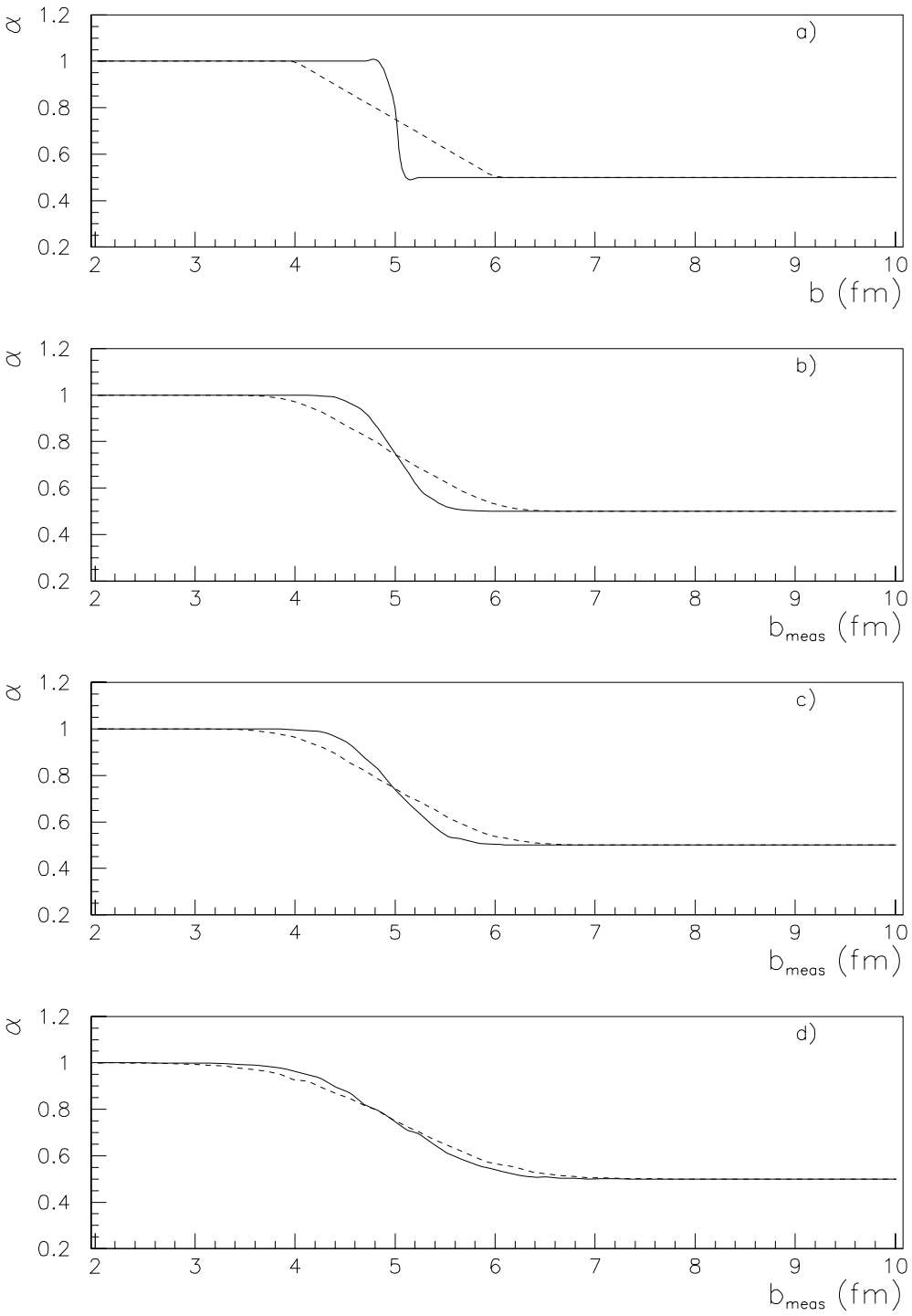

Figure 4.8: The effect of the finite resolution on the impact parameter b for a drop in a quantity α caused by a phase transition (solid line) or a hadronic mechanism (dashed line). In a) α is shown as a function of the true centrality, whilst in b), c) and d) the resolution on the impact parameter has been introduced. In (b) the centrality is measured using the whole set of calorimeters, in (c) only the signal from the two neutron ZDCs is considered, whilst in (d) only one of the proton ZDCs is supposed to be active.

As an example, Fig. 4.9 shows the mean multiplicity of intermediate mass fragments as a function of Z_{bound} for Au-Au collisions at various projectile energies. The fragment production turns out to be independent of the projectile energy within the experimental accuracy. The charge distribution of the produced fragments is found to follow a power law $dN/dZ = kZ^{-\tau}$; the exponent τ also depends on the variable Z_{bound}.

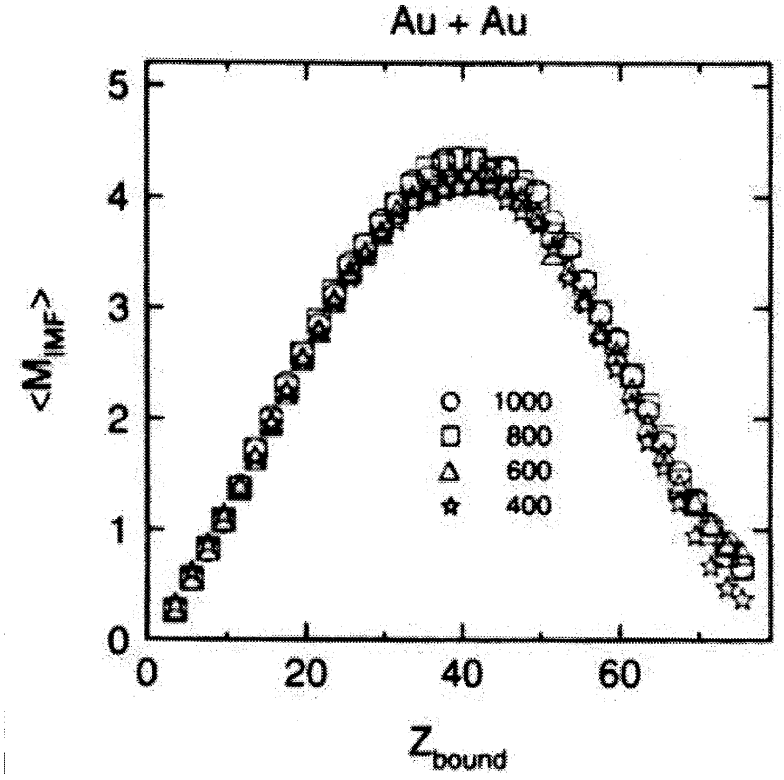

Figure 4.9: Mean number of intermediate mass fragment as a function of Z_{bound}.

Similar dependences of the mean multiplicities on Z_{bound} have been found in experiments with emulsion targets, both at AGS and at CERN energies (up to 160 GeV per nucleon). Therefore one can assume that the spectator formation and decay exhibit the same invariant features, even at the highest LHC bombarding energies.

4.6.2 Simulation

As the usual event generators do not consider fragment production, we have built a simple model to describe the nuclear fragmentation at LHC energies. The starting point is the evaluation of Z_{bound} from the impact parameter of the collision. Assuming that Z_{bound} is a monotonic function of the impact parameter [9], we can write:

$$\int_0^{Z_{\mathrm{bound}}} \frac{d\sigma}{dZ'_{\mathrm{bound}}} dZ'_{\mathrm{bound}} = \int_0^{b} \frac{d\sigma}{db'}\, db' \ ,$$

where b is the impact parameter, and the two integrals give the total nucleus–nucleus hadronic cross-section. As the differential cross-section $d\sigma/dZ_{\mathrm{bound}}$ is roughly constant [4], we can easily calculate Z_{bound} for a given value of the impact parameter. In Fig. 4.10 the quantity Z_{bound}, calculated in the framework of this simple model, is plotted as a function of the impact parameter.

The number of fragments, and their charge distribution as a function of Z_{bound}, have been obtained through a fit to the results of the Aladin experiment; the width of the distributions have also been taken into account. As an example, in Fig. 4.11 the mean number of fragments (left) and the greatest charge of

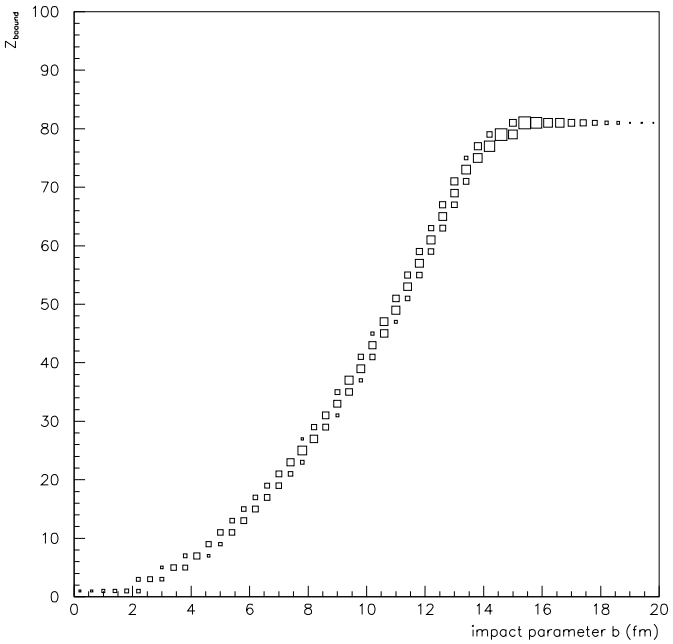

Figure 4.10: Z_{bound} as a function of the impact parameter.

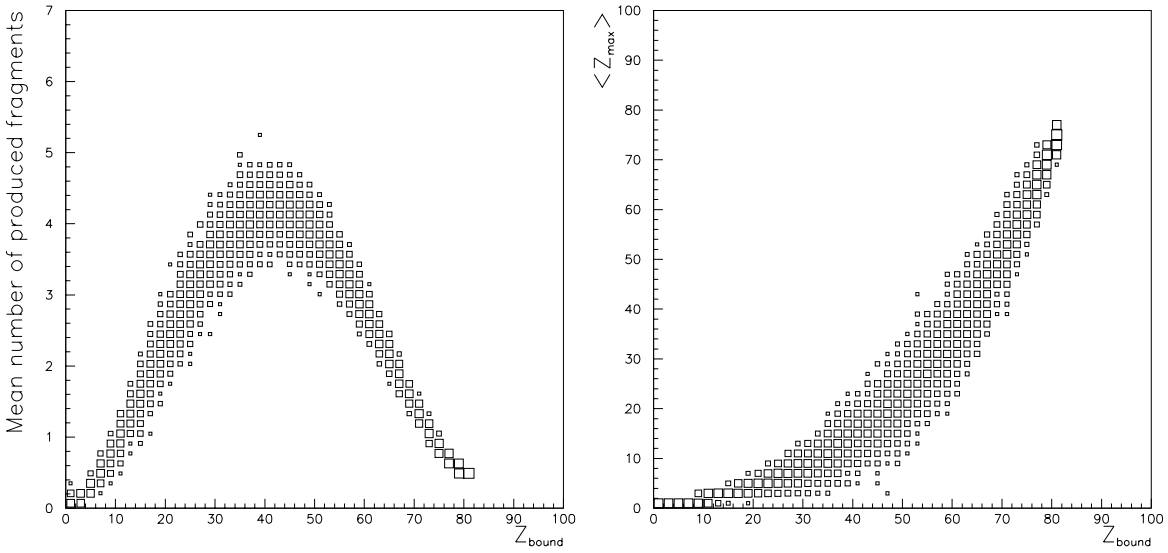

Figure 4.11: Mean number of fragments (left) and the greatest charge of the produced fragments (right) as a function of Z_{bound}.

the produced fragments (right) are shown as a function of Z_{bound}. As Z_{bound} depends quadratically on the impact parameter, the number of produced fragments is very small for central events; it increases up to a maximum for intermediate values of b and then decreases for peripheral events, where only one or two fragments are produced, with an atomic number Z close to that of the projectile.

Having fixed the number of fragments and their charge, a suitable number of neutrons is added to the chosen number of protons to form fragments, according to the GEANT list of stable nuclei. The momentum of the produced fragments and of the remaining free spectator nucleons (if any) is the beam momentum, smeared by the Fermi distribution. The spectator fragments and free nucleons are then tracked in the usual way through the LHC beam line up to the location of the ZDCs.

4.6.3 Results

When the fragmentation is considered, the monotonic correlation between the impact parameter and the sum of the energies detected by the four ZDCs is still visible up to $b \sim 11$ fm, whilst for very peripheral events it is partially destroyed, because of the large fragment yield (see Fig. 4.12). This fact could lead to a wrong assignment of the centrality of the collision for such events. The consequences in terms of trigger efficiency will be discussed in the next section.

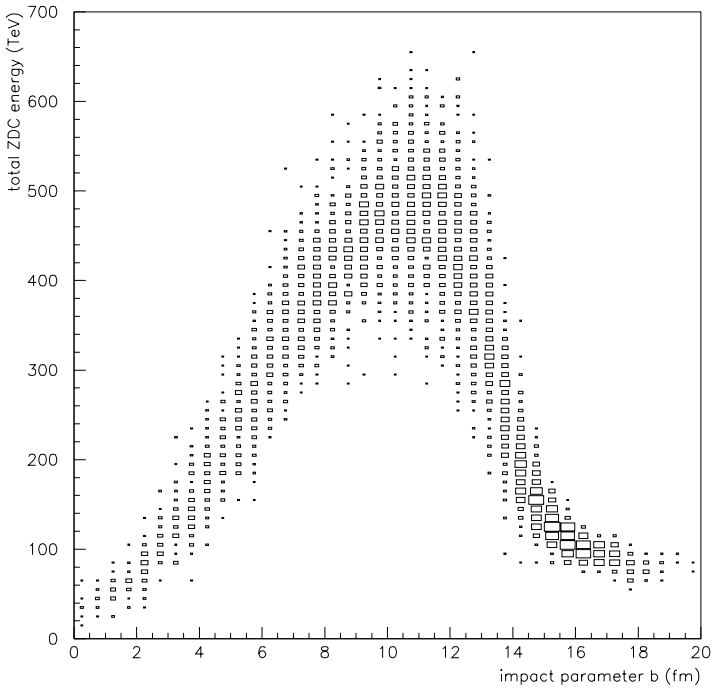

Figure 4.12: The total energy measured by the ZDCs as a function of the impact parameter.

Anyway, the most peripheral events are expected to be easily identified already by the level 0 trigger, which requires some minimum multiplicity in the Forward Multiplicity Detector (FMD). Another way to roughly identify very peripheral collisions is to use the e.m. calorimeters described in Section 3.6 on page 55. As these detectors are placed outside the emission cone of the spectators, the energy detected in such calorimeters, mainly due to participants emitted at large rapidity, is anti-correlated with the impact parameter, as can be seen in Fig. 4.13.

4.7 Trigger efficiency

In the logic of the level 1 trigger it will be possible to have several centrality intervals, selecting different ZDC energy thresholds. The effect of a cut on the total ZDC energy in terms of the impact parameter is shown in Fig. 4.14, where four different thresholds have been implemented. Figure 4.15 shows the efficiency of the centrality trigger for the selected energy thresholds. The centrality intervals appear to be defined within $\Delta b \sim 1$ fm.

With an energy cut around 300 TeV, it is possible to select about 10% of the minimum bias Pb-Pb cross-section. When fragment production is taken into account, as described in the previous section, with the same energy cut we also accept some very peripheral events, as can be seen in Fig. 4.16.

The resulting bias introduced in the trigger can be substantially removed, identifying the central events by an appropriate threshold on the total energy detected by the two e.m. calorimeters. By requiring

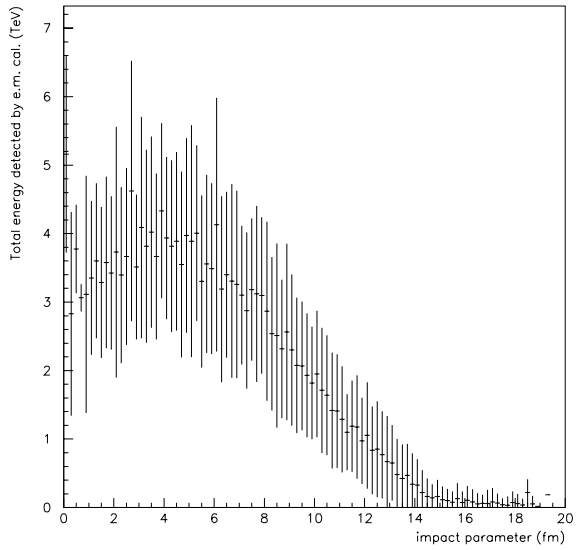

Figure 4.13: Total energy detected by the two e.m. calorimeters, one on each side of the IP, as a function of the impact parameter.

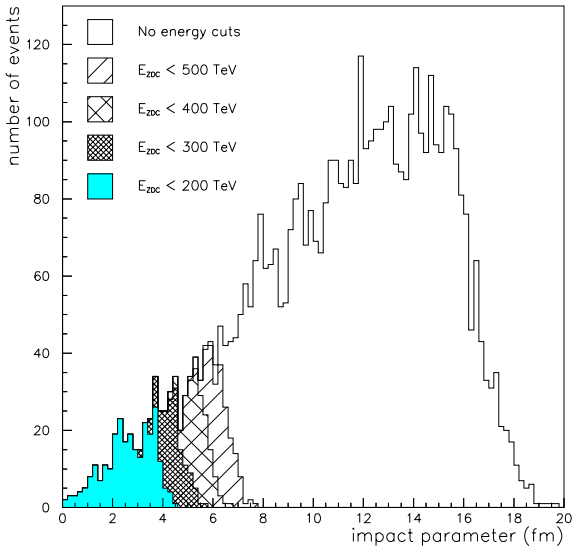

Figure 4.14: Impact parameter distribution for events satisfying different zero degree energy cuts.

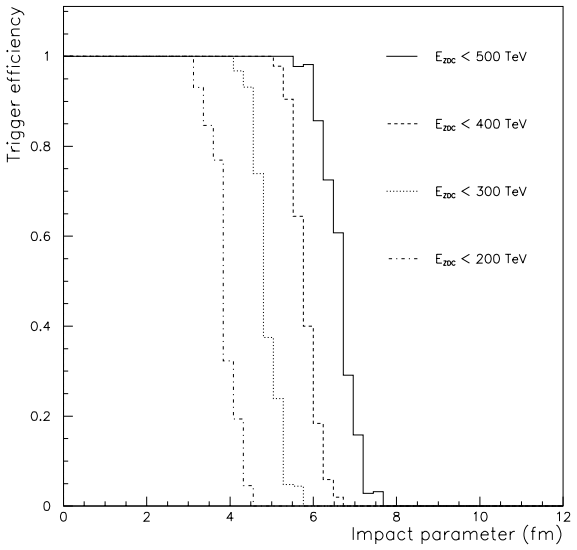

Figure 4.15: Efficiency of the centrality trigger for four different ZDC energy thresholds.

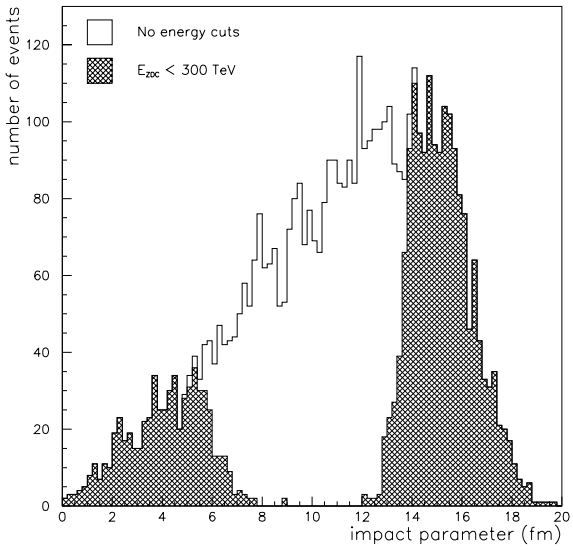

Figure 4.16: Events selected by a 300 TeV energy cut on the ZDCs, when the fragmentation model of Section 4.6 is considered.

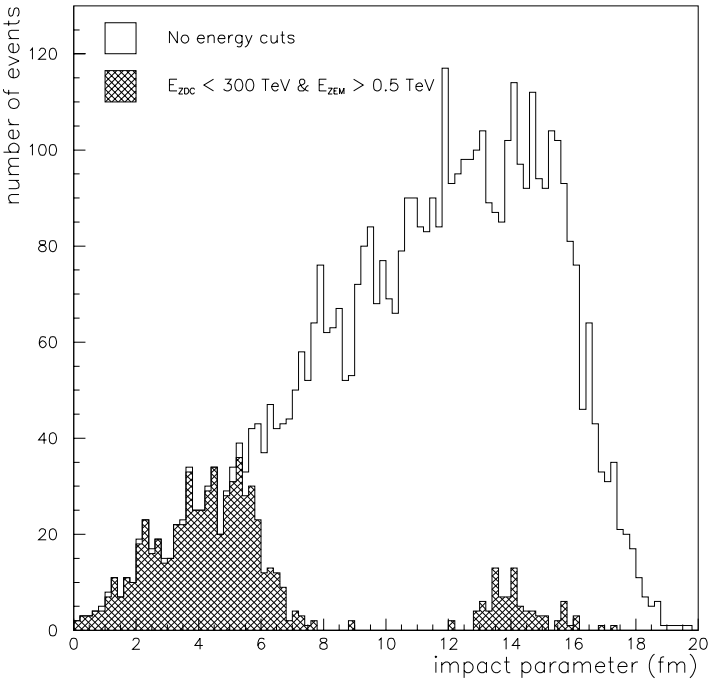

Figure 4.17: Events selected by a 300 TeV energy cut on the ZDCs, after applying a 0.5 TeV energy cut on the e.m. calorimeters.

an e.m. total energy $E_{ZEM} \geq 0.5$ TeV, the contamination due to peripheral events drops by a factor of ~ 20, with a loss of efficiency for central events of only $\sim 2\%$ (see Fig. 4.17).

Anyway, it must be stressed that the level 0 trigger should already remove the most peripheral events, thereby cleaning the event sample given to level 1.

4.8 The ZDC as a luminosity monitor

4.8.1 Introduction

During operation with heavy-ion beams, the LHC luminosity can be measured and monitored by means of the ZDCs. The basic idea is to measure the rate of mutual electromagnetic dissociation in the neutron channel. In this process, the Giant Dipole Resonance (GDR) is excited for both of the colliding nuclei by a virtual photon radiated by the partner nucleus. Since the GDR decays mainly by emitting one neutron, the process can be identified by detecting simultaneously one neutron in each of the neutron calorimeters placed on both sides of the interaction point. The measured rate dN^m/dt of mutual e.m. dissociations in the neutron channel is proportional to the luminosity L:

$$dN^m/dt = L \cdot \sigma^m \ . \tag{4.1}$$

Therefore, the luminosity can be immediately deduced if we know the cross-section for mutual e.m. dissociation in the neutron channel, σ^m.

The choice of this reaction for the luminosity measurement is driven by two considerations [10]. On the one hand the cross-section σ^m can be computed with reasonable accuracy, as will be discussed in the next section. On the other hand, this reaction is relatively background free and can be detected with full acceptance, implying a rather precise measurement of the reaction rate. These experimental aspects will be discussed in Section 4.8.3.

4.8.2 Mutual dissociation cross-section

When two nuclei A and B collide at impact parameter b larger than the sum of the nuclear radii, the interaction is purely electromagnetic. At ultrarelativistic energies, each nucleus experiences the strongly Lorentz-contracted Coulomb field of the other nucleus. According to the Weizsacker–Williams (WW) method, this can be expressed in terms of the equivalent photon spectrum $n_B(\omega, b)$, where ω is the energy of the virtual photon. The interaction with nucleus A of a virtual photon (radiated by nucleus B) may lead to its dissociation in the single neutron channel and, at first order, the cross-section for this process is given by

$$\sigma_A^{1n} = \int_{b \geq b_{\min}} 2\pi b\, db \int n_B(\omega, b)\, \sigma_A^{\gamma,1n}(\omega)\, d\omega \,, \tag{4.2}$$

where $\sigma_A^{\gamma,1n}$ is the cross-section for single-neutron production in the $\gamma - A$ interaction. The expression of $n_B(\omega, b)$ can be derived in the framework of classic electromagnetism [11]. It can be shown [12] that for a given impact parameter b the virtual photon spectrum scales as $1/\omega$ for $\omega \ll \omega_{\rm cut}(b)$ and then quickly vanishes for $\omega \gg \omega_{\rm cut}(b)$, where $\omega_{\rm cut}(b) = \gamma/b$ and γ is the Lorentz factor in the rest frame of nucleus A. The cutoff energy $\omega_{\rm cut}(b)$ increases when b decreases and for impact parameters close to the sum of the nuclear radii turns out to be $\omega_{\rm cut}(b) \sim 10^5$ GeV at LHC energies [12]. The electromagnetic dissociation in the neutron channel (the reaction we are interested in) is induced by low-energy photons. In fact, as previously stated, this process occurs via the excitation and subsequent decay of the GDR which, for Pb, lies in the energy range $6 \leq \omega \leq 30$ MeV.

Indeed, Eq. (4.2) represents the lowest-order approximation of the cross-section, and at extremely high colliding energies, higher orders have to be taken into account. The details of these calculations can be found in Ref. [10]; the main points are outlined here. For this purpose, it is worth rewriting Eq. (4.2) as

$$\sigma_A^{1n} = \int_{b \geq b_{\min}} 2\pi b\, db\, \bar{n}_A^{1n}(b) \,, \tag{4.3}$$

where

$$\bar{n}_A^{1n}(b) = \int n_B(\omega, b)\, \sigma_A^{\gamma,1n}(\omega)\, d\omega \tag{4.4}$$

represents the mean number of e.m. dissociations in the one neutron channel for a given impact parameter b. As we are interested in those events where one and only one neutron is emitted, we have to evaluate the probability P_A^{1n} for such a process. Using a Poisson distribution with mean value $\bar{n}_A^{1n}(b)$, this is given by:

$$P_A^{1n}(b) = \bar{n}_A^{1n}(b) \cdot \exp[-\bar{n}_A^{1n}(b)] \ . \tag{4.5}$$

Equation (4.5) is still an approximate expression. In fact, there are two effects that have to be taken into account in computing P_A^{1n}. The first is that, as previously mentioned, a large number of virtual photons of energy higher than the value needed to excite the GDR is radiated. As the interaction of these photons with nucleus A leads to higher excitation energies, the emission of one and only one neutron occurs if no energetic photon interacts with the nucleus in addition to the low-energy one. The second point concerns the effect of nuclear interactions. Because of the tails of the nuclear density distribution, nuclear interactions have a non-vanishing probability to occur even for impact parameters larger than the sum of the mean nuclear radii (we note that this introduces some incertitude on the value of $b_{\min}$ to be used as input of Eq. (4.2) and Eq. (4.3)). However, as for high-energy photons, in nuclear interactions a high excitation energy is transferred to nucleus A, which has a small probability to decay by emitting a single neutron with momentum close to the beam momentum. Therefore, the process we are interested in only takes place if the colliding nuclei do not undergo nuclear interactions.

With these two additional requirements, the probability for the emission of one and only one neutron becomes:

$$P_A^{1n}(b) = \bar{n}_A^{1n}(b) \cdot \exp[-\bar{n}_A^C(b) - \bar{n}_A^N(b)] \ , \tag{4.6}$$

where $\bar{n}_A^C(b)$ and $\bar{n}_A^N(b)$ are, respectively, the mean number of Coulomb and nuclear dissociations for a given impact parameter b. The former can be computed by replacing in Eq. (4.4) the photo-neutron cross-section $\sigma_A^{\gamma,1n}$ with the total photoabsorption cross-section σ_A^{γ} for nucleus A; the latter can be evaluated in the framework of the Glauber model.

The cross-section for e.m. dissociation of nucleus A in the single-neutron channel can be obtained by replacing in Eq. (4.3) $\bar{n}_A^{1n}(b)$ the probability $P_A^{1n}(b)$ given by Eq. (4.6). It should be noted that the exponential factor $\exp[-\bar{n}_A^C(b) - \bar{n}_A^N(b)]$ provides a natural impact parameter cutoff, since both $\bar{n}_A^C(b)$ and $\bar{n}_A^N(b)$ become large when b approaches the sum of the mean nuclear radii. Therefore, the single-neutron cross-section σ_A^{1n} given by Eq. (4.3) is not sensitive to the incertitude on the value of $b_{\min}$ needed to carry out the integration. The calculation of the single-neutron Coulomb dissociation for Pb-Pb collisions at the LHC energy gives σ_{Pb}^{1n} = 105.9 b. This value turns out to be independent from the choice of the nuclear density distribution parameters, within a few per mil.

For symmetric colliding systems ($A = B$), the probability for mutual Coulomb dissociation in the single-neutron channel for a given b is given by the square of $P_A^{1n}(b)$:

$$P_A^{m}(b) = (\bar{n}_A^{1n}(b) \cdot \exp[-\bar{n}_A^C(b) - \bar{n}_A^N(b)])^2 \ . \tag{4.7}$$

The cross-section for mutual dissociation in the single-neutron channel can be evaluated by entering $P_A^m(b)$ in Eq. (4.4). For Pb-Pb interactions at the LHC, the cross-section for mutual Coulomb dissociation in the one neutron channel turns out to be σ_{Pb}^m = 0.535 b. Again, the dependence of this value on the parameters of the nuclear density distribution is weak, less than 1%.

4.8.3 Experimental considerations

From the experimental point of view, the first relevant feature of the process that we propose to study for measuring the luminosity is that all the emitted neutrons fall in the acceptance covered by the neutron ZDC. This implies that no correction of the measured rates is needed to account for the experimental acceptance. In fact, simple kinematic considerations show that the transverse momentum of the neutrons produced in the decay of the GDR is below 250 MeV/c. This means that all these neutrons are emitted at angles smaller than 0.1 mrad in the laboratory system, corresponding to a ~ 1 cm radius spot on the front face of the neutron calorimeters.

A simple simulation shows that the energy of the single-neutrons from GDR decay ranges from 2.1 to 3.4 TeV, in the laboratory system, the most probable value corresponding to the energy per nucleon of the beam. In reality, the shape of the energy distribution (but not the extreme values) depends on the neutron angular distribution in the frame where the excited nucleus is at rest. In our calculations an isotropic angular distribution was assumed. The width of the single-neutron energy distribution is small enough to allow a clear separation between the events in which one neutron is emitted (the ones we are interested in) and those where two or more neutrons are emitted in the GDR decay. This can be seen in Fig. 4.18, where the expected ZDC energy distribution is shown. Note that the ZDC energy resolution is included in the calculation and the ratios between the numbers of one, two and three neutron events are taken from Ref. [13].

The two aspects discussed in this section hold for both single and mutual dissociation in the one-neutron channel. For luminosity measurements, the second reaction presents the additional advantage of having a smaller background. In fact, the coincidence measurement avoids the contamination caused by single-neutron emission from beam–gas interactions. It should be noted, however, that even for the single dissociation process such a background is not expected to be large, for two reasons. The first

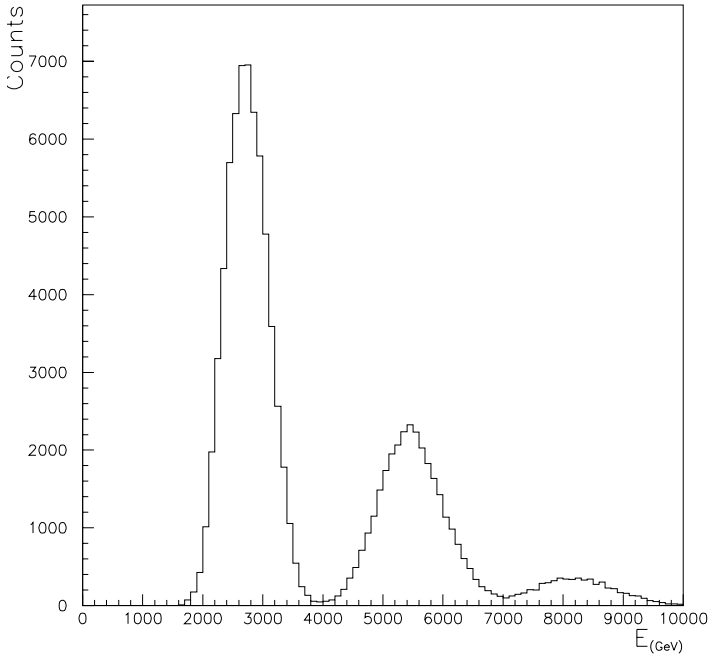

Figure 4.18: Expected energy distribution of neutrons from e.m. excitation of the giant dipole resonance. The ZDC energy resolution is included in the calculation.

is that the residual gas in the beam pipes is mainly made of light elements, and the cross-sections for Coulomb dissociation scales as Z^2 [10, 12]. The second is that for beam–gas interactions the Lorentz γ factor is much smaller than for beam–beam interactions, leading to a softer photon spectrum and a smaller Coulomb cross-section.

5 Installation and organization

5.1 Installation and experimental environment for the ZDC detector

The LHC layout includes a 50 m long section between the dipole magnets D1 and D2, where the common beam channel in the experimental insertion and low-beta section is separated into two beam channels before entering the D2 magnet. At Point 2 this section starts at 68 m distance from the intersection point. When LHC is operating with heavy ions, the D1 magnet will deflect all lighter ions produced in the interaction region, and separate them from the ion beam. Neutral particles will follow the bisector of the two ion beams. The best position of the ZDC detector modules are therefore as close as possible to the entrance of the D2 magnet, where the neutral detector module can be installed in between the two beam channels, and the positive (and negative) detector modules can be installed close to the outside of the beam channels.

In order to achieve this and to minimize the material in front of the ZDC detector modules, the two beam channels are combined into a common vacuum chamber and separated into two vacuum chambers only just before the entrance to the D2 magnet, leaving sufficient space for the ZDC modules (see Fig. 5.1).

Because of possible beam losses during LHC injection operations, retractable collimators (TDI) must be placed at about 5 m distance from D1. This installation is only necessary on the injection left side of Intersection Point 2. If the collimator blocks were made to retract by 135 mm, they would not obscure the aperture for the ZDC detector (as indicated in Chapter 3). A first feasibility study [1] shows that this is possible. The ZDC modules are placed on a table, which can be lowered during injection (see Fig. 5.2). The modules will be at a distance of about 5 mm from the vacuum chamber, and interlocks will be installed in order to avoid any collision with the beam elements during the movements of the scissors table. The table and detector do not protrude into the tunnel and the physical extension of the complete detector is contained within the diameter of the D2 magnet.

The integration of the ZDC in the LHC tunnel has been discussed [2] and a principal agreement of the proposed layout has been reached.

The vacuum chamber is made of cylindrical sections, joined by conical sections. A number of pumps will be placed outside the detection aperture of the ZDC detector. The vacuum chamber is terminated by a thin window having a thickness of about 2 mm of stainless steel. The RF losses for this vacuum chamber have been estimated and are not a course for concern[1].

The maintenance access to the detector will be limited to the frequency of access given to this part of the Point 2 straight section. This is not considered as a serious limitation. Similar detectors have operated in the NA50 environment during long no-access periods ($\sim$ 3 years with one month/year high intensity lead runs).

5.2 Safety aspects

The installation of the ZDC detector must be regarded as trivial and the small size, weight, and total absence of gases or liquids provide for an intrisincally safe installation. All insulation materials will

[1] The integration of the ZDC detector into the LHC lattice has been presented and discussed with the LHC management and only a preliminary agreement has been reached concerning the layout and interference with the machine, as described in this report. It is clear that the final integration of the ZDC detector will depend on the evolution of the LHC lattice and more detailed studies of the beam line between the D1 and D2 magnets.

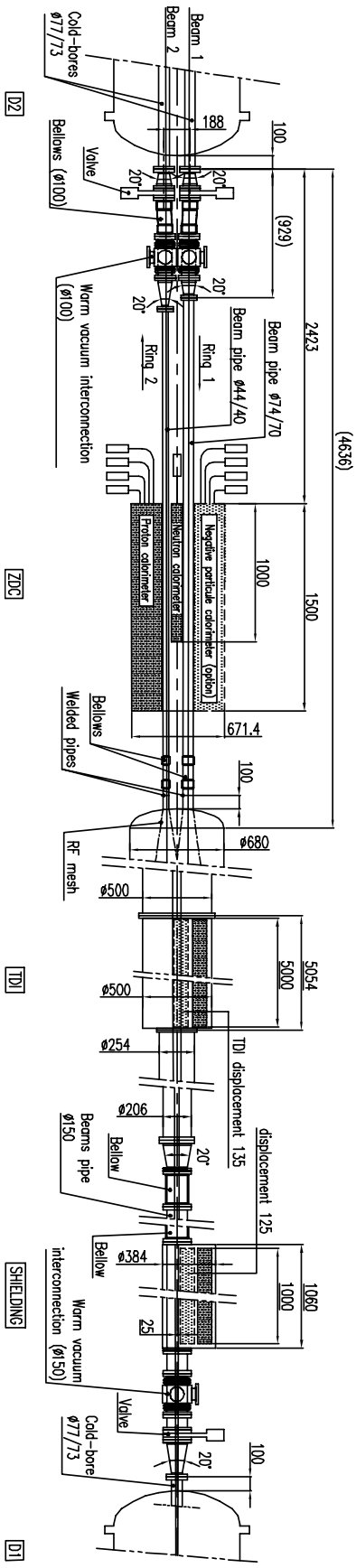

Figure 5.1: General layout of the LHC beam line at the position of the ZDC detector at Point 2.

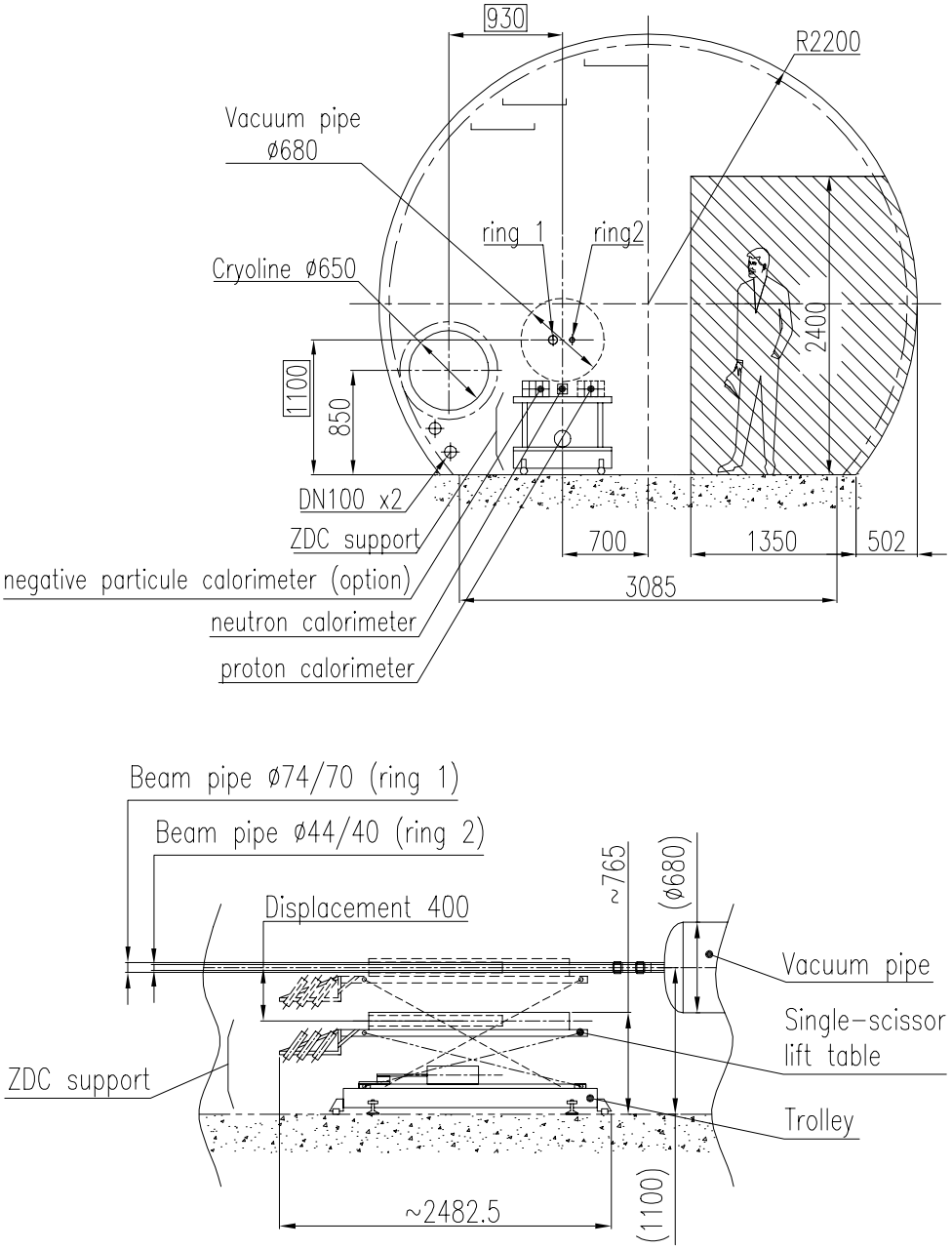

Figure 5.2: The ZDC detector supported by a movable table inside the LHC tunnel.

conform with the CERN Safety Instruction TIS IS41 (The use of plastic and other non-metallic materials at CERN with respect to fire safety and radiation resistance).

5.3 Services

The detector will require about 50 cables to be installed along the LHC tunnel all the way to the Alice counting room placed in the PX 24 access shaft at Point 2. The total length of these cables is 211 m on one side of the IP and 311 m on the other side. The detector will not require any special cooling.

5.4 Slow control

The Alice detector control system is specified in Ref. [3]. The signals to be measured for the ZDC detector are listed in Table 5.1.

Table 5.1: Main parameters of the detector control system for the ZDC detector.

System	Location	Controlled parameter	Number	Type	Parameters	Control
HV	PX24	PMT voltage	50	Analog	Voltage	ReadWrite
	PX24	PMT current	50	Analog	Current	Read
	PX24	PMT current limits	50	Analog	Threshold	ReadWrite
	PX24	PMT ramp up/down	50	Analog	Voltage	ReadWrite

5.5 Milestones and construction programme

An overall time schedule for the ZDC construction programme is shown in Fig. 5.3.

During 1999 we expect to finalize the calorimeter design, following the results of the prototype beam tests and the inquiry about the availability of the high-density absorber. Concerning the quartz fibres two possible scenarios are being considered, depending on the INFN budget allocations:

- a unique tender for all fibres in the year 2000 (this will save on the total cost),
- a first order for the fibres of the ZN calorimeters in the year 2000 and a second one in the year 2001 for the fibres of the ZP and e.m. calorimeters.

In any case, the construction of the first ZN calorimeter is not foreseen to start before the end of the year 2000. The years 2001–2003 will be devoted to construction and tests.

The estimated time for the construction and assembly is five months for each of the hadronic calorimeters and two months for each e.m. calorimeter. This activity is foreseen to be performed by engineers and technicians of Cagliari and Torino Laboratories. For the ZN, the machining of the passive material sheets could be done by the company selected to provide the material; an additional period of four months for each ZN should be accounted for this job.

Figure 5.3 is based on the following milestones:

- 1999:
  continuing beam tests on prototypes and offline tests on photodetectors
- 2000:
  order of quartz fibres for the two ZNs
  order of passive material for the two ZNs

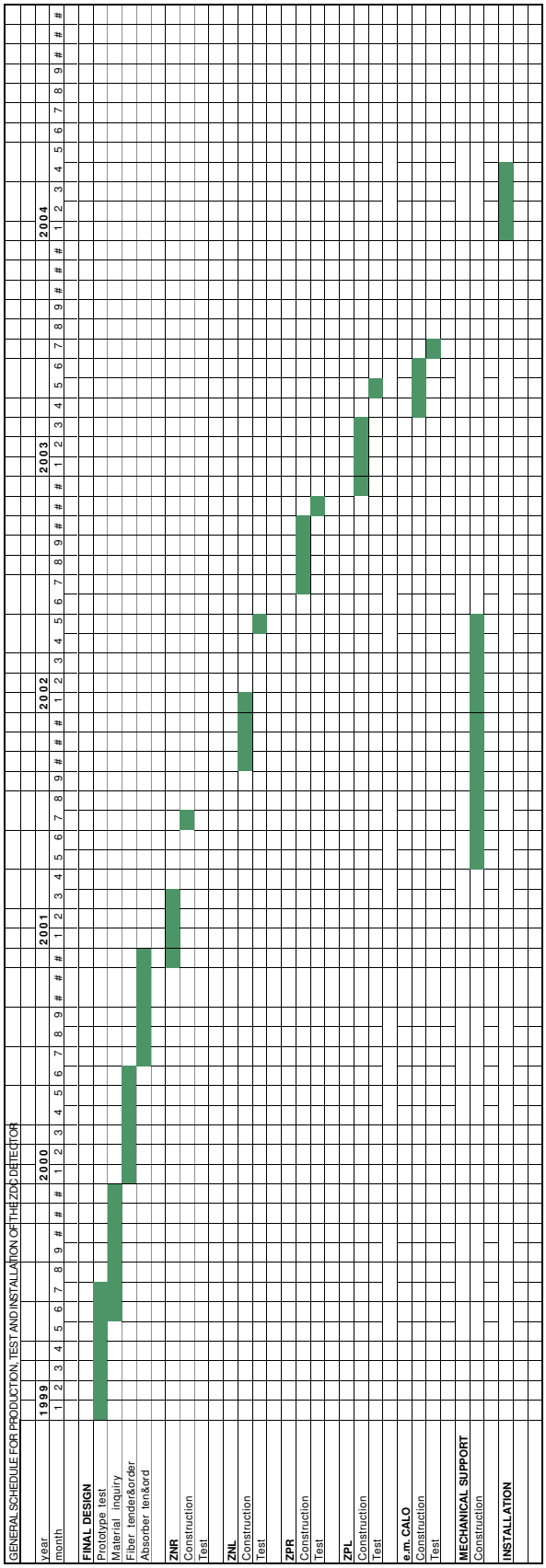

Figure 5.3: General schedule for production, testing and installation of the ZDC detectors.

order of passive material for the ZP and e.m. calorimeters
start construction of the first ZN

- end 2001:
  end of construction and test of one ZN
  beginning of construction of the second ZN
  order of quartz fibres for the ZP and e.m. calorimeters
  (there is the possibility of ordering all the quartz fibres together in the year 2000, in which case the schedule becomes more flexible)
- middle 2002:
  end of construction and test of the second ZN
  beginning of construction of the two ZP and of the e.m. calorimeters
- end 2003:
  all detectors ready for installation

The final installation of the ZDC modules in the LHC tunnel will depend on the LHC installation schedule.

5.6 Organization

The following institutes will share the fabrication and commissioning of the ZDCs:

- Università del Piemonte Orientale 'A. Avogadro', Alessandria, and INFN Torino, Italy.
- INFN, Sez. Cagliari and Dipartimento di Fisica, University of Cagliari, Cagliari, Italy.
- INFN, Sez. Torino and Dipartimento di Fisica, University of Torino, Torino, Italy.

In the design, construction and testing, the following ALICE members have participated:

- Università del Piemonte Orientale 'A. Avogadro', Alessandria, and INFN Torino, Italy.
  G. Dellacasa, E. Scalas.
- INFN, Sez. Cagliari and Dipartimento di Fisica, University of Cagliari, Cagliari, Italy.
  C. Cicalo, A. De Falco, M. Macciotta-Serpi, A. Masoni, G. Puddu, S. Serci, E. Siddi and G. Usai.
- INFN, Sez. Torino and Dipartimento di Fisica, University of Torino, Torino, Italy.
  R. Arnaldi, E. Chiavassa, P. Cortese, N. De Marco, M. Gallio, P. Mereu, A. Musso, A. Piccotti, E. Scomparin and E. Vercellin.

In addition, the following people have provided considerable help in specific sections of this Technical Design Report: F. Carminati, L. Leistam, C. Lourenço, A. Morsch, P. Vande Vyvre.

5.7 Responsibilities

The proposed sharing of responsibilities in the construction and operation of the ZDCs is presented in Table 5.2.

The institutes will jointly participate in the testing activities and related data analysis.

5.8 Cost estimate and resources

Table 5.3 reports the cost evaluation for the two sets of ZDCs. The manpower from participating institutes is estimated to ~ 35 man years.

Table 5.2: Sharing of responsibilities.

Institution	Responsibilities
INFN Torino and	On-line software and off-line analysis (part)
Univ. Torino and	Readout electronics and auxiliary equipment (part)
Univ. Alessandria	Mechanical work
	Calorimeter modules (part)
INFN Cagliari and	On-line software and off-line analysis (part)
Univ. Cagliari	Readout electronics and auxiliary equipment (part)
	Calorimeter modules (part)

Table 5.3: Cost evaluation.

Items	Cost [kCHF]
Absorbers	252
Fibres	340
Readout and electronics	216
Monitoring	82
Cables	68
Calibration	50
Mechanics	40
Total	1048

References

Chapter 1

[1] ALICE Collaboration, Technical Proposal, CERN/LHCC 95–71.
[2] R.J. Glauber, in Lectures in Theoretical Physics, edited by W.E. Brittin and L.G. Dunham (Interscience, N.Y., 1959), Vol. 1, p. 315.
[3] K. Werner, Phys. Rep. **232** (1993) 87.
[4] R. Arnaldi et al., NIM **A411** (1998) 1.
[5] C. de Marzo et al., NIM **217** (1983) 405.
[6] G.R. Young et al., NIM **A279** (1989) 503.
[7] GEANT 3.21, CERN Program Library Long Writeup W5013.
[8] X.N. Wang and M. Gyulassy, Phys. Rev. **D44** (1991) 3501.
[9] A. Schttauf et al. (ALADIN collaboration), Nucl. Phys. **A607** (1996) 457.
[10] H. Appelshauser et al. (NA49 collaboration), Eur. Phys. J. **A2** (1998) 383.
[11] A.J. Baltz et al., NIM **A417** (1998) 1.
[12] See Zero Degree Calorimeter for RHIC, at http://www.rhic.bnl.gov/∼swhite/zcal/proposal.ps

Chapter 2

[1] P. Gorodetzky et al., Proc. Fourth Int. Conf. on Calorimetry in High Energy Physics (World Scientific, Singapore, 1994) 433.
[2] P. Gorodetzky et al., Proc. Fourth Int. Conf. on Calorimetry in High Energy Physics (World Scientific, Singapore, 1994) 462.
[3] A. Musso et al., Proc. Fourth Int. Conf. on Calorimetry in High Energy Physics (Word Scientific, Singapore, 1994) 457.
[4] A. Contin et al., CERN/DRDC/94–4, January 5, 1994.
[5] G. Anzivino et al., NIM **A357** (1995) 380.
[6] A. Contin et al., NIM **A357** (1995) 369.
[7] P. Gorodetzky et al., NIM **A361** (1995) 161.
[8] P. Gorodetzky et al., Radiation Physics and Chemistry (Pergamon Press, Oxford, 1992) 41 (1992) 253.
[9] http://www.cern.ch/alice/Projects/offline/Simulation/galice/Manual.html
[10] H.C. Fesefeldt, Technical Report PITHA 85–02, III Physikalisches Institut, RWTH Aachen Physikzentrum.
[11] A. Caldwell et al., NIM **A330** (1993) 389.
[12] R. Arnaldi et al., NIM **A411** (1998) 1.
[13] C.R. Kerns, IEEE Trans. Nucl. Sci. **NS24** (1997) 353.
[14] M. Lundin et al., NIM **A372** (1996) 359–367.

Chapter 3

[1] A. Shor et al., Nucl. Phys. **A514** (1990) 717.
[2] A. Schttauf et al. (ALADIN collaboration), Nucl. Phys. **A607** (1996) 457.
[3] S. Weisz, private communication.
[4] O. Ganel et al., NIM **A365** (1995) 104.

[5] See for instance 'Photomultipliers data handbook', Philips Components PC04 – 1990.
[6] C.R. Kerns, IEEE Trans. Nucl. Sci. **24** (1977) 353.
[7] J.M. Dieulot et al., NIM **A314** (1992) 185.
[8] G. Rubin and J. Sulyan, Internal Note ALICE 97–14.
[9] O.Villalobos et al., Internal Note ALICE 98–23.

Chapter 4

[1] D.L. Olson et al., Phys. Rev. **C28** (1983) 1602.
[2] W.B. Christie et al., Phys. Rev. **C48** (1996) 2973.
[3] G.J. Kunde et al., Phys. Rev. Lett. **74** (1995) 74.
[4] A. Schuttauf et al., Nucl. Phys. **A607** (1996) 457.
[5] M.L. Cherry et al., Phys. Rev. **C52** (1995) 2652.
[6] C. Singh et al., Phys. Rev. **C54** (1996) 3185.
[7] M.L. Cherry et al., Acta Phys. Pol. **B29** (1998) 8–2155.
[8] H. Appelshauser et al. (NA49 collaboration), Eur. Phys. J. **A2** (1998) 383.
[9] J. Hubele et al. (ALADIN collaboration), Z. Phys **A340** (1991) 263.
[10] A.J. Baltz, C. Chasman and S.N. White, NIM **A417** (1998) 1.
[11] M. Vidovich, M. Greiner, C. Best and G. Soff, Phys. Rev. **C47** (1993) 2308.
[12] M. Vidovich, M. Greiner and G. Soff, Phys. Rev. **C48** (1993) 2011.
[13] B.L. Berman and S.C. Fultz, Rev. of Mod. Phys. **47** (1976) 713.

Chapter 5

[1] S. Peraire (CERN SL/IN), private communications.
[2] Minutes of the CERN LEMIC meeting of February 16, 1999.
[3] O. Villalobos et al., Internal Note ALICE 98–23.